INSTITUTO SUPERIOR DE ENGENHARIA DE LISBOA

Departamento de Engenharia de Electrónica e Telecomunicações e de Computadores

Study of the Bio-Radar radio channel

Beatriz Bento da Cruz

Graduate

Dissertação para obtenção do Grau de Mestre
em Engenharia Eletrónica e de Telecomunicações

Orientadores : Professor Doutor Pedro Pinho
Professor Doutor Carlos Mendes

Júri:
Presidente: Professor Doutor Alessandro Fantoni
Vogal: Professor Doutor Daniel Malafaia

December, 2023

INSTITUTO SUPERIOR DE ENGENHARIA DE LISBOA

Departamento de Engenharia de Electrónica e Telecomunicações e de Computadores

Study of the Bio-Radar radio channel

Beatriz Bento da Cruz

Graduate

Dissertação para obtenção do Grau de Mestre
em Engenharia Eletrónica e de Telecomunicações

Orientadores : Professor Doutor Pedro Pinho
Professor Doutor Carlos Mendes

Júri:
Presidente: Professor Doutor Alessandro Fantoni
Vogal: Professor Doutor Daniel Malafaia

December, 2023

Aos meus pais

Acknowledgments

First of all, I would like to thank my two supervisors, Professor Pedro Pinho and Professor Carlos Mendes for all the help and guidance given throughout this project as well as for the excellent orientation provided. Thank you for everything.

I would also like to thank Professor Daniel Albuquerque and Carolina Gouveia for all their essential help throughout this project. The work performed in this dissertation could not have been done without you both. Thank you for all your patience and for helping me overcome all the obstacles faced in this project. To you both I will always be grateful.

I would also like to express my gratitude to the Instituto de Telecomunicações for providing the resources that contributed to the completion of this dissertation. All the practical experiments conducted were made possible through the use of their facilities.

To my parents, I would like to express my gratitude for affording me the chance to enroll in this course and for all their unconditional support. Thank you for believing in me and for providing me with all these great opportunities.

Lastly, I would like to thank all my friends and my boyfriend for all their support, both in the work performed on this thesis and life in general.

To all of you, thank you!

Abstract

Micro-Doppler radars have been widely used for the remote vital signs acquisition. These type of radars are commonly known as Bio-Radar. The obtained vital signal quality is directly related with the received power, which can be inferred by using the radar equation. Nevertheless, there are other aspects that influence the received power, especially when the the target of interest is located near the antennas. To better understand the optimal radar configuration, it is necessary to study the propagation of the radio channel, whose study has been lacking in the literature.

In this work, simulations and experiments were performed to characterise the received signal power variation as well as the Radar Cross Section (RCS), according to the distance in relation to the Bio-Radar. The work performed, which involved conducting simulations and practical measurements on well-known shapes, has not only helped validate the software used in the simulations but also the practical measuring method of received power conducted in the anechoic chamber. Subsequently, an analysis was performed on human subjects, revealing that various factors could influence the obtained results, such as the posture of the subjects and their breathing patterns. Overall, for improved respiratory signal measurement, shorter distances, up to 1 meter, tend to be the most adequate.

Keywords: Bio-Radar, Vital signs, Near-field radar, Radar Cross Section

Resumo

Os radares de Micro-Doppler têm sido amplamente utilizados para a aquisição remota de sinais vitais. Este tipo de radar é tipicamente denominado de Bio-Radar. A qualidade do sinal vital obtido está diretamente relacionada com a potência recebida, que pode ser inferida através da equação do radar. No entanto, existem outros aspetos que influenciam a potência recebida, especialmente quando o alvo de interesse está localizado próximo das antenas. Para melhor compreender a configuração ótima do radar, é necessário estudar a propagação do canal de rádio, cujo estudo tem sido escasso na literatura.

Neste trabalho, foram realizadas simulações e experiências para caracterizar a variação da potência do sinal recebido, bem como a Secção Eficaz de Dispersão (RCS), de acordo com a distância em relação ao Bio-Radar. O trabalho realizado, que envolveu a realização de simulações e medições práticas em formas geométricas conhecidas, não só ajudou a validar o software utilizado nas simulações, mas também o método prático de medição da potência recebida realizado na câmara anecoica. Posteriormente, foi realizada uma análise em seres humanos, revelando que vários fatores poderiam influenciar os resultados obtidos, como a postura dos sujeitos e os seus padrões de respiração. No geral, para obter uma boa medida do sinal respiratório, distâncias mais curtas, até 1 metro, tendem a ser as mais adequadas.

Palavras-chave: Bio-Radar, Sinais Vitais, Radar em região de campo próximo, Secção Eficaz de Dispersão

Contents

List of Figures

List of Tables

1

Introduction

1.1 Motivation

According to the World Health Organization (WHO), cardiovascular diseases are the leading cause of death globally, taking an estimated 17.9 million lives each year [1]. More than four out of five cardiovascular diseases deaths are due to heart attacks and strokes, and one third of these deaths occur prematurely in people under 70 years of age [1]. In order to preventably detect and monitor these problems it is necessary to use devices to monitor heart and respiratory rhythm.

The Bio-Radar system allows the monitorization of the cardiopulmonary signal with precision without the need for physical contact, avoiding the usage of contact electrodes or any type of invasive sensors. The applications of this system are varied, for example, in a burn unit or even with bedridden patients, as it was the case with those suffering from Covid-19 [2]. This way, the subjects can be observed more comfortably, continuously and over long periods of time. In addition, the system can be marketed, for example, to monitor the vital signs of a driver and prevent possible accidents when the driver has a cardiac arrest or shows signs of fatigue. This technology has been referred to as one of the most promising contactless tools to overcome these obstacles [3]. In this dissertation, the Bio-Radar system used was the prototype developed in [2]. This prototype offers a low power and portable solution for Bio-Radar implementation.

The quality of the obtained signal is directly related with the received power provided

by the reflecting chest-wall. The good functioning of the Bio-Radar system is dependent on the setup characteristics, such as transmitted power, antenna gain or directivity. These factors have an impact on the SNR (Signal-to-Noise Ratio) of the signal [4]. Besides the setup characteristics, the system also depends on the subjects characteristics, such as subject's interpersonal variability in breathing pattern and their body position and stature. The main challenge faced in this dissertation is in fact that the subject under study is a reflective target that may impact the propagation channel and consequently the received power. In this way, it is important to study the radio channel of the Bio-Radar system and how it varies with target characteristics. The main goal is not only evaluate the impact that different subjects have on the propagation channel, but also to observe if there is an optimal distance to measure parameters such as the respiratory signal for various subjects.

1.2 Dissertation Goals

In order to perform an analysis of the Bio-Radar system, it is important to characterize and also have a better understanding of the radio channel of the Bio-Radar. For this purpose, it is important to acknowledge which is the optimal radar configuration. In this sense, the main goals for this dissertation are:

- Study of the radar far-field and the near-field regions. Have a clear understanding regarding the effects of the targets near-field versus the antennas near-field;
- Perform simulations to assess the Radar Cross Section (RCS) of simple target shapes and compare them to the theoretical equations. Validate the practical measuring process used to carry out experiments in the anechoic chamber;
- Perform simulations of the RCS of different 3D CAD subjects. Observe the impact that the gender, height, or weight have on the received power as well as the RCS. Verify if there is an optimal distance for each subject type;
- Perform tests with a mannequin and real humans with different characteristics to observe the impacts on the RCS, in the anechoic chamber. Observe the respiratory signal for different subjects at several distances. Compare with the results performed in the simulation.

1.3 Structure of the document

In Chapter 2, the basic principles of the Bio-Radar are studied, as well as, the related work of this dissertation.

In Chapter 3, the simulations to assess the RCS of simple target shapes were done. Those values were compared to the theoretical equations. Also, the validation of the practical measuring process used to carry out some experiments in the anechoic chamber was performed.

In Chapter 4 simulations were performed on three different 3D CAD subjects, observing the different impacts that certain characteristics have on the received power and RCS. Also in this chapter, it was possible to validate the far-field criterion with the simulation software.

In Chapter 5, practical measurements were performed in the anechoic chamber with a mannequin and with three human subjects. The received power, the RCS and the respiratory signal, for the human subjects, were analysed and compared.

In Chapter 6 is presented a brief conclusion and the future work intended to be done/improved upon.

In Appendices A and B, auxiliary simulations and practical experiments involving the 3D subjects and the mannequin were performed.

1.4 Contributions from the developed work

The study performed in this dissertation attempts to address certain problems regarding the radio channel of the Bio-Radar. While doing so, several contributions were made along this process. The articles published were:

- C. Gouveia, B. Cruz, P. Pinho and D. Albuquerque, "*Signal Power Variation for Bio-Radar Applications*", published in *XIV Iberian Meeting on Computational Electromagnetics* in 2022;

- D. Albuquerque, B. Cruz, C. Gouveia, V. Coelho, P. Pinho, J. Matos, A. Oliveira and N. Carvalho, "*Indoor near Field Impact in the RADAR Signals for 6G Mobile Networks Integration*", published in *13th IEEE/IET international symposium on communication systems, networks and digital signal processing* (CSNDSP22) in 2022;

- B. Cruz, C. Gouveia, P. Pinho, D. Albuquerque and C. Mendes, "*Near-Field Impact in Various Targets for Bio-Radar Applications*", presented at the *16th Congress of the Portuguese Committee of URSI* in 2022.;

In these articles, simulations were performed to characterize the variation in received signal power as well as the RCS, considering a certain distance of the subject from the radar. With the work presented, it was demonstrated that different targets have different impacts on the RCS, and it requires an in-depth study to better understand the best operating distance for each target. Additionally, in the article published in the *13th IEEE/IET International Symposium on Communication Systems, Networks, and Digital Signal Processing* (CSNDSP22), the aim was to study the impact of the near-field on RADAR signals for 6G mobile network integration. In this work, various concepts were studied regarding propagation in the near-field region. Although the work performed was done for another application context, the addressed concepts can be directly applied in this work.

2

Near-field impact in Bio-Radar Systems

This chapter is divided into two main sections. The first section explores the basic principles of Bio-Radar, while the second section is dedicated to related work, primarily focusing on the radar near-field region.

2.1 Basic Principles of the Bio-Radar

This section aims to outline the basic principles of the Bio-Radar system developed in [2]. Firstly, a brief description of radar fundamentals is provided, along with an explanation of the fundamental function of the Bio-Radar system. Subsequently, it was delved into the study of Doppler radar, different ways to classify radar systems, and the concepts of monostatic and bistatic radar. Furthermore, it was explored the radar equation, RCS, optical regions of the RCS, and the far-field criterion. Finally, both the far-field region and the near-field of the radar system were characterised.

2.1.1 Radar Fundamentals

RADAR or Radio Detection And Ranging is an electromagnetic system for the detection and location of target objects such as aircraft, ships, spacecraft, vehicles, people, and the natural environment which can reflect a signal back [5]. The simplest form of a radar system consists in a transmitter, a receiver, an antenna and hardware or software dedicated to signal processing, just like illustrated in Figure 2.1, [2].

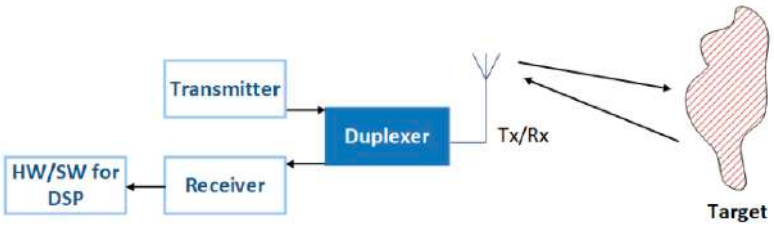

Figure 2.1: Basic model of a radar system, [2].

The transmitter and the receiver are connected to an antenna. The transmitter sends a signal in the form of an electromagnetic wave towards one or more targets. Subsequently, the receiver is designed to collect as much energy as possible from the echoes reflected in its direction by the target, and then it processes this information.

Regarding its functioning, the Bio-Radar system sends an electromagnetic wave towards the rib cage of the subject, which is then reflected and received by the radar. The received signal is processed in order to extract two main vital signs: Respiratory signal and Cardiac signal. The simplified working principle of the radar system is represented in Figure 2.2, where Tx and Rx represent the transmitter and receiver antennas respectively, Δr is the amplitude of the respiratory signal and R is the distance between the subject and the antennas.

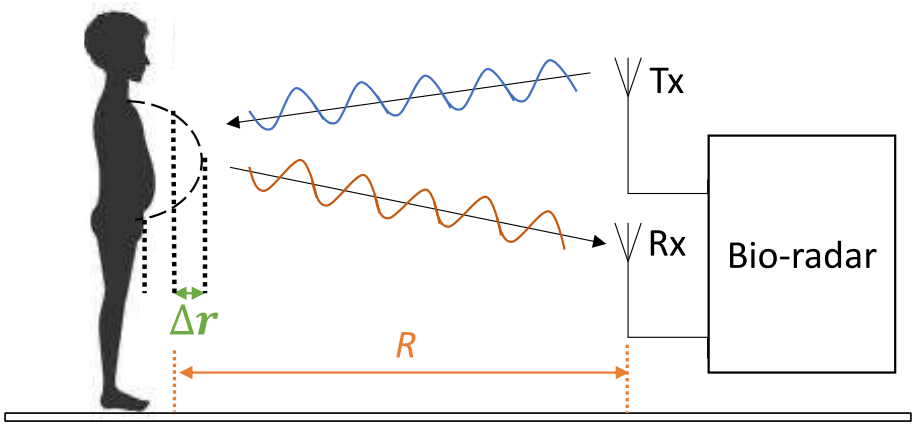

Figure 2.2: Function of Bio-Radar system.

2.1.2 Radar Systems

There are various ways to classify radar systems. Radars can be categorised into numerous groups based on specific radar characteristics, such as frequency band, antenna type, and waveforms used. These categories include weather radar, acquisition and

search radar, tracking radar, track-while-scan radar, fire control radar, early warning radar, over-the-horizon radar, terrain-following radar, and obstacle avoidance radar [6]. In terms of radar operation modes, radars are commonly classified into four types: Pulsed Wave radar (PW), Continuous Wave radar (CW), Frequency-Modulated Continuous Wave radar (FMCW), and Ultra-WideBand radar (UWB). UWB is a form of Pulsed Wave radar [6].

Nowadays, the CW , the FMCW or UWB radar are the most frequent radar system types to apply in remote measurement of vital signs [3]. In Figure 2.3 is illustrated the usual radar operation modes used in vital signs sensing applications.

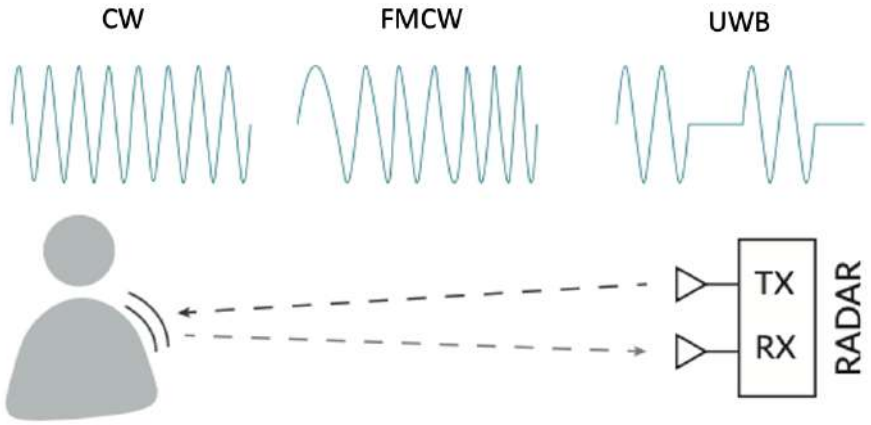

Figure 2.3: Usual radar operation modes used in vital signs sensing applications: CW, FMCW and UWB [3].

Continuous Wave Radar

The Continuous Wave (CW) radar continuously transmits and receives electromagnetic energy using separate antennas [7]. These radar systems are the most common and simplest type of radar. Several studies have already demonstrated the capability of these radar systems in measuring respiratory and heartbeat signals [3]. Each radar system depends not only on the type of waveform but also on whether it operates continuously or intermittently [5]. The Bio-Radar, being a CW radar, simultaneously transmits and receives a continuous sine wave. This capability enables it to detect moving targets [8] and measure the velocity of the target's motion, allowing it to distinguish between moving targets and stationary objects [2]. The Bio-Radar used in this dissertation is a CW radar.

Frequency-Modulated Continuous Wave Radar

The FMCW radar system is also commonly used for vital signs sensing applications. In this type of radar, the transmitted signal frequency is modulated over time, allowing it to compute the target's velocity and the distance between the target and the radar [2]. Frequency modulation in FMCW systems is typically triangular, causing the frequency to vary gradually [9]. An example of modulation in an FMCW radar is illustrated in Figure 2.4. The solid line represents the transmitted signal, while the dashed line represents the received signal. The received signal is delayed by $T = 2R/c$, where R is the range to the target, and c is the speed of light. The bottom line represents the absolute value of the frequency difference between the transmitted and received signals.

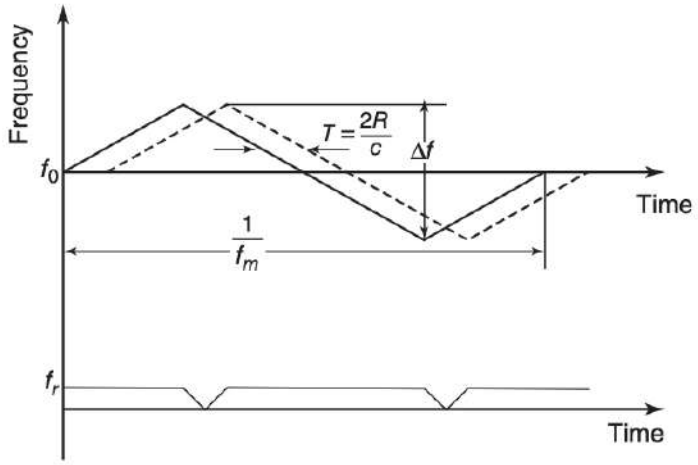

Figure 2.4: Example of the modulation in an FMCW radar [9].

However, FMCW devices have significantly more complex hardware architecture than the simple CW radars. This aspect, not only consumes more energy from the power supply, but also, requires more complex signal radar processing methods [3].

Pulse Wave Radar

A pulse radar transmits pulsed bursts and then listens to the resultant echoes. The transmitter and the receiver do not operate simultaneously, and it uses the Doppler effect to detect moving targets [7].

There are typically two types of pulse radar: Moving Target Indication Radar (MTI) and pulse Doppler radar. MTI Radar can differentiate between a reflected signal coming from a stationary target, a moving target, and clutter by utilizing the Doppler shift

in frequencies [8]. In this radar, the sampling rate is usually selected to be low enough to avoid ambiguities in range. On the other hand, pulse Doppler radar operates at a high sampling rate to avoid blind speeds, which can result in ambiguities in range. This radar uses a medium or high pulse repetition frequency to detect moving targets in clutter and is primarily used by the army, navy, and air force.

This type of radar system is typically not used for vital signal acquisition because pulse wave radar systems are better suited for long-range detection, whereas CW radar, FMCW radar or UWB radar are better suited for short-range detection [[3],[10]].

Ultra-Wideband Radar

The Ultra-Wideband Radar (UWB) radar was recently introduced as a high-resolution radar system that is capable of vital signs measurements through pulse-timing techniques [3]. This radar is a special application of the PW radar and it is characterised by its large bandwidth regarding the center frequency [2]. It is generated by a very short duration pulses rather than continuous waves. Just like the PW Radar, in UWB the transmitter and the receiver antennas do not operate at the same time.

2.1.3 The Doppler Radar

Doppler radars are based on the Doppler effect, also known as Doppler shift. This effect results from the motion of the target relative to the radar and causes a change in the frequency of the received signal. Doppler radar systems provide information about the movement and position of targets [11].

By measuring the phase shift between a transmitted pulse and a received echo, the radar can assess the target's movement, including its radial velocity, which is the velocity along the line of sight [11]. The Doppler frequency increases as a target approaches the radar and decreases as it moves away. Additionally, if either the radar or the observer is in motion, an apparent shift in frequency occurs. This principle underlies various radar architectures, including PW radar, CW radar, and FMCW radar [11].

The Bio-Radar is a type of Micro-Doppler radar, which detects the Micro-Doppler effect. This effect occurs when small movements, such as mechanical vibrations, produce phase differences between the transmitted and reflected waves. These phase differences are particularly noticeable in the received signals [11].

2.1.4 Monostatic and Bistatic Radar

The positioning of the transmitter and receiver antennas can classify radar systems into two types: bistatic/multistatic and monostatic radars. In bistatic/multistatic radars, the transmitter and receiver antennas are placed in two or more different locations, with significant separation distances between them. On the other hand, radars where the same antenna is used for both transmission and reception, or where the transmitter and receiver antennas are in approximately the same location, are called monostatic radars [7].

In monostatic radar systems, the high transmitting power is sometimes directly coupled to the receiver. This can lead to self-jamming, saturation, or even damage to the receiver. In contrast, the bistatic configuration can be more efficient than monostatic in terms of self-jamming, as physical distance can provide sufficient isolation between transmitting and receiving paths. However, despite these challenges, many modern radars are monostatic due to the simple architecture enabled by a monostatic system [9]. The Bio-Radar used in this study can be classified as a monostatic radar since the transmitter and receiver antennas are located in approximately the same location. A brief illustration of a monostatic radar is shown in Figure 2.5.

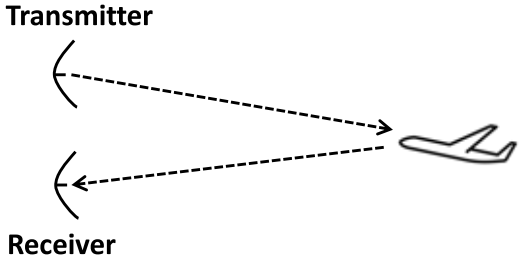

Figure 2.5: Monostatic CW Radar.

2.1.5 Radar Equation and Radar Cross Section (RCS)

The Bio-Radar signal accuracy depends on the received power, which could be inferred using the radar equation. The radar equation is used to estimate the received power in a radar system, for a target with given properties and range from the transceiver, and it can be used to help determine the system theoretical limits [9]. This equation relates the range of a radar to the characteristics of the transmitter, receiver, antenna, target, and distance. If a monostatic radar is considered, the power density P_d at the target is given by equation (2.1), where P_t is the transmitted power, G_t is the antenna gain and R is the distance of the target [12].

$$P_d = \frac{P_t G_t}{4\pi R^2} \tag{2.1}$$

Assuming the target receives the incident power with an area σ, also known as RCS, and radiates isotropically, the power density at the radar is given by equation (2.2) [12].

$$P'_d = \frac{P_t G_t \sigma}{(4\pi R^2)^2} \tag{2.2}$$

Afterwards, its taken into consideration that the radar antenna has an effective area A_e, which is related to the antenna gain by $A_e = G_r \lambda^2 / 4\pi$ [12]. Then, the power received by the radar, also known as the radar equation is given by (2.3), where P_r is the received power, G_r is the gain of the receiving antenna, G_t is the gain of the transmitting antenna, λ is the wavelength, σ is the RCS and R the distance to the target.

$$P_r = P'_d A_e = \frac{P_t G_t G_r \lambda^2 \sigma}{(4\pi)^3 R^4} \tag{2.3}$$

According to the radar equation [13], the RCS can be obtained if equation (2.3) is put in order of σ. The RCS of a target is the equivalent area seen by a radar. It is the property of a scattering object or target, which represents the fraction of the echo signal returned to the radar by the target compared with the echo that would be reflected by a perfectly conducting sphere with a 1 m^2 cross-sectional area [9].

Overall, there are two types of conditions of the RCS in regards of the wavelength. Firstly, if the wavelength is large compared with the targets dimensions, the scattering is in Rayleigh region. If, on the other hand, the wavelength is small compared with the targets dimensions, the scattering is in the optical region. Scattering from aircraft or ships at microwave frequencies generally is in the optical region where the RCS is affected more by the shape of the object than by its reflecting area. In between the Rayleigh and the optical region is the resonance region where the radar wavelength is comparable to the targets dimensions [9]. All this regions are explained in more detail in the following section.

2.1.6 Optical Regions of the RCS

Theoretically, the RCS of a target can be determined by solving Maxwell's equations with proper boundary conditions [12]. However, only objects with simple geometries can be determined by these methods. According to [12], the RCS of a simple conducting sphere is $2\pi a/\lambda$, where a is the radius of the sphere and λ is the wavelength. This

relationship can be observed in Figure 2.6.

In Figure 2.6, the RCS can be divided into three regions: the Rayleigh region, the Mile or resonance region, and the optical region. In the optical region, the dimensions of the sphere are large compared to the wavelength, and the RCS is independent of the frequency. Therefore, the reflecting area of the sphere is equivalent to the area of a circle with the radius of the sphere, and the RCS is a constant value of πa^2.

In the Rayleigh region, the size of the sphere is small compared to the wavelength, and the RCS varies with λ^4. In the Mie or resonance region, which is between the optical and the Rayleigh region, the RCS oscillates with frequency [12]. The Mie region is the region of the electromagnetic spectrum where the wavelength of the signal is comparable to the size of the scattering target. The Bio-Radar system operates in the optical region because the dimensions of the target are large when compared to the wavelength.

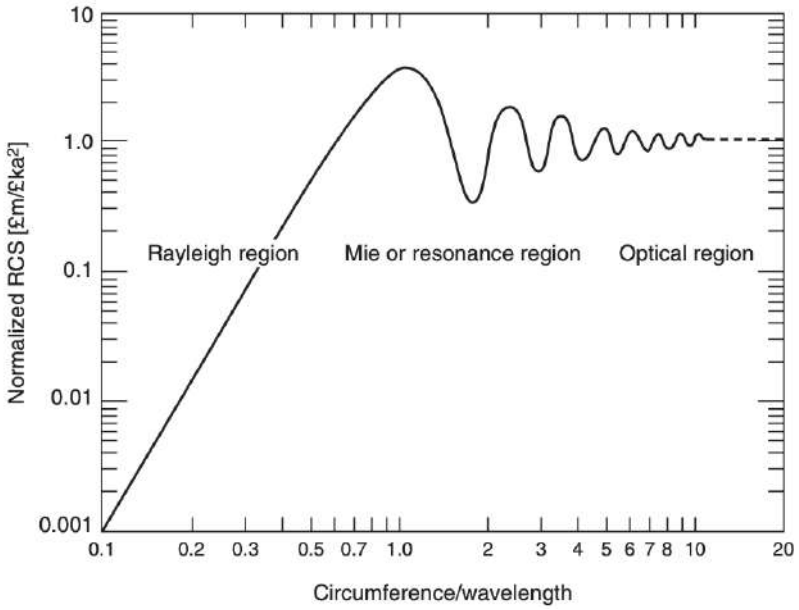

Figure 2.6: RCS of a Conducting Sphere as a Function of the Normalised Circumference [12].

2.1.7 Far-field criterion

The RCS, as previously observed, can be obtained if equation (2.3) is rearranged with respect to σ. However, the RCS obtained is not always constant. This is because, when considering the far-field, the RCS is independent of distance, meaning that it remains constant. But in the near-field region, the RCS varies with distance, indicating that it is not always constant.

The far-field criterion requires that the target be located at an infinite distance, ensuring that a plane wave illuminates the target. To perform an analysis in the far-field region, the choice of whether to consider the antenna or the target in the equation depends on whether it is intended to analyse the far-field region from the antennas point of view or the target's point of view. This will be explained in more detail later in section 2.1.8.

In general, the target and measurement sensors are always situated at a finite distance apart. Thus, the incident wave is spherical [14]. To measure RCS with an acceptable error of 1 dB, the target must be at a certain distance. Regarding the far-field region of the target, the distance is given by equation (2.4), where D is the largest dimension of the target, and λ is the wavelength.

$$R \geqslant \frac{2D^2}{\lambda} \tag{2.4}$$

2.1.8 The Far-field and the Near-field region

As previously mentioned in Section 2.1.7, in the near-field region, the absorption of radiation affects the load on the transmitter, while in the far-field, the absorption of radiation does not affect the transmitter [15]. This holds true when considering the far-field from the perspective of the antennas. However, in the near-field from the perspective of the target, the main concern is that the RCS is not constant. In this subsection, the goal is to further explain the difference between the two near-field scenarios.

Traditional radar systems are typically analysed assuming that the target is in the far-field region. This approach reduces the analysis complexity and simplifies the RCS computation since the RCS does not vary with the distance. As a result, most of the theory presented in radar textbooks relies on far-field configurations [13]. However, the Bio-Radar system studied in this dissertation is implemented in a short-range, less than 2 m, and although it is possible to operate in the antennas far-field region, the same cannot be applied on the target side due to the human body/target dimensions. The far-field region of the antennas of the Bio-Radar system used is above 0.5 m, and since the system is implemented in a 2 m or less range, all the simulations and experiments conducted are always performed in the far-field region of the antennas.

Although the Bio-Radar system is being operated in the antenna's far-field region, the target reflects the signal thus arising a new far-field and near-field regarding the target's point of view. The concept described is shown in Figure 2.7. Thus, despite the radar equation being valid for both near and far-field regions [13], the RCS is difficult to quantify not only because the radar could be operating in a near-field region,

considering the target's point of view, but also due to the complex human body shape.

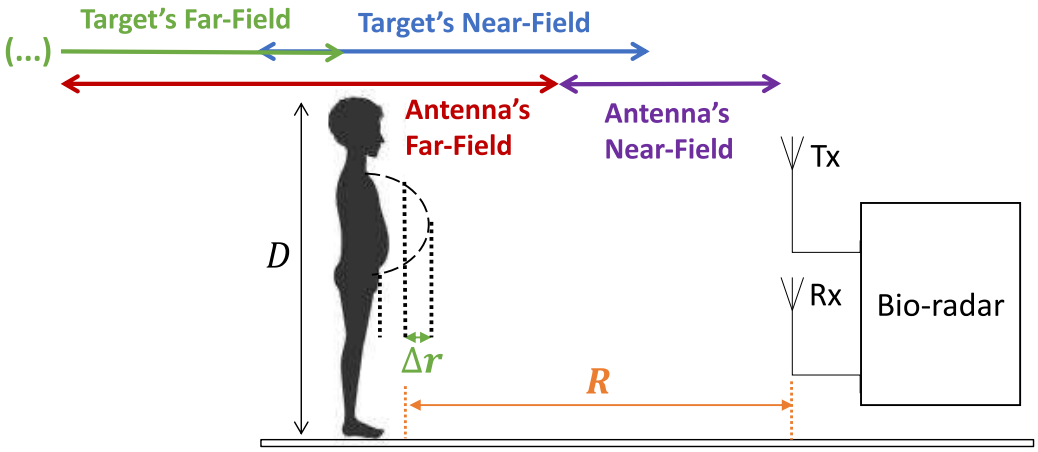

Figure 2.7: Far-field and near-field regarding the target's point of view.

2.1.9 RCS of well-known shapes in the near-field region

To date, very few articles have been published regarding the study of RCS in the near-field region. However, in [13] and [16], analytical calculations of the near-field RCS were conducted for a circular and a rectangular plate at normal incidence, utilizing the theory derived from Physical Optics (PO). In these studies, the target's surface was approximated using flat surface patches. These patches were sized to represent individual approximations to the far-field. Subsequently, integration over each meshing element was performed analytically, and the reflection from the entire object was calculated by vectorially summing all individual elementary reflections.

The RCS is most commonly defined in the far-field region. There are two primary aspects in which near-field RCS differs from far-field RCS. Firstly, near-field RCS depends on the range (R), whereas far-field RCS depends solely on target size and frequency [13]. Secondly, near-field RCS exhibits an oscillatory nature as a function of range and target size, while far-field RCS for the same target and incidence angle increases monotonically with size and frequency [13]. Determining RCS in the far-field is generally less complex because RCS is entirely independent of the range between the radar and the target [16].

In the far-field region, the RCS depends on the geometry, the size of the target and material. In equation (2.5) is presented the RCS equation for a large, smooth plane surface of any shape made of perfect electric conductor (PEC), where A is the plate area and λ is the wavelength [7].

$$\sigma = \frac{4\pi A^2}{\lambda^2} \tag{2.5}$$

According to equation (2.5), RCS does not depend on the distance between the antennas and the target. However, in the near-field region, the same cannot be inferred. To study this aspect, the RCS was theoretically estimated for circular, square, and rectangular plate targets in the near-field region using the RCS equations presented in [16]. These equations were derived considering that the flat plate was observed in normal incidence (with the radar axis parallel to the Z-axis), as illustrated in Figure 2.8.

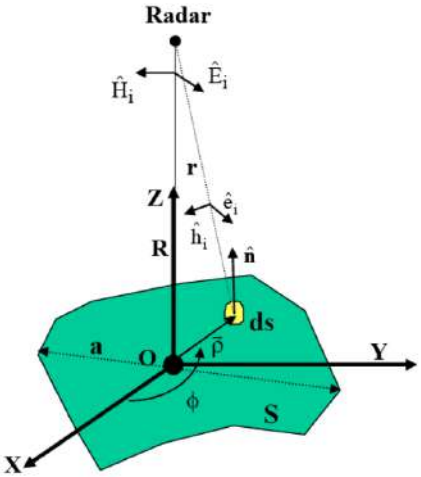

Figure 2.8: Geometry of the backscattering by a flat plate in near-field [16].

In order to come up with the equations of the RCS for well-known shapes, it was considered an expression of the magnetic field scattered by a perfectly conducting target. This expression was obtained and then simplified due to PO approximations [16].

RCS of a circular plate target

For a circular flat plate target made of PEC, the theoretical equation for the near-field region is given by equation (2.6) (deducted in [16]). The area of the target is given by A, the range distance between the antennas and the target is given by R and λ is the wavelength. This formula confirms the periodic behaviour of RCS versus frequency and the empirical formulae established in [17] and [18].

$$\sigma(R) = 2\pi R^2 \left[1 - \cos\left(\frac{2A}{\lambda R}\right) \right] \tag{2.6}$$

From the previous equation, it can be deduced that the RCS does not increase with

the square of the frequency, as it happens in the far-field region. The RCS can vary between 0 and $4\pi R^2$. Additionally, the average RCS of the circular target is $2\pi R^2$.

RCS of square plate target

The next example considered is a flat square target with side a, also made from the material PEC, at normal incidence. The PO derivation for that case is much more complicated than for the circular plate and the resulting near-field RCS does not display the same well-defined oscillations. In fact, this RCS tends to a limit value as we increase the frequency, which is $\lim_{f\to\infty}\sigma = \pi R^2$ [13]. The RCS equation for a square plate target in the near field region is given by (2.7) (deducted in [16]), a represents the side of the square, R is the distance between the target and the antennas and $X = R\lambda/\pi^2 a^2$.

$$\sigma(R) = 4\pi R^2\left[0.25 + 2X + X^2 - X\sin\left(\frac{1}{\pi X}\right) - \sqrt{2X}(1+2X)\sin\left(\frac{\pi}{4} - \frac{1}{2\pi X}\right)\right] \tag{2.7}$$

When analysing this equation it is important to consider that as long as we are in the near-field regime, the lowest-power term in R (which in this case is R^2) is the dominant one. Consequently, upon inserting the RCS formula into the radar equation, the square plate produces a radar-received power that displays the same-order variation with range as the circular plate, proportional to $1/R^2$ [13].

RCS of rectangular plate target

The last target shape that was taken into consideration on this analysis was the rectangular flat plate. The RCS equation for a rectangular target in the near field region is given by (2.8), a is the width of the rectangle, b is the height of the rectangle, R is the distance between the target and the antennas and $k = 2\pi f/c$ (f being the frequency and c being the speed of light).

$$\sigma(R) = \frac{4\pi}{\lambda^2}\left|\left(\sqrt{\frac{R\lambda}{2}}e^{j\frac{\pi}{4}} - j\frac{2R}{ka}e^{j\frac{ka^2}{4R}}\left(1 - j\frac{\lambda R}{\pi a^2}\right)\right)\times\left(\sqrt{\frac{R\lambda}{2}}e^{j\frac{\pi}{4}} - j\frac{2R}{kb}e^{j\frac{b^2}{4R}}\left(1 - j\frac{\lambda R}{\pi b^2}\right)\right)\right|^2 \tag{2.8}$$

2.2 Related Work

When analyzing a radar system, it is assumed that the target and radar antenna are in the far-field region with respect to one another. This assumption simplifies the analysis performed in general and allows for the precise definition of certain parameters such

as antenna directivity and RCS [13]. However, as previously seen at short ranges, although it is possible to operate in the antenna's far-field region, the same cannot be applied on the target side due to the human body's/target's dimensions.

In this section, eight different works were studied in order to better understand the near-field region of the target as well as how to characterize different targets in this region.

2.2.1 RCS Measurements of Pedestrian Dummies and Humans

In [19], a number of results from an extensive series of RCS laboratory measurements on pedestrian dummies and humans are presented. The main focus was to enhance road safety on European streets and reduce the number of road fatalities. In the tests carried out, the radar system used was the SRR (short-range radar), which operates in CW mode. This type of radar system is useful for monitoring the area around a vehicle to detect obstacles, such as other vehicles, pedestrians, or static obstacles.

All the RCS measurements of the subjects were conducted in the anechoic chamber of the European Microwave Signature Laboratory (EMSL). The measurements served a dual purpose: first, to gather RCS signatures of pedestrian dummies, and second, to assess their similarity to the RCS signatures of humans. These RCS measurements were simultaneously performed in the frequency bands of 23–28 GHz and 76–81 GHz using two Vector Network Analyzers (VNAs) equipped with a common trigger input signal. Although the frequency range used differs from that in the Bio-Radar system in this dissertation, some of the concepts and procedures applied are valuable for a better understanding of certain aspects in this dissertation. A VNA is an instrument designed to measure the frequency response of a component or a network comprising multiple components, which can be either passive or active. It measures the power of a high-frequency signal transmitted into and received from a component or network. Unlike voltage and current, power can be accurately measured at high frequencies. At each frequency point, the VNA captures both the amplitude and phase of the high-frequency signal. The VNA's built-in computer calculates key parameters such as return loss and insertion loss for the network under test [20].

In the study conducted in [19], a quasi-monostatic configuration was employed, with Tx and Rx antennas positioned along the horizontal cross-range axis. The horizontal separation between the two sets of Tx/Rx antennas was 15 cm. As for the range distance between the antenna apertures and the rotation axis of the turntable, it measured 3.4 m. This range is slightly greater than the one used in Bio-Radar applications. The schematic for the setup is depicted in Figure 2.9.

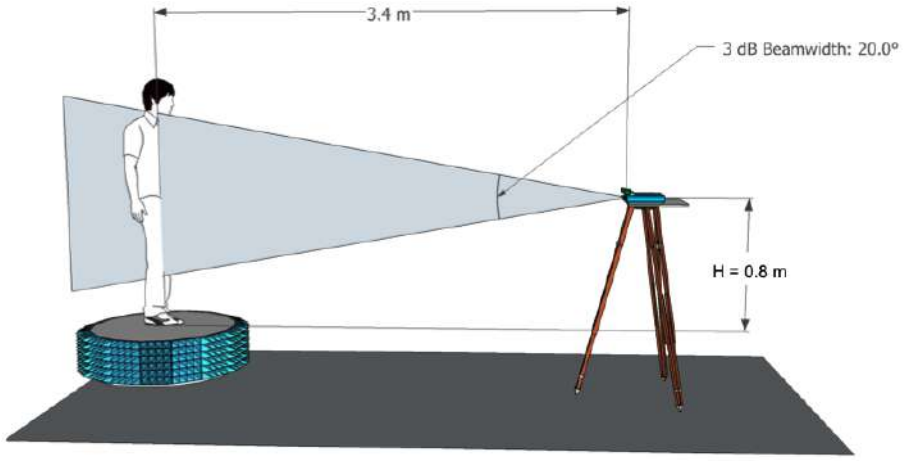

Figure 2.9: Sketch showing the measurement set-up used in the RCS measurements [19].

With the setup described in Figure 2.9, the tests involved 11 pedestrian dummies. In addition to measuring the RCS of the pedestrian dummies, a series of tests was conducted to compare the RCS of humans under the same conditions. The aim of these additional measurements was:

- To assess the degree of similarity between the typical RCS signatures of pedestrian dummies and those of real humans.
- To investigate the impact of different types of clothing on the measured RCS.

However, it is also important to mention that establishing the degree of similarity of the RCS among different types of pedestrian dummies or between humans and pedestrian dummies is not a trivial task. This is because the collected backscatter datasets are multi-dimensional and can be treated in many different forms [19].

In the study described earlier, the RCS measurements were categorized into three different groups. The first group involved characterizing all available dummies at various heights relative to the radar antennas. The second group focused on assessing the impact of clothing on the RCS signatures of both pedestrian dummies and humans. Finally, the third group used a specific dummy to evaluate the influence of movement on the measured RCS.

The main conclusions drawn from this work indicated that pedestrian's height had an impact on the measured RCS, particularly in the higher frequency bands where clear effects on the RCS averages were observed. Concerning the impact of clothing, it was

found that in most cases, clothing did not significantly affect the RCS. Regarding the comparison of RCS signatures between dummies and humans, the results showed that the RCS obtained from the dummies was slightly lower than that of the humans [19].

This previous work provides valuable insights that can be applied in this dissertation. Firstly, it underscores the importance of accurately aligning the antennas with the subject's chest wall because the subject's height has a discernible impact on the RCS. Additionally, when conducting experiments with both dummies and humans, it is likely that the RCS values obtained from the dummies will be slightly lower than those from the humans. In the context of this dissertation, the goal is not only to observe the RCS of dummies and humans but also to perform a comparative analysis involving subjects with diverse characteristics, including variations in shape, weight, height, and gender. This comparative study aims to elucidate the influence of these factors on the optimal operating distance.

2.2.2 Tool to Characterize the RCS of a Pedestrian in Near-Field

In the study presented in [21], a simulation tool was employed to characterize the RCS of a pedestrian in the near-field while considering the far-field of the antenna. This tool was developed with the aim of predicting and optimising the performance of short-range radar systems used in autonomous vehicle operations. The tool relies on an analytical model that combines human body modeling with Physical Optics (PO) theory. To validate this model's accuracy, a comparison was made between simulated, theoretical, and experimental data related to the RCS of both metal and lossy spheres, as well as an adult subject. These tests were conducted within the frequency range of 23–28 GHz [21].

The radar system used in this study is UWB (Ultra-WideBand), a technology commonly employed for human tracking due to its benefits in conditions of poor visibility. It is especially valued for its utilisation of wide bandwidth signals, enabling high-resolution ranging and localisation capabilities [21]. Although the frequency range and radar system differ from those used in the Bio-Radar, the underlying principles can be adapted and applied in various scenarios.

The presented results comprise a series of RCS measurements on pedestrian dummies and humans, where the influence of their dimensions and the effect of clothing were analysed in the 24 GHz and 77 GHz frequency bands. In the conducted tests, the subjects were positioned at specific distances, identifying a near-field region due to the high working frequencies and the dimensions of the human targets [[21], [22]]. According to [21], there have been very few studies assessing the features and accuracy of the

3D models employed in scattering problems. In [21], the human body is modeled using canonical geometries based on the cuboid equation, rendering the model suitable for all dimensions and postures of any target that requires analysis. The cuboid equation is presented in (2.9), representing the surface of a cuboid in a 3D space, where x_g, y_g, z_g are the coordinates of the center of the geometric shape, and a, b, c are the semi-length, semi-width, and semi-height, respectively, of the geometric shape.

$$f(x,y,z) = \left(\frac{x-x_g}{a}\right)^m + \left(\frac{y-y_g}{b}\right)^n + \left(\frac{z-z_g}{c}\right)^p = 1 \tag{2.9}$$

Afterwards, a human model has been modelled as having 13 body parts, reproduced by the combination of a sphere, cylinders, and a parallelepiped. All these geometric shapes were obtained using equation (2.9). The chosen dimensions are equivalent to the average human body size [21]. The model created is presented in Figure 2.10.

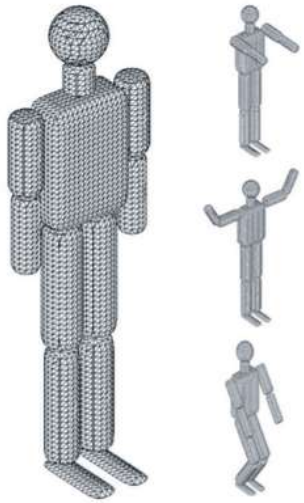

Figure 2.10: Human body model analytically expressed in several positions [21].

Subsequently, several simulations were performed to determine the RCS of metal and lossy spheres, as well as the RCS of a pedestrian. These targets were measured in the frequency range of 23–28 GHz. The main goals were to determine the accuracy of the proposed simulation tool and to validate the analytical approach for RCS evaluation in the near-field region. The simulated results were compared with the experimental tests presented and discussed in [19] and with the theoretical results based on the Mie theory [21].

The RCS measurements were performed in an anechoic chamber at the European Microwave Signature Laboratory (EMSL) by the European Commission Joint Research

Centre [19]. The characteristics of the measurement setup were replicated in the simulation tool. The setup used is presented in Figure 2.11. The Tx and Rx antennas were placed in a quasi-monostatic configuration, with a horizontal separation of about 15 cm between them. The polarisation was vertical for both Tx and Rx antennas. The range distance between the antenna apertures and the rotation axis of the turntable was 3.4 m. The antennas were positioned at 1.1 m above the ground [19].

Firstly, RCS simulations were conducted for metal and lossy spheres. The results were then compared with the simulations presented in [19] and with the Mie Series. The RCS results obtained were consistent with those in [19] as well as with the theoretical predictions. Regarding the RCS of a pedestrian, a similar analysis was performed. The RCS results were also found to be consistent with the simulations presented in [19]. However, slight movements or different positions of the target had a significant impact on the RCS.

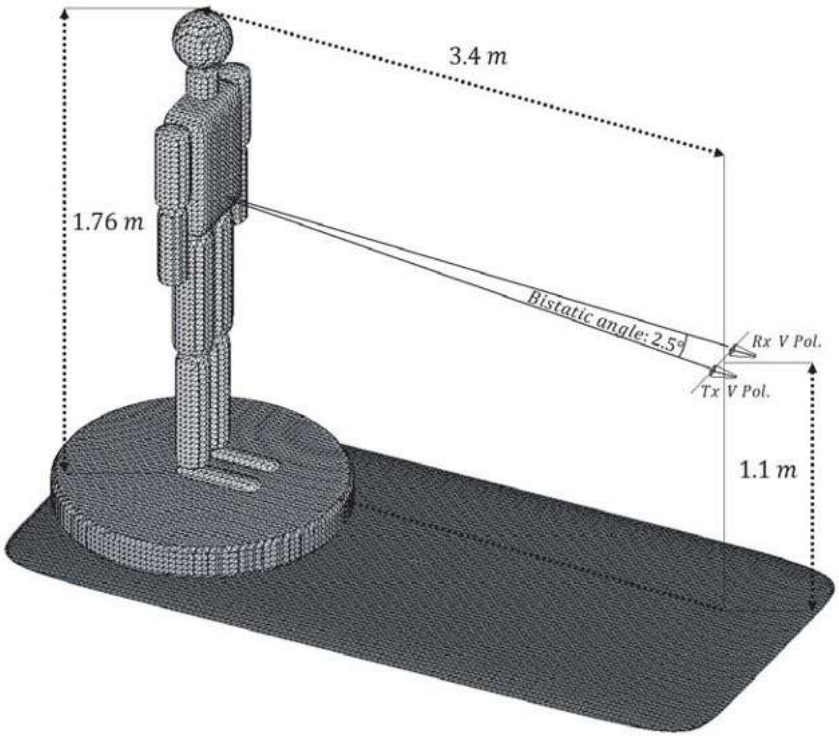

Figure 2.11: Setup for the evaluation of the RCS of a human target [21].

In this dissertation, the work that will be carried out is based on the aspects presented in [21]. For this purpose, the same validation methods will be used, and initially, a known target will be considered to determine the RCS. It is important to note that, despite mentioning the validity of the simulation tool used and its comparison with other simulation tools, this tool is not clearly described in the article. Additionally,

it is worth mentioning that in the ongoing dissertation, apart from conducting RCS simulations for various targets, the intention is to validate all simulations conducted in the anechoic chamber.

2.2.3 RCS Measurements of the Human Body for Breath-Activity Monitoring Applications

In [23], an experimental setup for measuring complex monostatic RCS was conducted with measurements in the 1–10 GHz frequency band. These experiments were carried out in a modified semi-anechoic chamber with the intended application being the measurement of the complex RCS of the human body during respiratory activity. The proposed RCS test range was calibrated using an aluminium flat panel, and its performance was tested against canonical targets. Subsequently, the setup was employed to conduct investigations on the RCS of a volunteer, with a focus on the changes resulting from breath activity. The radar operated in UWB mode.

The chamber described in [23] was transformed into a fully anechoic chamber by covering the floor with panels adorned with ferrite tiles and lining the walls with pyramidal absorbers. This transformation was done to make it suitable for RCS measurements. The measurements in the chamber were performed using a Vector Network Analyser (VNA), with the parameter of interest being S_{11}. The VNA was configured to sweep from 1 to 10 GHz within its frequency range, using a 3 MHz step, an IF bandwidth of 10 kHz, and a source power of 13 dBm.

The software utilized in the simulation was FEKO, a commercial electromagnetic solver. Initially, the system was calibrated using an aluminum flat panel. The chosen panel had transverse dimensions of 9.6 cm (width) × 10.3 cm (height) with a thickness of 3 mm. Simulations conducted with the FEKO software were compared to the Physical Optics (PO) solution, revealing similar signal behaviors.

Subsequently, to validate the range, the RCS of a canonical cylindrical target was measured. These measurements were taken at distances of 0.5 m and 2 m. The analysis conducted at 0.5 m demonstrated a strong agreement between the measured and reference RCS, with only a minor loss of accuracy compared to the measurements at 2 m. In the frequency range relevant to UWB radar applications (3 to 10 GHz), the maximum error in the magnitude of the measured RCS was found to be 1 dB. In summary, it was concluded that the RCS test range is suitable for measuring the complex-valued RCS within the explored distance and frequency ranges [23].

After the validation of the RCS test site in [23], a series of RCS measurements were conducted on a female volunteer. For these measurements, the female subject stood on a wooden stool chosen to align the chest wall with the antenna level. Two measurements were performed: one at the end-inspiration and another at the end-expiration breathing phases. These measurements demonstrated that the RCS is significantly influenced by slight movements of the human chest wall resulting from respiratory activity.

It is worth noting that the results of the breath activity monitoring, while obtained in this study, are not the main focus of this dissertation and will not be discussed in this section.

In summary, this study was valuable for this dissertation because it provided important concepts and measurement structure. Firstly, it validated the software used by comparing RCS measurements of well-known shapes. Secondly, it replicated these tests using human subjects. Although the study employed a UWB radar system, the concepts can be applied to a CW radar system as well. However, it is important to mention that the study analysed only the RCS of one subject. In this dissertation, the intention is to measure the RCS of various subjects with different genders, heights, and weights, to observe the impact of these characteristics on the RCS.

2.2.4 79 GHz band RCS Measurement for Pedestrian Detection

In [24], the RCS measurements for pedestrian detection in a 79 GHz band radar system are presented. This measurement was conducted with a human subject standing 6.2 meters away. The objective of this work is to study and address pedestrian-related accidents. A millimeter-wave radar system was installed at an intersection, but an issue arose due to misalignment between the radar's orientation and the frontal direction of the target human. To accurately detect human beings, it is necessary to understand the reflective characteristics of various poses, not just the frontal pose. Therefore, the primary goal of this work is to investigate the human body's reflective characteristics in the 79 GHz band millimeter-wave radar.

The human target was positioned in front of the radar in a stationary state, maintaining a distance of 6.2 meters. The angle between the human body and the radar was set to 0, 45, and 90 degrees, with 0 degrees representing the frontal direction of the human body facing the radar. The experimental setup and environment are illustrated in Figure 2.12. Received power measurements from the human target were compared to those from a spherical reflector target, and the peak values for each scenario were recorded. Subsequently, RCS values were measured for three different positions of the human

body (0, 45, and 90 degrees). The obtained RCS values exhibited variations in all three positions [24].

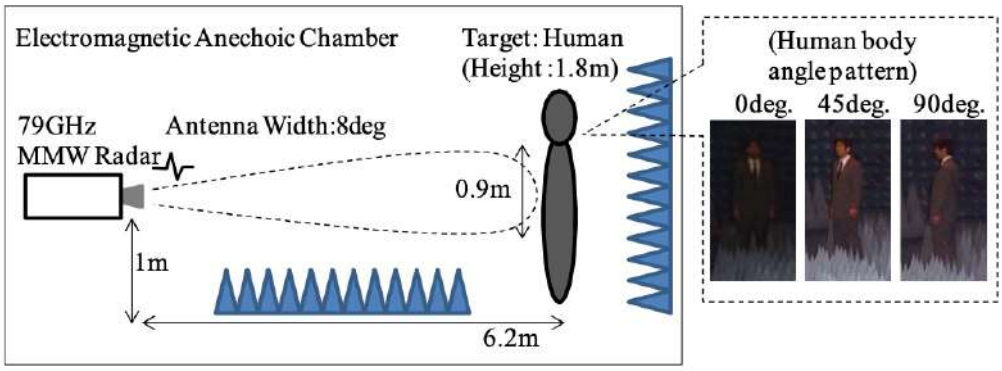

Figure 2.12: Measurement environment [24].

Upon analyzing this work, it became evident that the RCS was different when the target considered was a human subject or a sphere. Also, RCS measurements varied in different positions of the human body. This work shares some similarities with the objectives of the current dissertation, such as analyzing received power and RCS of pedestrians. Nevertheless, it is important to note that the measurements were conducted in a very high-frequency band, and the target was positioned at a significant distance from the radar antennas. Therefore, it was not operating in the near-field region of the target. However, certain applications and insights derived from these measurements can still be applied to the Bio-Radar system used in this research.

2.2.5 Sleep Posture Recognition With a Dual-Frequency Cardiopulmonary Doppler Radar

In the article [25], a dual-frequency (2.4 GHz and 5.8 GHz) Doppler radar system that integrates sleep posture recognition with cardiopulmonary monitoring has been successfully demonstrated. Measurement results from a study involving 20 human subjects were analysed for the recognition of three critical categories of sleep postures. The goal was to develop an approach for recognising three sleep posture categories while simultaneously measuring diagnostic cardiopulmonary patterns using an unobtrusive and non-contact Doppler radar system. Initially, tests were conducted on metallic spherical objects to validate the measured quantities and system accuracy. Subsequently, tests were performed on human subjects [25].

When subjects switch postures, it affects the RCS because different parts of the body become exposed to the radar, conveying cardiopulmonary motion differently [25]. In

principle, RCS measurement using Doppler radar is based on detecting phase modulation caused by a moving target. Since the motion occurs in the direction of the transceiver, the target's range is also modulated by the displacement, resulting in variations in the power of the returning wave [25].

To establish the validity of the measured quantities and test system accuracy, a metallic spherical object was used. The accuracy of RCS measurements depends not only on system sensitivity but also on target alignment. In this experiment, the target was measured in three different positions. First, the target was laterally aligned with the transceiver. Then, the process was repeated with the target shifted two centimetres to the left and two centimetres to the right [25]. Various tests were performed, and digital processing algorithms were applied to extract the RCS and displacement magnitude of the torso during respiration. The measurements of the metallic spherical targets, which modeled expected human respiratory motion, indicated that these two quantities can be effectively measured with acceptable accuracy [25].

Subsequently, tests were conducted using human subjects. A total of twenty subjects (6 females and 14 males) were included in the study. The body mass index varied from 19 to 31.8 kg/m2, with 8 subjects having a normal weight, 11 being overweight, and one being obese [25]. Each subject was measured in three recumbent postures: supine, prone, and side. Inside an anechoic chamber, each subject was instructed to wear effort belts and a finger pulse strap for reference measurements, and then lay down on a flat horizontal surface. The transceiver antennas were suspended above the subject using the chamber's ceiling, at a range of 2.05 m [25].

The results showed that the RCS in the prone posture was consistently greater than that in the supine posture for measurements performed at 2.4 GHz. This observation was less pronounced for the 5.8 GHz system due to the spherical nature of the incident wave at the relatively short target range, resulting in reduced sensitivity to target curvature. Conversely, the effective RCS in the side posture was smaller than that in the supine posture for most subjects at both 2.4 and 5.8 GHz.

In addition to these findings, the study also developed a decision algorithm to explore the potential for identifying a subject's orientation based on the measured RCS and torso displacement magnitude. The proposed method successfully distinguished between three distinct recumbent postures in a study involving twenty participants within an anechoic chamber [25].

2.2.6 Radar Cross Section of Human Cardiopulmonary Activity for Recumbent Subject

In this paper, the RCS corresponding to human cardio-respiratory motion is measured for a subject in two different recumbent positions: lying face up (supine) and lying face down (prone) [26]. Doppler radar is employed due to its high potential for monitoring the cardiopulmonary behaviour of remote human subjects. The Doppler radar motion sensor typically uses continuous wave illumination of the subject. The reflected wave backscattered off the subject's torso is phase-modulated by the torso's movement, resulting from the Doppler effect [26], which is the same principle used in the Bio-Radar system. Experiments were conducted to describe the RCS associated with respiration and heartbeat, as well as its dependence on subject orientation.

The setup used in the measurements has separate but similar transmitting and receiving antennas to minimise Tx to Rx coupling. Two measurements were taken on a 30-year-old male subject in the lying position. In the first measurement, the subject was comfortably lying on his back (supine), with the transmitting and receiving antennas suspended above him at a vertical distance of 1.82 m for 90 seconds. In the second measurement, the subject was lying face-down (prone) with his back facing the transceiver antennas. The antenna positions were kept the same, and signals were recorded while the subject was breathing for another 90 seconds [26]. Additionally, two piezoelectric effort belts were used as respiration reference, one for the chest and the other for the abdomen [26].

The main conclusion drawn from this paper is that the respiratory signal obtained when the subject is lying face up (supine) is much more pronounced than when the subject is lying face down (prone). This difference is primarily attributed to the nature of motion on the body surface in these two lying positions. When the subject lies on their back, they can breathe more freely, and all motion, primarily from respiration, is translated to the front and is manifested with higher amplitude. Conversely, when the subject lies face down, the motion of the chest and stomach is translated into a uniform motion of the back but with reduced depth due to the subject's weight [26]. This can be observed in Figure 2.13.

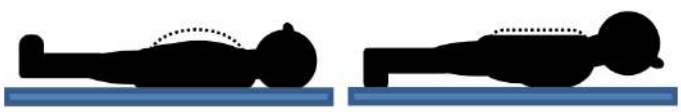

Figure 2.13: Motion Characteristics when subject lies in supine and prone positions, [26].

Another conclusion drawn from this study is that due to this aspect, the effective RCS of the back is nine times larger than that of the front. This increase in RCS can be attributed to the difference in the geometrical shapes of the front and back of the body. The front of the body can be approximated as a cylinder with a radius of curvature roughly equal to half the chest, whereas the back of the body can be considered as a flat surface. In summary, the obtained RCS values suggest modeling the moving part of the upper body as a half-cylinder, where the front is cylindrical and the back is flat. It is expected that the RCS will further differ for other body orientations [26]. However, a comprehensive understanding of this quantity is a necessary step toward enabling extensive quantitative interpretation of cardiopulmonary body motion and other related aspects.

2.2.7 Radar monitoring of heartbeats and respiration

In the thesis presented in [27], the use of radar for heartbeat and respiration monitoring is addressed. The measurements were conducted by using a VNA (Vector Network Analyser) or a UWB radar. Overall, the dissertation in [27] shares similarities in structure with this dissertation. Firstly, it includes a study of the basic principles of the radar used, followed by experiments conducted with human subjects in an anechoic chamber to measure the respiratory signal and the RCS of the subjects.

The main goal was to find an optimal way of detecting heartbeats and respiration in terms of transmitting frequency, aspect angle and signal processing. It was observed that both the heartbeat and respiration modulation increase with increasing transmitting frequency, and are best detected from the front and the back of a person. Also, with the experiments performed, it was showed that it is the chest surface motion that is seen when monitoring the human heartbeats from a distance using radar.

In the experiments conducted in [27], measurements were carried out using both remote monitoring and on-body methods. While both methods yielded results, it was observed that the on-body measurements provided the best results. In this thesis, while there are some shared topics, a more comprehensive examination was not conducted since the detailed aspects were not the primary focus of my dissertation.

2.2.8 EM Modelling of Monostatic RCS for Different Complex Targets in the Near-Field Range

The work presented in [28] involves the evaluation of monostatic RCS responses in the near-field range. This evaluation was carried out for several targets with different and

complex topologies. The primary objective was to develop and validate an efficient tool based on electromagnetic (EM) simulations for characterizing a traffic scenario. These simulations were experimentally validated using a commercial vehicular FMCW radar operating at 24 GHz. The paper introduces a hybrid method that combines the Geometrical Theory of Diffraction (GTD) and Physical Optics (PO) to calculate the RCS of various targets [28].

In this study, monostatic RCS was evaluated in the near-field range to simulate the operation of car radars. To minimise the impact of wall or floor scattering, measurements were conducted in an anechoic chamber. A measurement setup was established, comprising a transmitter, a receiver, and a rotating platform situated at a fixed distance for manoeuvring the target. Consequently, it was crucial to properly calibrate the measurement setup before commencing the data collection process.

To calibrate the measurement setup, a metallic sphere was employed. Subsequently, RCS measurements were conducted for various targets, including simple shapes like a metallic flat plate and a metallic rectangular box, as well as more complex structures like a cavity and a metallic Electromagnetic Band Gap (EBG) structure. Additionally, measurements were taken for an airplane mock-up and a human body. The configuration of the setup used in the anechoic chamber for RCS measurements is depicted in Figure 2.14. It is important to note that, for the purposes of this dissertation, only the analysis of simple target shapes and the human body will be conducted, as they constitute the primary focus of the study.

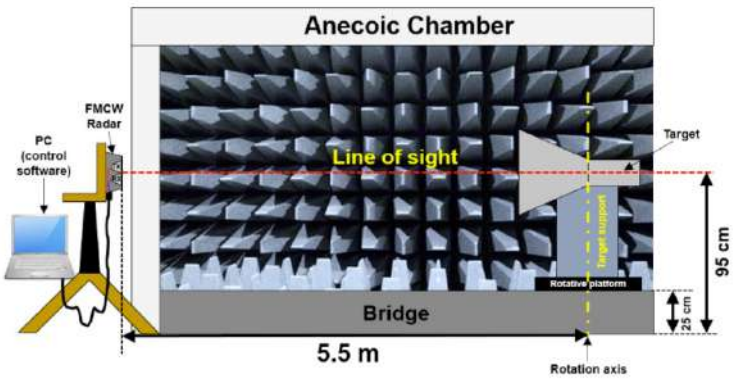

Figure 2.14: Schematic view of the measurement setup [28].

The main conclusion drawn from this work is that the EM method, which combines the GTD and PO methodologies to characterize a traffic scenario, has been proven to be valid. However, for the purposes of this dissertation, an alternative method has been chosen. This decision is based on the availability of other validated methods in

the literature, supported by extensive research. The methods used for theoretical RCS calculations are detailed in [16].

Regarding the chosen approach for RCS analysis, the system was initially calibrated using simple targets such as metallic flat plates, and subsequently, the system's performance was evaluated with more complex targets, including human subjects. This same approach will be applied in this dissertation. The initial step involves simulating scenarios with well-known shapes and comparing the results with theoretical equations. Subsequently, practical measurements will be conducted in an anechoic chamber to validate the process. This procedure will then be replicated using both dummy targets and human subjects. The work related to the RCS analysis of well-known shapes for calibration and software validation is presented in Chapter 3.

3

Simulation Software: Selection and Validation

In this chapter, the main goal was to describe the conditions as well as the platforms used to perform the simulations. Also, to describe the used setup for validation of the practical measurement process. Similar to the related works presented in Section 2.2, the first approach involved determining the RCS of targets with well-known shapes through simulations. This analysis with well-known shapes served a dual purpose: validating the simulation software (by comparing theoretical equations with simulation results) and subsequently validating the practical measurement process.

3.1 Selection of the simulation software

There are various software programs capable of simulating radar systems. Two examples of simulation software are SIMULIA from 3DEXPERIENCE® and WaveFarer from REMCOM®. For this dissertation, a license was obtained for the software WaveFarer and this was the software used all throughout the simulations performed in this work. This software allows for the simulation of moving targets, which is particularly relevant for Bio-Radar applications since the antennas are stationary and emitting signals to moving targets.

3.2 Validation of the simulation software

The accuracy of the Bio-Radar signal depends on received power, which can be inferred using the radar equation [13]. The radar equation, presented in equation (2.3) in Chapter 2, takes into consideration the transmitted power, the antenna gain, the distance, and the target's RCS. The radar system used in all the tests is parameterised as shown in Table 3.1, where P_t represents the transmitter power, G_r is the gain of the receiver antenna, G_t is the gain of the transmitted antenna, f is the operating frequency, and $HPBW$ is the Half Power Beam Width. The transmitted signal is a sinusoidal wave with a frequency of 5.8 GHz.

In the simulations, two directive antennas were positioned in front of the moving target, and the radar operated at 5.8 GHz in CW mode. The setup used is consistent with the parameterisation in Table 3.1. Figure 3.1 presents the antennas used in the Bio-Radar system.

Table 3.1: Parameterisation of the radar system

P_t	G_r	G_t	f	$HPBW$
7 dBm	12.2 dBi	12.2 dBi	5.8 GHz	42°

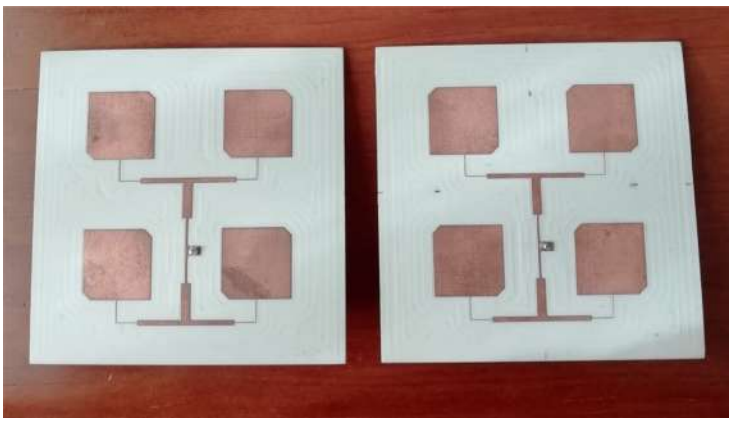

Figure 3.1: Antennas used in the Bio-Radar system.

The first set of simulations was performed using well-known shapes. This approach aimed to conduct a controlled analysis, not only for RCS but also for received power. The received power and the measured RCS were verified while varying the distance between the target and the antennas within the range of 0.5 to 2 m. The simulations were carried out on three well-known shapes with different dimensions. The first target was a circular plate with a radius of 0.25 m, the second target was a square plate

with dimensions 0.4 × 0.4 m, and the third target was a rectangular plate with dimensions 0.4 × 1 m. Each of these targets is presented in Figure 3.2.

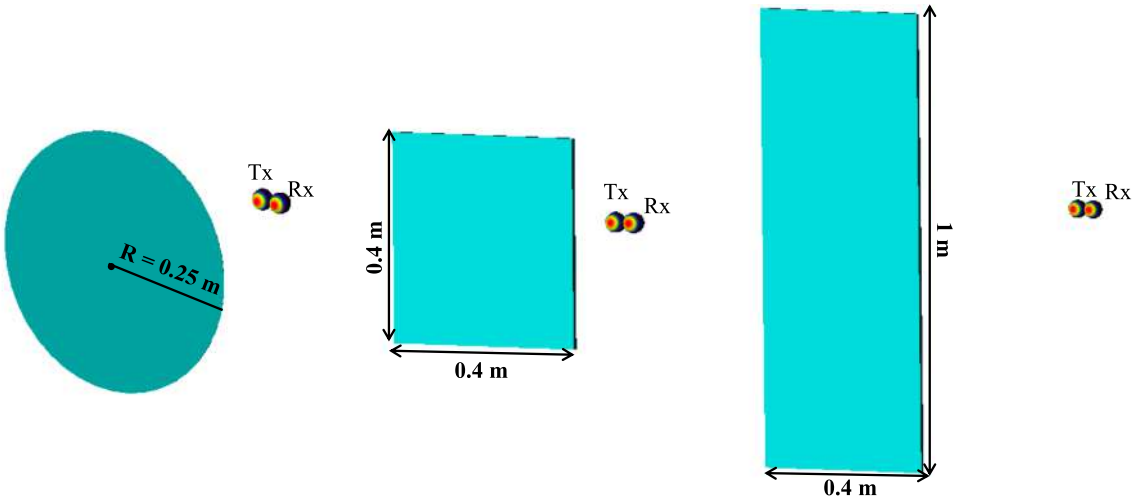

Figure 3.2: Well-known shapes targets.

The simulations were performed using the software WaveFarer, which gives the received power. The RCS was calculated according to the radar equation (2.3), and compared to the RCS obtained from the theoretical equations, given by (2.6), (2.7) and (2.8). The results obtained are presented in Figure 3.3, where the full coloured lines represent the simulated results and the dotted lines represent the theoretical results. These results were simulated in a range of 0.5 m to 2m since this is the typical range used in Bio-Radar applications.

The received power decreases with distance, and the RCS increases with distance, as expected. Regarding the three different target shapes, it can be observed that the circular target, in comparison with the square and rectangular targets, exhibits more pronounced local minimum (LM) around 0.6 m and 1.2 m. However, both the square and rectangular targets also show LMs around 0.8 m, although not as pronounced as the circular target. When comparing the theoretical RCS results with the simulated ones, all simulated results exhibit a similar behaviour to the theoretical results. In the case of the circular target, the simulated results start converging to the theoretical value only after 1.3 m. However, the LMs occur at the same distance in both the simulated and theoretical results. It is worth noting that an LM appears around 0.6 m and 1.2 m, although it is not as pronounced as in the theoretical equation. This could be a result of the fact that the theoretical equation does not account for the diffractions that occur at the edges of the target shape.

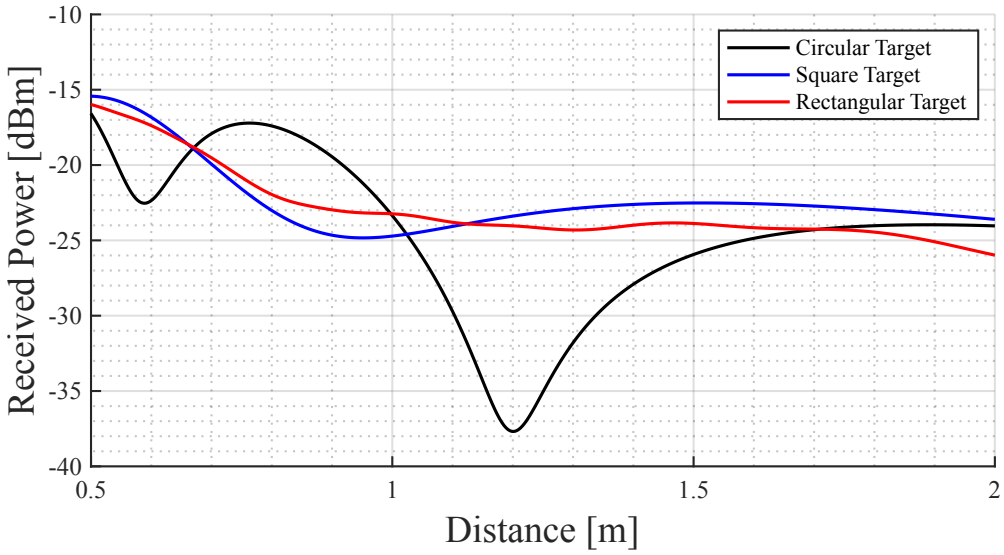

(a) Received Power

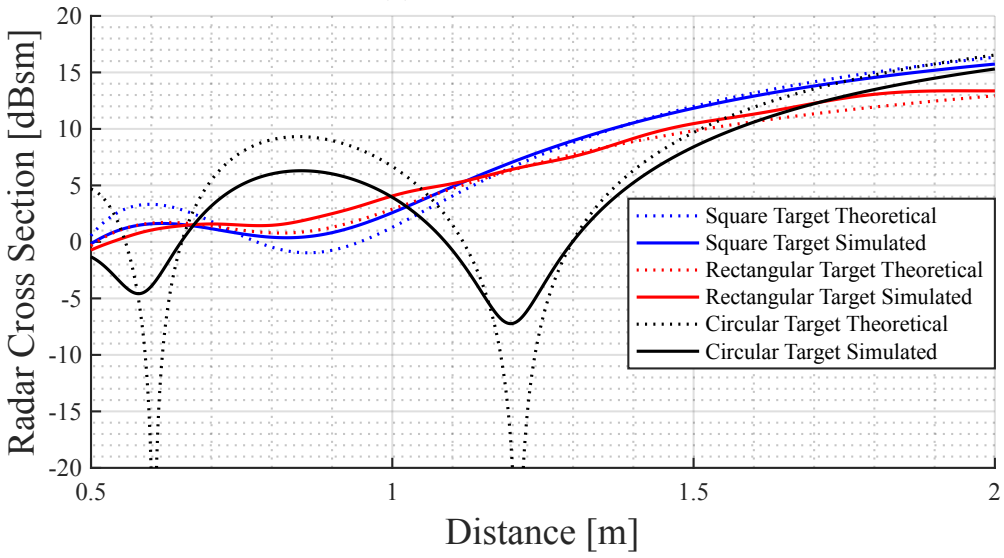

(b) RCS

Figure 3.3: Received power and RCS variation according to the distance in well-known shapes.

In the simulation of the rectangular target, the directive antennas were aligned with the center of the object. If is considered that the rectangular target resembles the shape of the human torso, this placement does not correspond to the positioning of the chest-wall. Therefore, the next analysis compares the received power and RCS of a rectangular target when the antennas are aligned above the center of the shape, where the chest wall would presumably be. Altering the position of the antennas not only affects the received power but also the RCS. These differences are more pronounced within the range of 0.9 m to 2 m, as can be observed in Figure 3.4.

Despite possible analytical differences, it can be concluded that the software is valid.

The next step is to validate the practical measuring process, using an anechoic chamber. This process is described in section 3.3.

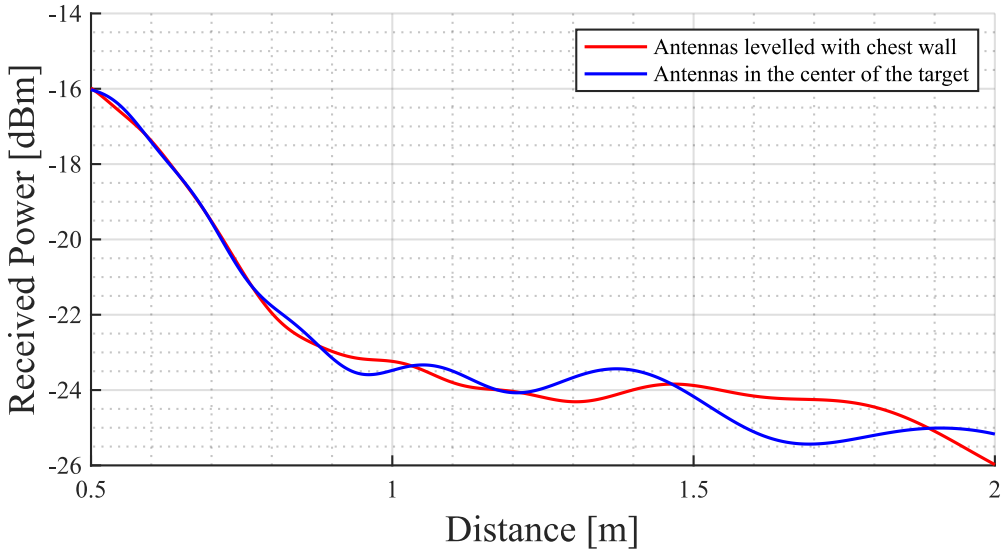

(a) Received Power

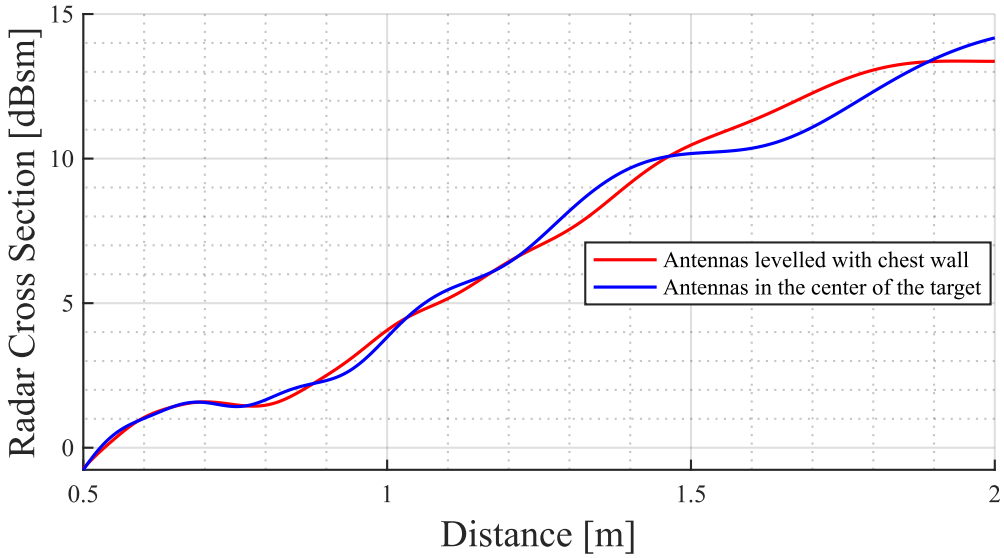

(b) RCS

Figure 3.4: Received power and RCS variation according to the distance - Antennas centred vs not centred.

3.3 Validation of practical measurements in comparison with the simulation software

As the results obtained through the simulation were consistent with the results obtained through the theoretical equations, the next step taken was to perform practical

measurements in the anechoic chamber in order to observe if the practical results are coherent with the results obtained from the simulation software. An anechoic chamber can be defined as a chamber developed to reduce unwanted reflected energy by using absorber materials, providing a 'virtual' free-space testing chamber. This room is used to perform a variety of antenna measurements, electromagnetic interference (EMI) measurements, and electromagnetic compatibility (EMC) measurements while providing minimal interference from external sources [29].

The aim of going to the anechoic chamber was to replicate the results obtained in simulations. The experiment was performed only with one of the well-known shapes. The shape chosen was the circular target, as it exhibits more pronounced LMs. The radius of the circular target was 0.25 m. It is also important to mention that the target was made of aluminium alloy.

Before proceeding with tests in the anechoic chamber, it is crucial to conduct a preliminary study. It is important to note that the setup is assembled by hand, which implies human error, even if it is done very carefully.

Thus, the impact of having the antennas perfectly centred with the target's center, as well as the impact of tilting a target, was studied in preliminary tests. Both of these preliminary tests are shown in Figures 3.5 and 3.6. As for the obtained results of these two tests, they are illustrated in Figure 3.7.

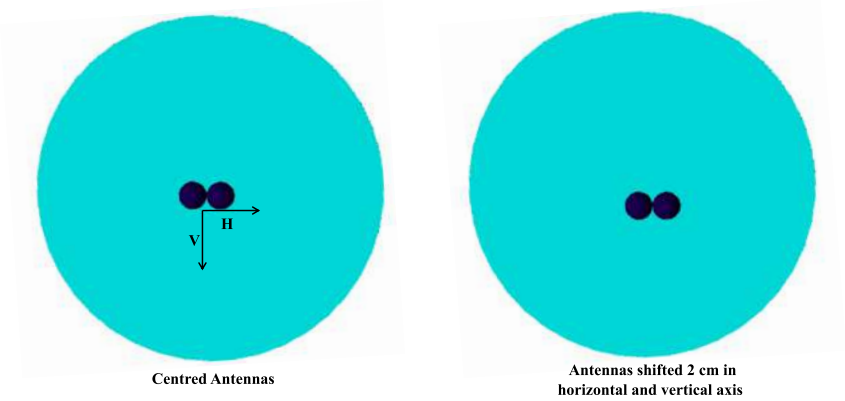

Figure 3.5: Test of the centred antennas.

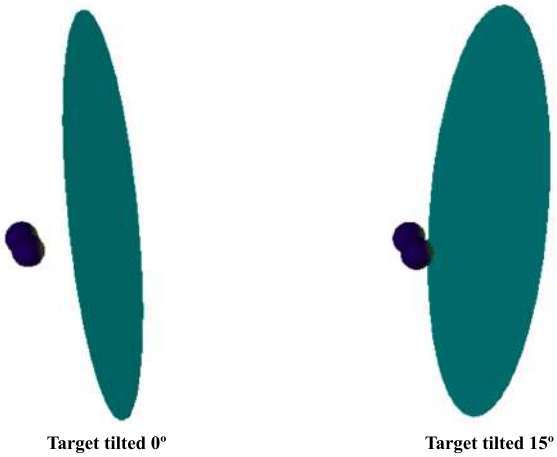

Figure 3.6: Test of the tilt.

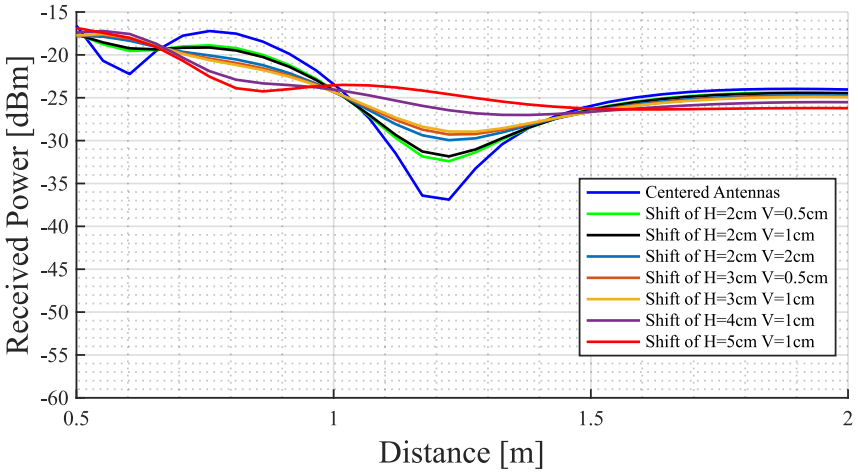

(a) Test of the centred antennas

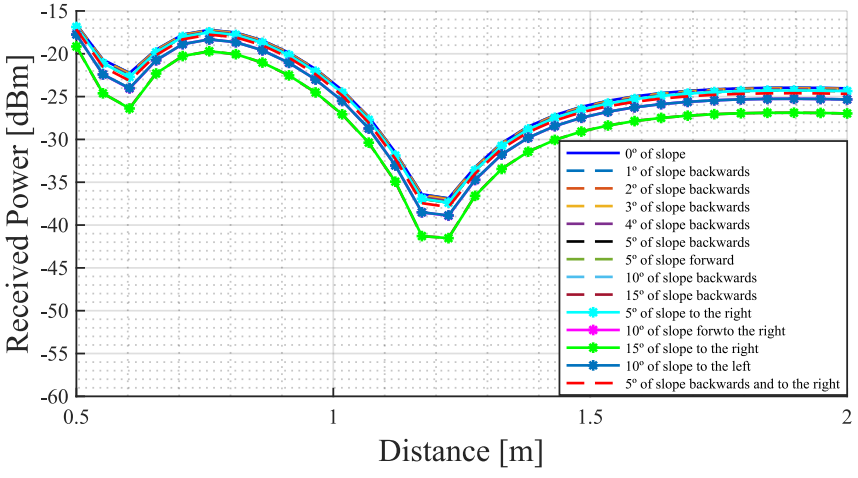

(b) Test of the tilt

Figure 3.7: Received power variation according to the distance with the target shifted and tilted in relation to the antennas.

The conclusions drawn from this study were that a deviation, in both the horizontal and vertical planes, of 2 cm or more from the center of the target had a drastic impact on the received signal. As can be observed in Figure 3.7a, especially in the signal represented by light blue, a shift of 2 cm or more in both the horizontal and vertical planes can cause the last, more pronounced LM to disappear entirely. Regarding the tilt, as seen in Figure 3.7b, tilting the target in different directions (up to 15°) does not have a significant impact on the signal behaviour. Although there is a slight difference in the magnitude of the received power, the signal behaviour remains the same.

With all these preliminary tests carried out, and now considering that there is a margin of error of 2 cm when trying to center the target with the antennas, it was possible to move on to experiments in the anechoic chamber. The setup used is illustrated in Figure 3.8, and all measurements in the anechoic chamber were performed with a VNA (Vector Network Analyzer).

Figure 3.8: Setup used in the anechoic chamber.

In the tests performed in the anechoic chamber, a VNA was used to analyse the S_{21} parameter, in order to obtain the received power. In order to explain the procedure conducted to determine the received power from the S_{21} measurement, three equations are presented. The S_{21} represents the power transferred from port 1 to port 2. This parameter can have many components that need to be isolated in order to obtain the desired component. These components are illustrated in Figure 3.9. All the following procedure was performed in the VNA.

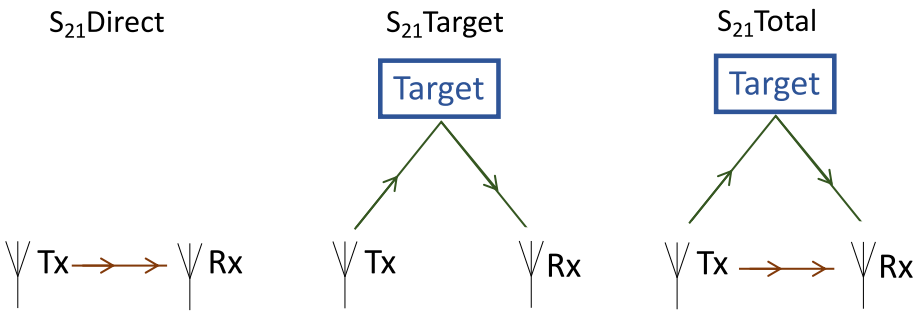

Figure 3.9: Representation of the various components of the S_{21} parameter.

In equation (3.1) is represented the $S_{21\,\text{Direct}}$ in linear, where the received power obtained directly from the transmitter antenna is $P_{Rx\text{Direct}}$ and P_t is the transmitted power. This equation represent the mutual coupling between both antennas.

$$S_{21\,\text{Direct}} = \frac{\sqrt{P_{Rx\text{Direct}}}}{\sqrt{P_t}} \tag{3.1}$$

In equation (3.2) is presented the $S_{21\,\text{Target}}$, which represents the relation of power transmitted towards the target and the received power, which is given by $P_{Rx\text{Target}}$.

$$S_{21\,\text{Target}} = \frac{\sqrt{P_{Rx\text{Target}}}}{\sqrt{P_t}} \tag{3.2}$$

If the contributions from the $S_{21\,\text{Direct}}$ and the $S_{21\,\text{Target}}$ are added, a new S_{21} emerges. This parameter is the $S_{21\,\text{Total}}$ and is presented in equation (3.3).

$$S_{21\,\text{Total}} = \frac{\sqrt{P_{Rx\text{Direct}}} + \sqrt{P_{Rx\text{Target}}}}{\sqrt{P_t}} \tag{3.3}$$

The values of S_{21} measured by the VNA are presented in equation (3.4). It can be observed that $S21_{\text{Final}}$ has the same value of the $S21_{\text{Target}}$.

$$S21_{\text{Final}} = S21_{\text{Total}} - S21_{\text{Direct}} = \frac{\sqrt{P_{Rx\text{Direct}}} + \sqrt{P_{Rx\text{Target}}} - \sqrt{P_{Rx\text{Direct}}}}{\sqrt{P_t}} = \frac{\sqrt{P_{Rx\text{Target}}}}{\sqrt{P_t}} \tag{3.4}$$

All the previous equations were expressed in linear. The next step taken was to put the $S21_{\text{Final}}$ in dB. The main goal is to convert $S21_{\text{Final}}$ into received power, in order to compare the simulated results with the results obtained from the anechoic chamber. The equation obtained is presented in (3.5), where $P_{Rx\text{Target}}$ and P_t are already expressed in dB.

$$S21_{\text{Final}}(dB) = P_{Rx\text{Target}} - P_t \tag{3.5}$$

Regarding the experiment, the same procedure was carried out in the anechoic chamber as in the simulation, where the antennas were stationary, and the target was moving towards the antennas, stopping at different distances. This procedure was performed with the target placed on a platform with wheels, which stopped at different distances to measure the S_{21} parameter. First, before going to the anechoic chamber, the received power was simulated in the WaveFarer software with the same aluminium target and the same distances traveled. This was done so that the results could be directly compared. In the anechoic chamber, at each distance, the $S_{21\text{Final}}$ parameter was measured for 10 seconds. This procedure was carried out to obtain a more accurate $S_{21\text{Final}}$.

In Figure 3.10, the received power is represented according to the distance when comparing the simulated results with the mean value as well as the standard deviation for each distance. The standard deviation was considered important to take into account because it quantifies the amount of dispersion in a set of values, providing a better understanding of how the values are spread around the mean value. The measurements were taken from 0.5 m up to 2 m. As can be seen, the results obtained from the anechoic chamber are consistent with those obtained from the simulation. At 1.18 m, the standard deviation obtained was greater than at any other distance, indicating that at this distance, there is a possible zone for a most pronounced LM. For this reason, this distance could be one to avoid when taking measurements for this specific target.

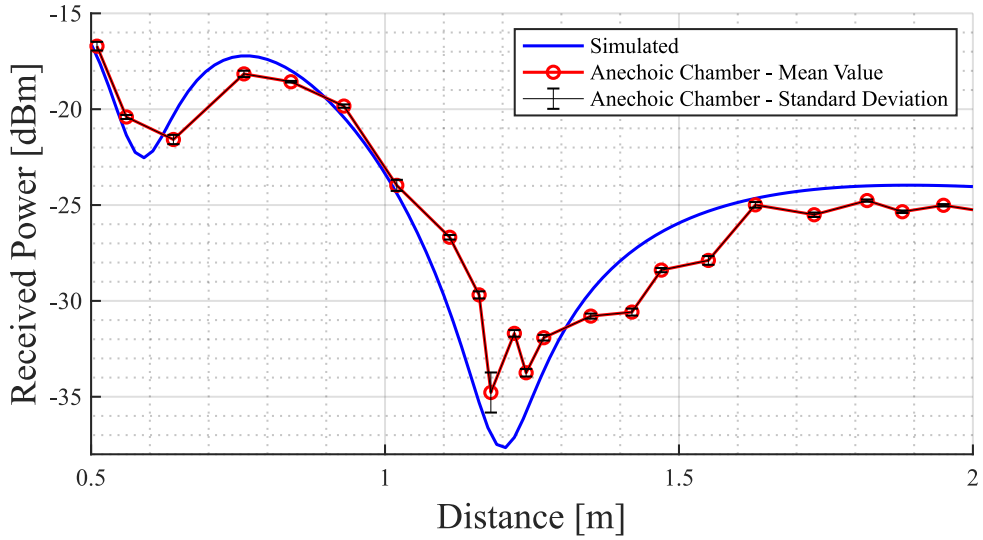

Figure 3.10: Received power variation according to the distance - Circular Target simulated values in comparison with the values from the anechoic chamber.

Afterwards, the mean received power value was used to determine the corresponding RCS. The received power as well as the RCS are presented in Figure 3.11, where the blue line represents the simulated results, the black line represents the theoretical RCS result for a circular target, and the red line with circular markers represents the test performed in the anechoic chamber.

It can be seen that the behaviour of the signal is very similar in both the simulated results and the practical results. The more pronounced LM is located around 1.2 m, as stipulated in the simulation. However, the LM is not quite as pronounced in the practical measurements as in the simulation or even when compared to the theoretical results. The values start converging around 1.7 m, as also seen in the simulation.

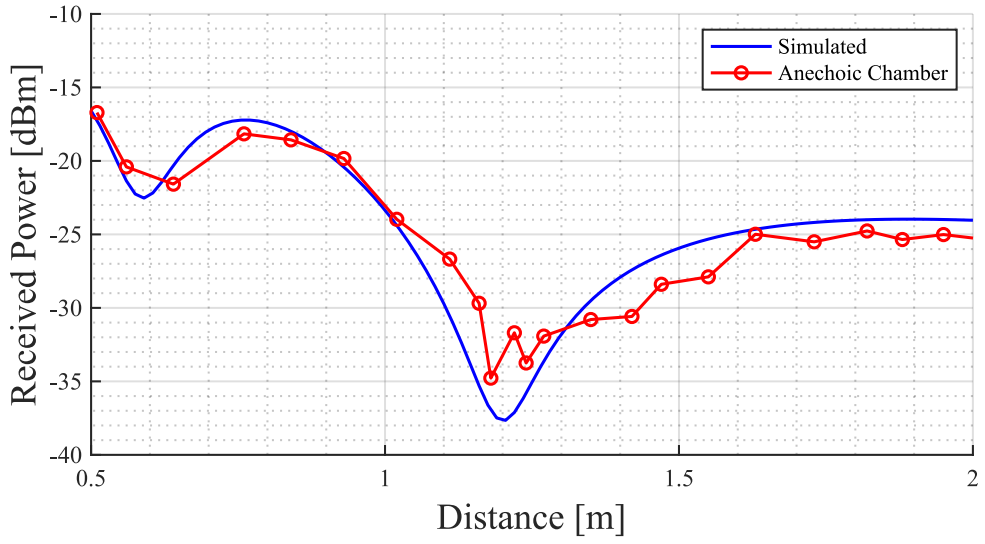

(a) Received Power

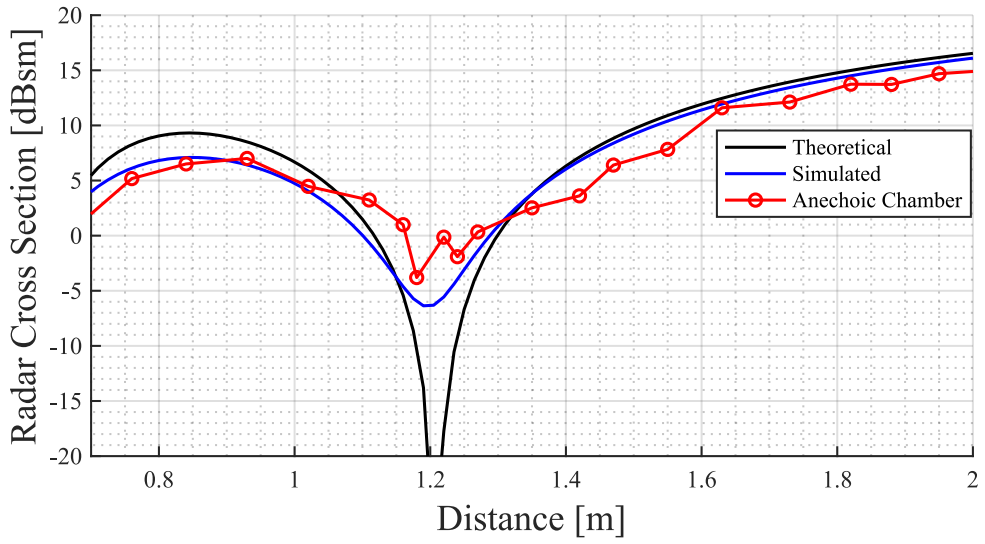

(b) RCS

Figure 3.11: Received power and RCS variation according to the distance - Values from the simulator and the anechoic chamber.

With the presented results, it is possible to conclude that the simulator used has been validated and can be used to perform simulations with various targets in the near-field region of the target. Additionally, the practical measuring process was also validated. With this study of the well-known shapes concluded, it is possible to proceed with simulations involving 3D CAD subjects.

4

Study of the received power and RCS of 3D subjects

Previously, in Chapter 3, the simulation software and the practical measurement process conducted in the anechoic chamber were validated using well-known shapes. In this chapter, the study of received power and RCS was performed on various 3D CAD subject models. The goal of studying different targets with various genders, heights, weights, and other characteristics was to determine an optimal measurement distance for each target to capture the respiratory signal accurately. Additionally, the aim was to observe the behaviour of the LM and its respective impact on the received signal.

4.1 Simulations with Young Male CAD subject

The first set of simulations was performed on a young male 3D subject with a height of 1.76 m. In these simulations, various parameters were tested to evaluate their impact on the received power and RCS. The goal of this study was to gain a better understanding of the LMs behaviour when specific parameters are changed. This 3D subject target is presented in Figure 4.1, where the antennas were aligned with the diaphragm, and R represents the distance between the antennas and the target.

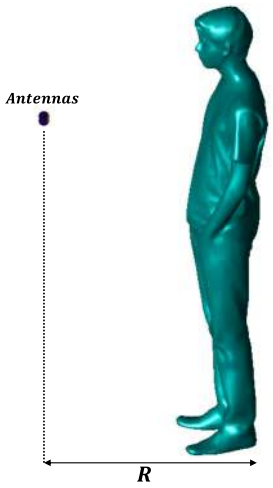

Figure 4.1: 3D Young Male subject model.

4.1.1 Dielectric properties of the subject

The first approach taken towards this subject was to study different types of materials that could be associated with the subject to carry out the simulation. The 3 materials considered were PEC, Skin and Muscle. The dielectric properties of the Skin and the Muscle at 5.8 GHz are presented in Table 4.1.

Table 4.1: Dielectric properties of the Skin and Muscle at 5.8 GHz, [30].

	Dielectric permittivity ϵ_r	**Electrical Conductivity σ (S/m)**
Skin	35.114	3.717
Muscle	48.485	4.9615

The comparison between these three materials is presented in Figure 4.2, where the received power and RCS are analysed according to the distance. The subject coated with the PEC material exhibits higher received power and RCS in comparison to the other two materials. This is attributed to the fact that PEC is often considered a perfect reflector for electromagnetic waves. In addition to the differences observed in the magnitude of the received power and RCS, the behaviour of the received signal remains similar when changing the material covering the subject. Since the dielectric properties of the skin and muscle do not have a significant impact on the signal behaviour, all subsequent simulations were performed using the PEC material.

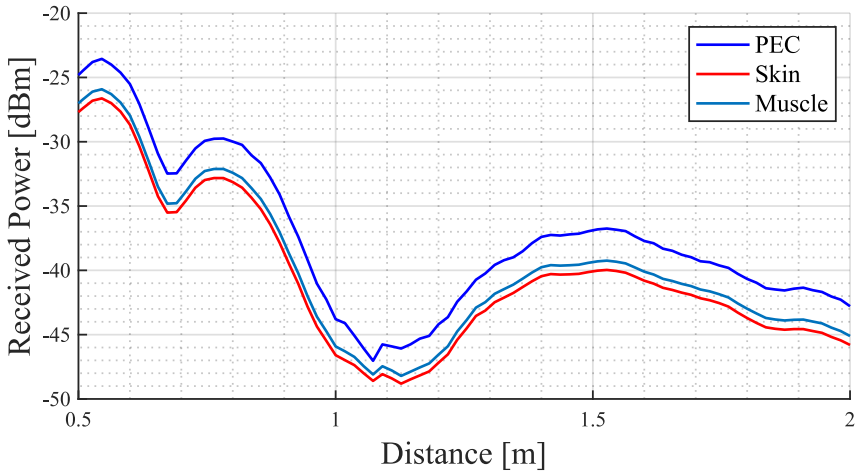

(a) Received Power

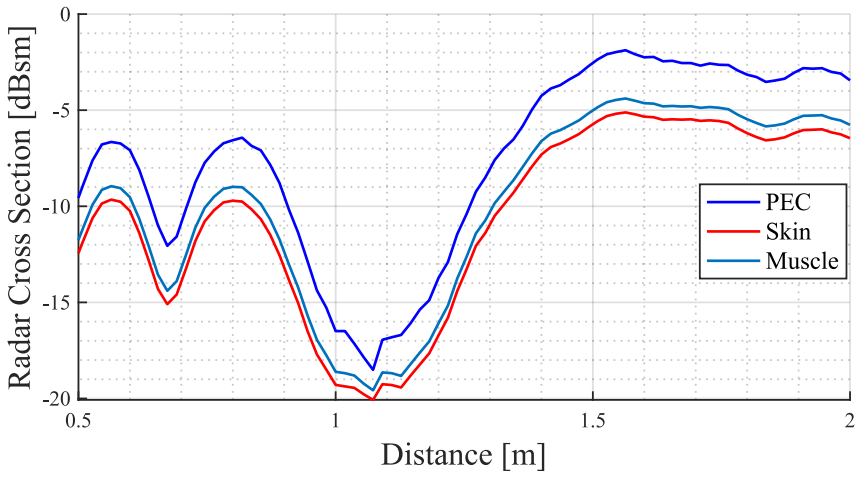

(b) RCS

Figure 4.2: Received power and RCS variation according to the distance when changing the material covering the subject.

4.1.2 Far-field validation

The second test performed involved the measurement of the received power and RCS while varying the distance between the subject and the antennas, within the range of 0.5 to 200 m. This simulation was performed up to 200 m because it was intended to observe if the software simulated the far-field region in agreement with the equation. The far-field region can be determined by equation (2.4), previously discussed in Chapter 2, according to [13]. The obtained results are shown in Figure 4.3.

By analysing the graphs in Figure 4.3, it can be observed that the received power decreases almost linearly but oscillates highly on the first 10 m, having a more constant behaviour afterwards. The same behaviour occurs with the RCS and both have a pronounced LM around 1 m. As previously mentioned, the far-field region can be defined

as where it is possible to measure the RCS with a variation less or equal to 1 dB [14]. Considering such definition, the far-field region for this specific target, with biggest dimension (height) of 1.76 m, starts at 120 m, according to equation (2.4). As it can be observed, the simulation is coherent with the results acquired through the far-field criterion because from 120 m forward, the RCS varies less than 1 dB. From the results presented in this simulation, one valuable aspect taken from it is that, most likely, the Bio-Radar system always operates in the near-field region, regarding the target's point of view, due to the target's dimension.

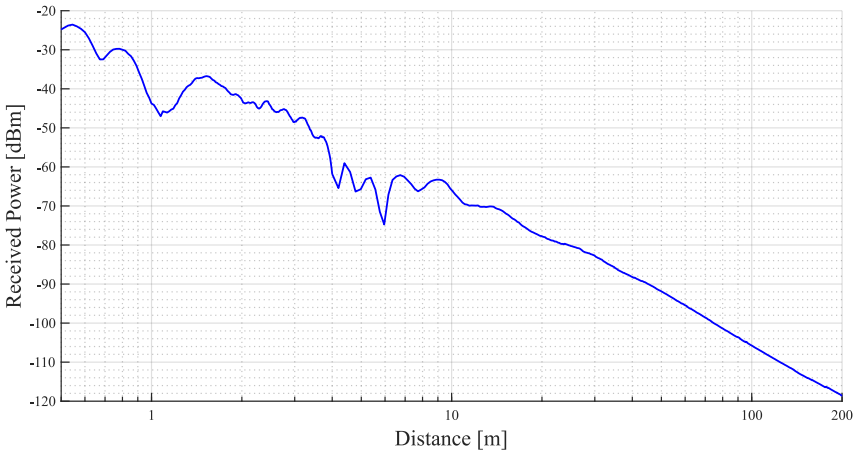

(a) Received Power

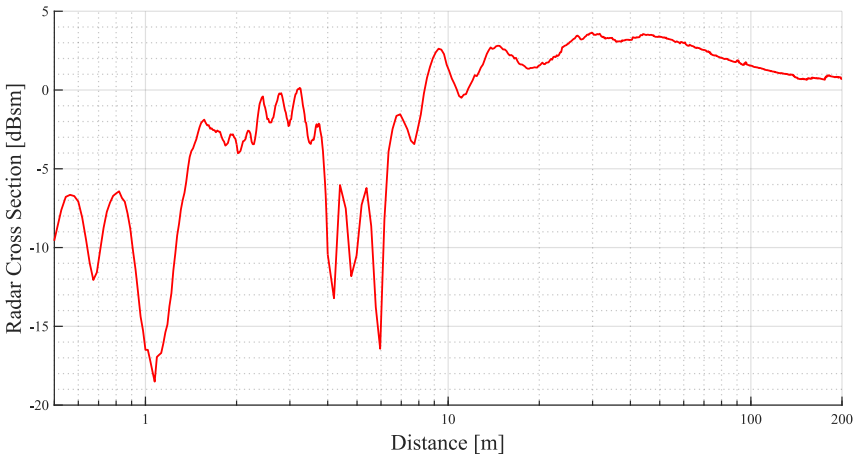

(b) RCS

Figure 4.3: Received power and RCS variation according to the distance - 3D Young Male target.

4.1.3 Variation of the antenna aperture and transmitted power

To better understand the appearance of LM, a study was conducted involving variations in the antenna aperture and transmitted power. In the previous simulations, the

antenna's half-power beamwidth (*HPBW*) was set at 42°, and the transmitted power was 7 dBm. The antenna aperture was then narrowed to 10°, and the transmitted power was increased to 10 dBm.

To gain insight into the antenna aperture's coverage area on the target, simple trigonometry was employed. The results obtained for both a 42° aperture and a 10° aperture are presented in Figure 4.4.

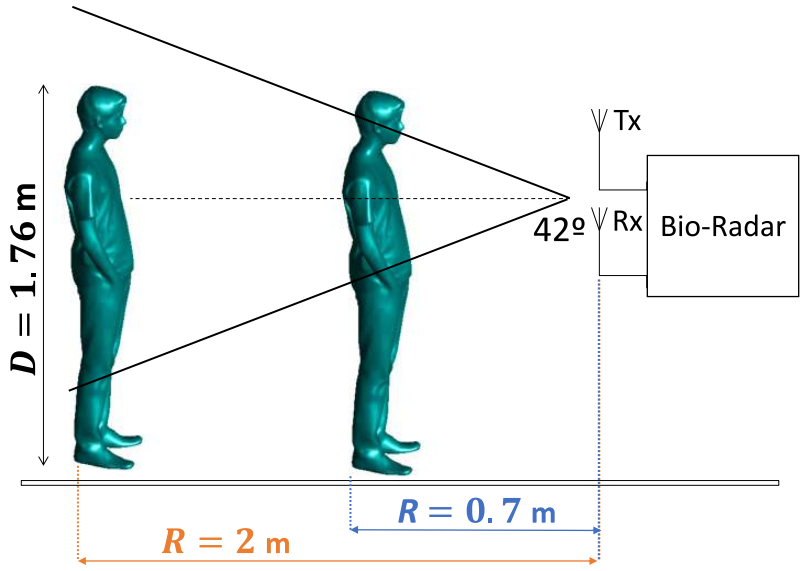

(a) *HPBW* = 42°

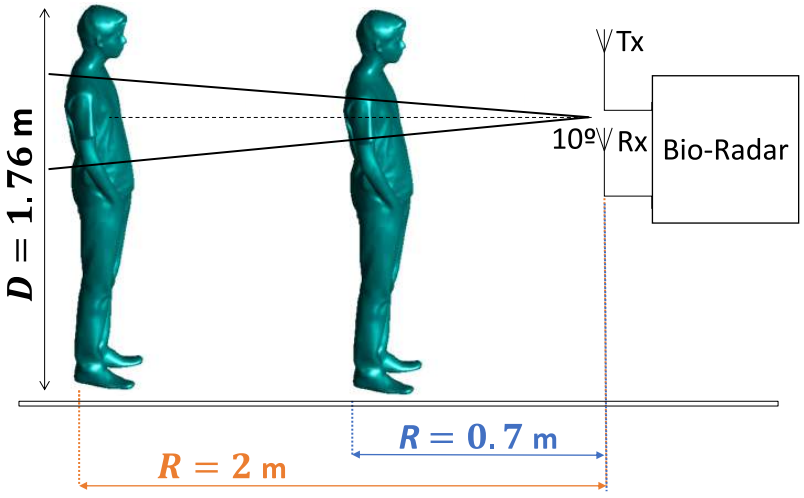

(b) *HPBW* = 10°

Figure 4.4: Variation from an antenna aperture of 42° to 10°.

It can be observed that an aperture of 42° covers a larger area of the subject compared to an aperture of 10°. With a 42° aperture at a distance of 2 m, the measured signal takes into account almost the entire form of the subject, as opposed to only capturing the chest-wall area, which is the case with a 10° aperture at the same distance. The

received power and RCS obtained for these results are presented in Figure 4.5. Reducing the antenna aperture to 10° decreases the occurrence of LM. When the transmitted power is increased from 7 dBm to 10 dBm, the received power increases by 3 dBm accordingly. The RCS in these circumstances exhibits the same behaviour because it is not dependent on the transmitted power. In future practical experiments, although the radar's antenna aperture will remain at 42°, if there is a need to increase the transmitted power (P_t), this change will not impact the signals behaviour.

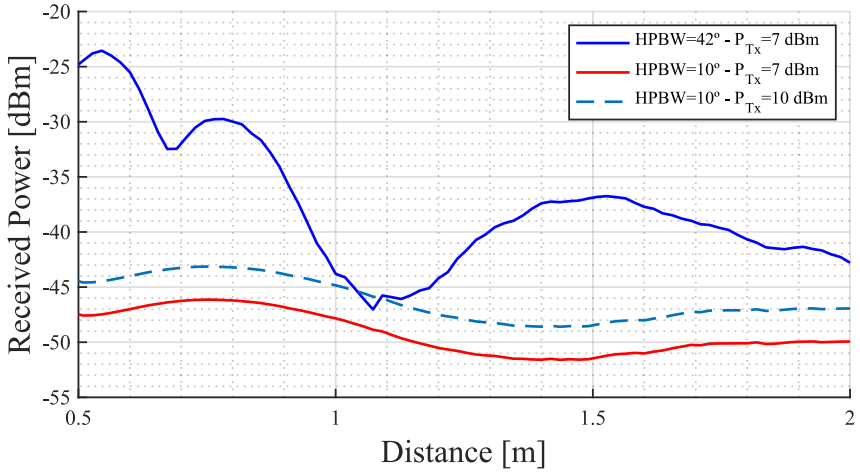

(a) Received Power

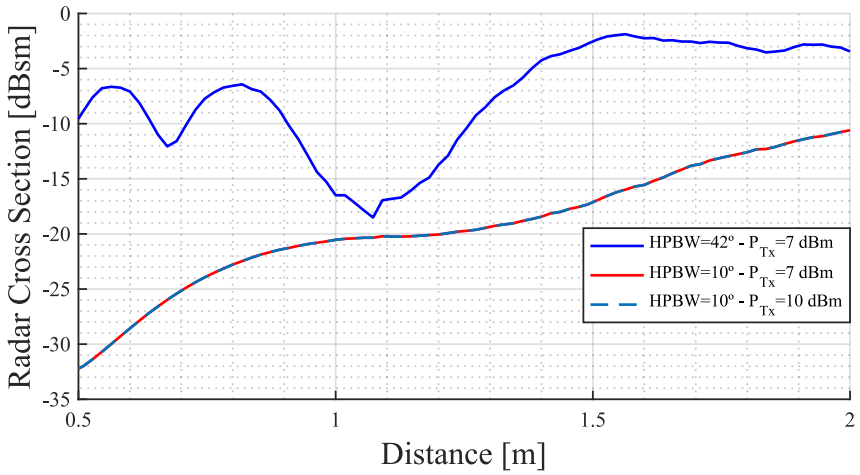

(b) RCS

Figure 4.5: Received power and RCS of 3D young male subject while varying the antenna aperture and the transmitted power.

4.1.4 Impact of certain parts of the subject's body

To further understand the impact of certain parts of the subject's body, such as the legs, on received power and RCS, a rectangular object made of a perfect absorber was placed in front of the subject's legs. As illustrated in Figure 4.4, with an HPBW of 42°,

the legs have an impact on the received signal from a certain distance. The objective of this study is to determine at what distance the legs have an impact, providing valuable information for future experiments conducted in the anechoic chamber. The results are presented in Figure 4.6.

As observed, both received power and RCS converge to approximately the same value before reaching 1 m. Beyond 1 m, the results diverge slightly because the torso and arms of the subject reflect all the transmitted power, as the legs are covered with an object made of a perfect absorber. When the subject's legs are covered, the occurrence of LM around 1.2 m becomes more pronounced.

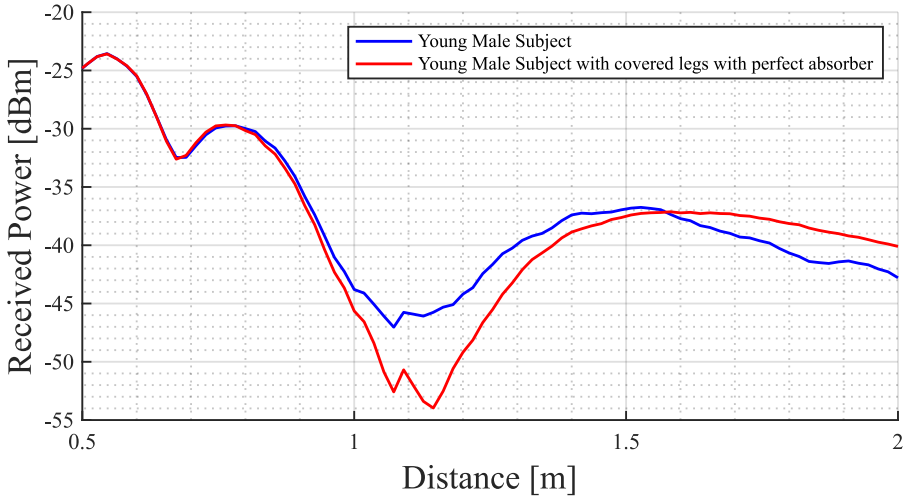

(a) Received Power

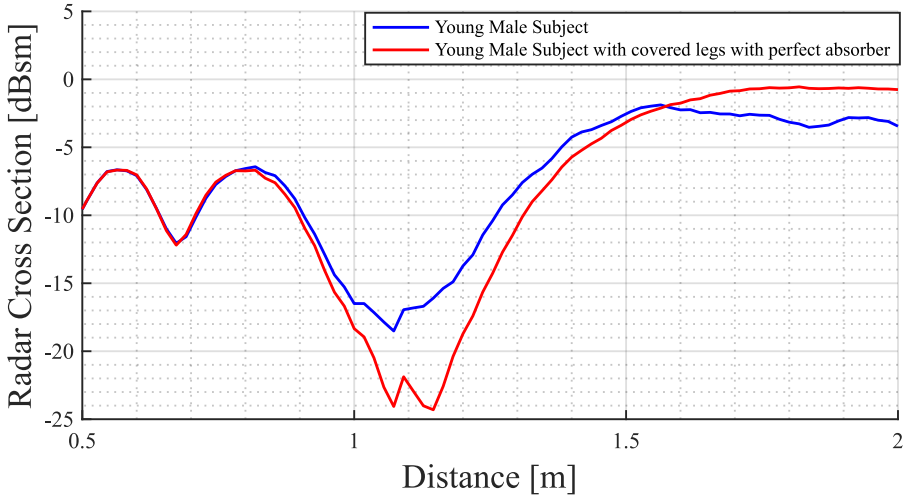

(b) RCS

Figure 4.6: Received power and RCS of a 3D young male subject while a rectangular perfect absorber object covers the legs.

4.1.5 Impact of the chest-wall on the received signal

The next aspect considered important to evaluate was if a slight change of the position of the chest-wall had a significant impact on the received signal. This is a similar study performed regarding the position of the circular pate target in Figure 3.7. For that goal, the received power and the RCS were measured as the subject was rotated 5° around a horizontal axis and a vertical axis. The rotations performed are illustrated in Figure 4.7 and the obtained results are presented in Figure 4.8.

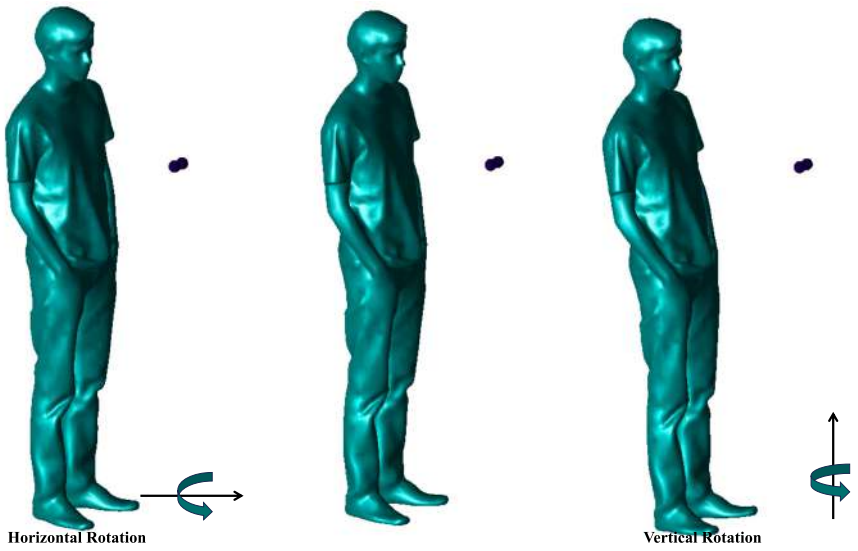

Figure 4.7: Rotation of the subject.

According to the graphs, it can be seen that rotating the subject around an axes does not change the behaviour of the signal obtained, it only shifts the LM. However, a more pronounced LM is presented in the horizontal rotation around 1 m. A valid explanation for this phenomenon is that by rotating the subject, the antennas may have picked up a slightly rounder part of the body, as perhaps rounder objects might cause more pronounced LM .

A similar analysis has already been performed previously in Chapter 3 with a circular target. It was observed that rotating the target in various directions did not have a huge impact on the signal behaviour, however the received signal shifts as the rotation angle increases. These were not exactly the same results obtained in the simulation with the circular plate target. However, it is important to take into consideration that the circular target is different from the 3D subject's target, as the circular target used is uniform and perfectly smooth, which is not the case with the 3D subject. With this study, was possible to observe that even the slightest change on the rotation of the torso

or the position of the subject can cause variation in the received signal. Although the behaviour of the signals stayed more or less the same with these slight variations, the LM occurred at slightly different positions and in some cases it was more pronounced than others. So, it is important for the subject in future practical experiments to maintain the position and posture as still as possible.

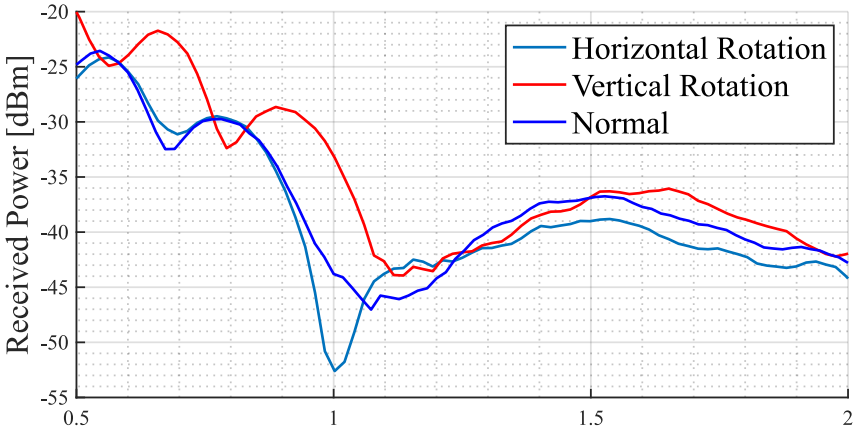

(a) Received Power

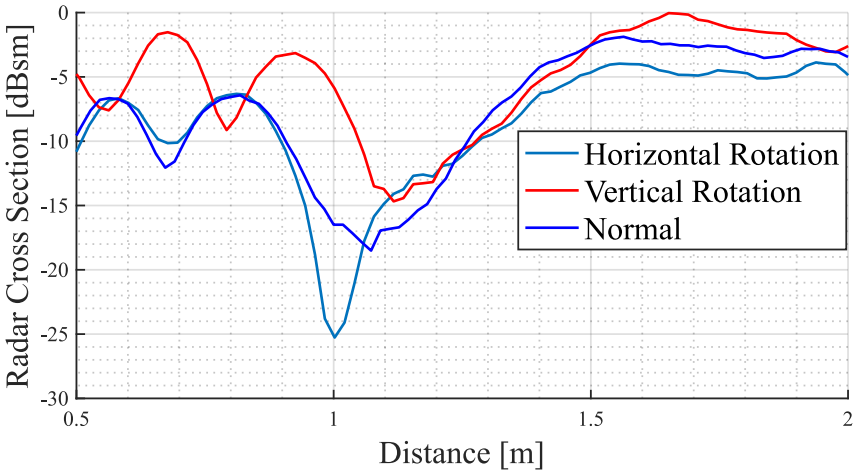

(b) RCS

Figure 4.8: Received power and RCS while rotating the 3D young male subject around an horizontal axis and a vertical axis.

4.1.6 Tests regarding the operating frequency

Another study was conducted using the same 3D subject, focusing on the operating frequency of the Bio-Radar system. Despite the radar system's operating frequency being 5.8 GHz, it was considered relevant to assess the impact of frequency on the behaviour of the received signal and, consequently, on the occurrence of LMs.

In this study, three approaches were employed. In the first approach, the frequency was varied across different ISM bands. In the second approach, the frequency was adjusted within the same ISM band. Lastly, in the third approach, the frequency range was extended from 5.6 GHz to 6 GHz.

In the first approach, the frequency was changed from 5.8 GHz to 2.5 GHz and 24 GHz. These frequencies were selected because they do not require exclusive access and are available for nearly anyone to use. The received power and RCS obtained from the simulation are presented in Figure 4.9. Upon analyzing the results, it is evident that as the frequency increases significantly, the number of LMs also increases. Furthermore, as the frequency increases, the received power decreases in terms of average power.

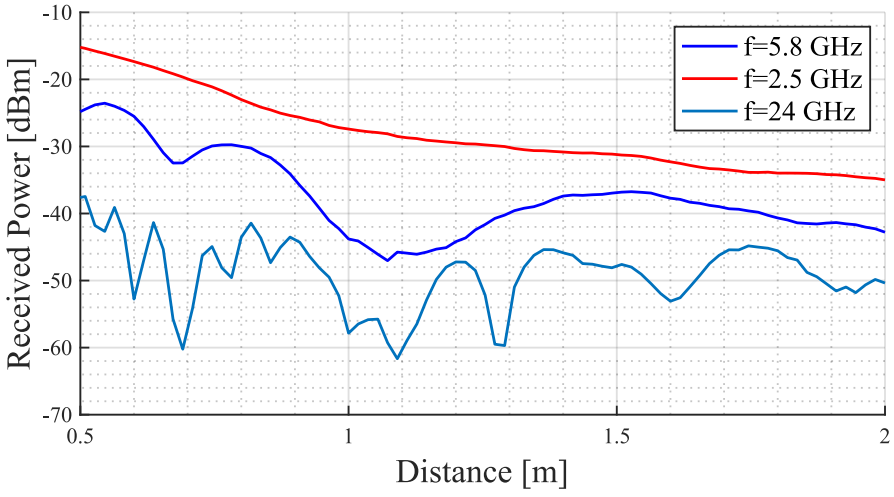

(a) Received Power

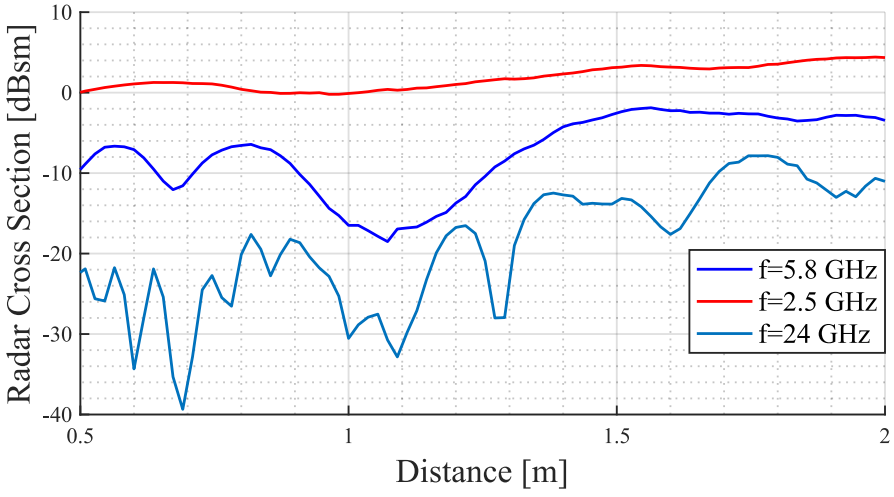

(b) RCS

Figure 4.9: Received Power and RCS variation according to the distance - Different ISM band.

To further investigate whether this phenomenon also occurs within the same ISM

band, the same test was conducted, marking the second approach of this study. The frequency was varied from 5.8 GHz to a narrower range, specifically 5.725 GHz and 5.875 GHz. The results are presented in Figure 4.10.

It can be observed that, although the behaviour throughout the distance stays similar in the three frequencies, from 1 to 1.2m it is noticeable a significant variance in the position of the LM. The 5.8 GHz frequency, of the three analysed in the same ISM band, seems to be the most suitable since it causes the least pronounced LM.

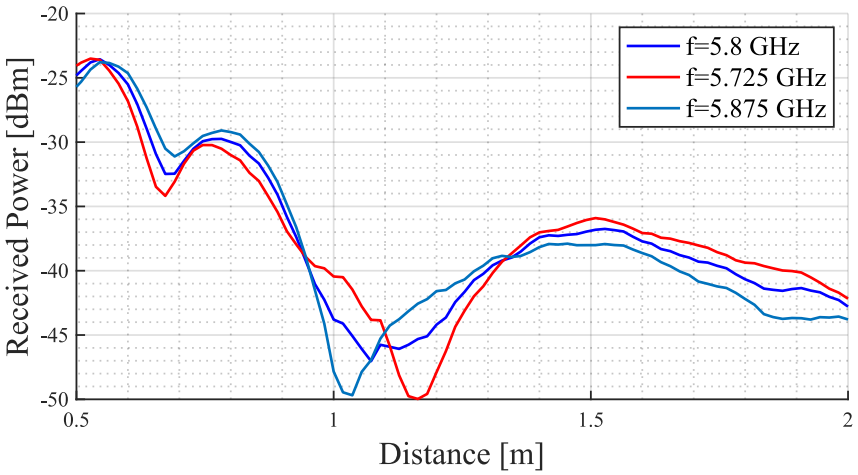

(a) Received Power

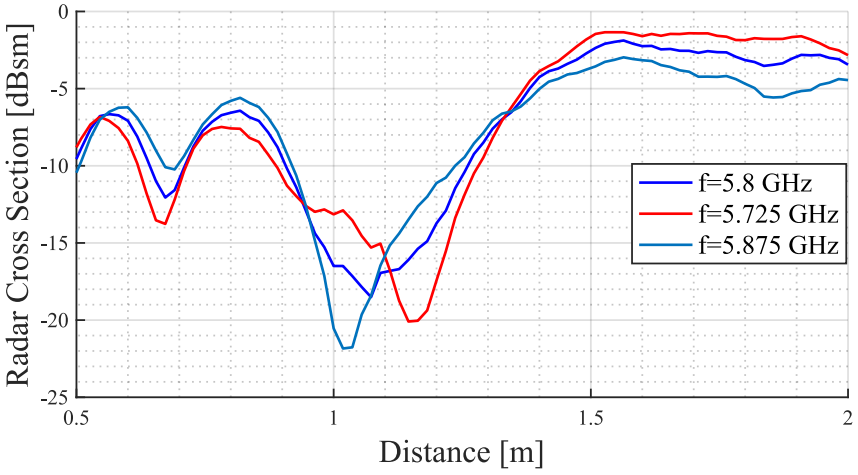

(b) RCS

Figure 4.10: Received Power and RCS variation according to the distance - Same ISM band.

Finally, the third approach involved varying the frequency from 5.6 GHz up to 6 GHz. The objective was to determine if there is an optimal frequency for conducting simulations, one that results in fewer LMs. Once again, received power and RCS data were collected while varying the distance for each frequency. The results are presented in Figure 4.11.

As the frequency increases, the occurrence of the last LM happens earlier. It is also noticeable that frequencies 5.6 GHz and 6 GHz exhibit very pronounced LMs, on the order of -65 dBm. Overall, the 5.8 GHz frequency appears to be a suitable choice for the Bio-Radar system in general because, out of the five frequencies analyzed, it produces the least pronounced LMs.

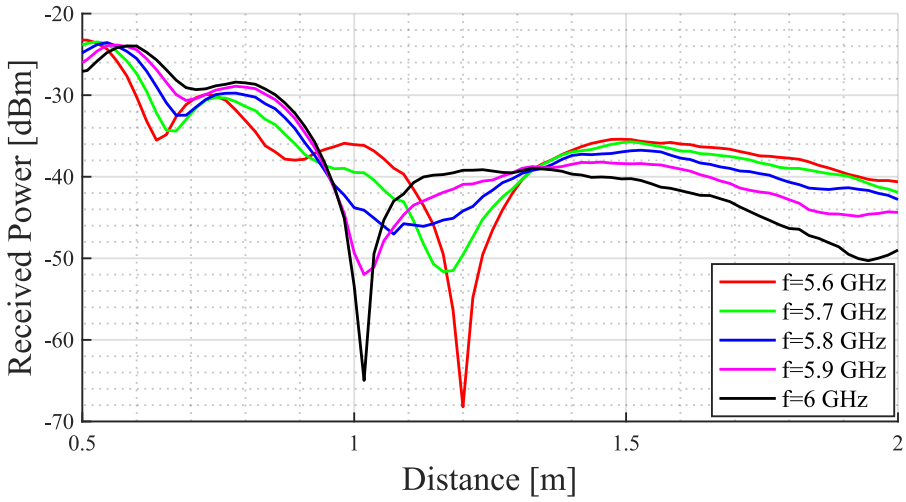

(a) Received Power

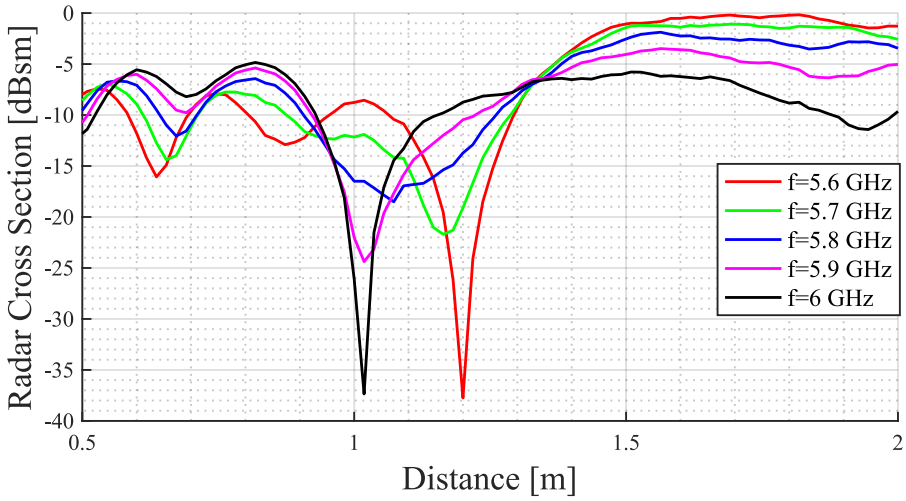

(b) RCS

Figure 4.11: Received Power and RCS variation according to the distance - Range from 5.6 GHz up until 6 GHz.

4.1.7 Variation of the width of the subject's torso

The final series of tests conducted with this subject involved altering the width of the subject's torso to observe whether the subject's physical characteristics significantly impact the behaviour of LMs. The width was adjusted within a range of 0.23 m to 0.32

m, while the original width of the subject was 0.3 m. The received power and RCS obtained are presented in Figure 4.12.

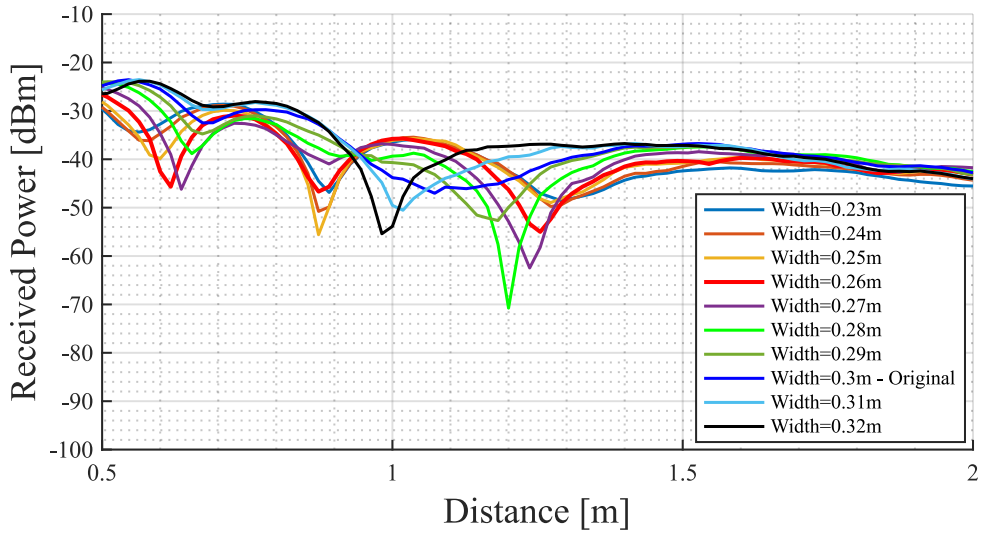

(a) Received Power

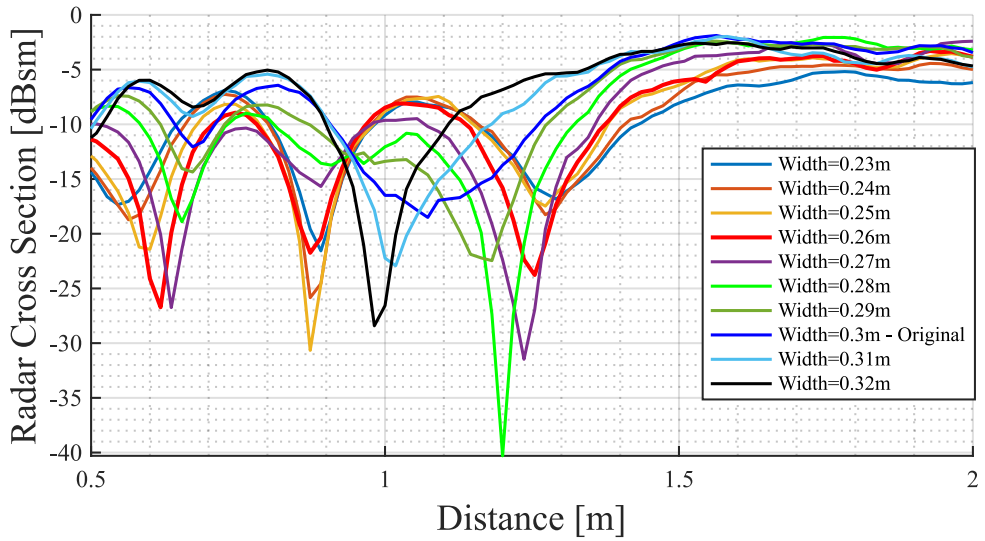

(b) RCS

Figure 4.12: Received Power and RCS variation according to the distance - Variation of the width of the chest-wall young male.

Overall, the signal behaviour exhibits significant variations and is highly sensitive. For every 0.01 m difference in width, various shifts can be observed. Some LMs become more pronounced, and even the appearance of more LMs becomes more noticeable when compared to the original signal, which only had one slightly pronounced LM. Therefore, even the slightest change in the subject's body can result in a substantially different profile, affecting not only the received power but also the RCS.

4.2 Comparison of three 3D subjects

In this section, the goal was to compare the impact of different body shapes on received power and RCS. To achieve this objective, three simulations were conducted, each involving a distinct 3D CAD subject. One of the targets was the young male previously used in the simulations in Section 4.1. The other two subjects were a female with a height of 1.53 m and a middle-aged male with a height of 1.82 m. All three subjects can be seen in Figure 4.13. The antennas in all three subjects were aligned with the diaphragm. It is worth mentioning that auxiliary simulations regarding the young male and female subjects were performed and are presented in Appendix A.

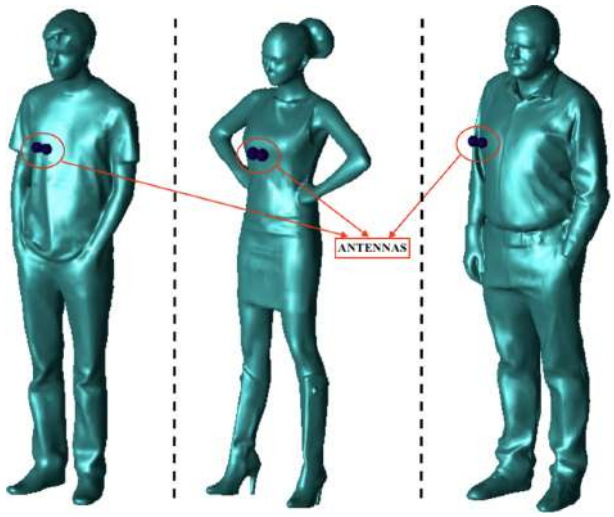

Figure 4.13: Three CAD subjects.

Once again, the received power and RCS were assessed while varying the distance between the different subjects and the antennas, with a considered range of 0.5 to 2 m. The comparison between the three subjects is presented in Figure 4.14.

The received power and RCS exhibit wide variations within a 2 m range for all 3D subjects. The middle-aged male subject presents more LMs than the other two subjects and has a shift in minima compared to the young male subject. On the other hand, the female subject displays more pronounced LMs compared to the other subjects at 0.6 m and 0.9 m. One plausible explanation for this could be due to the physical shape of the subjects. Considering that male subjects might have a flatter surface, resembling a rectangular or square shape, they could cause less pronounced LMs in comparison to the female subject. Given the wide variations in received power and RCS within a 2 m range, a more in-depth study is required to determine whether there is an optimal operating distance for each subject, as the behaviour of these simulations for each subject

diverges significantly.

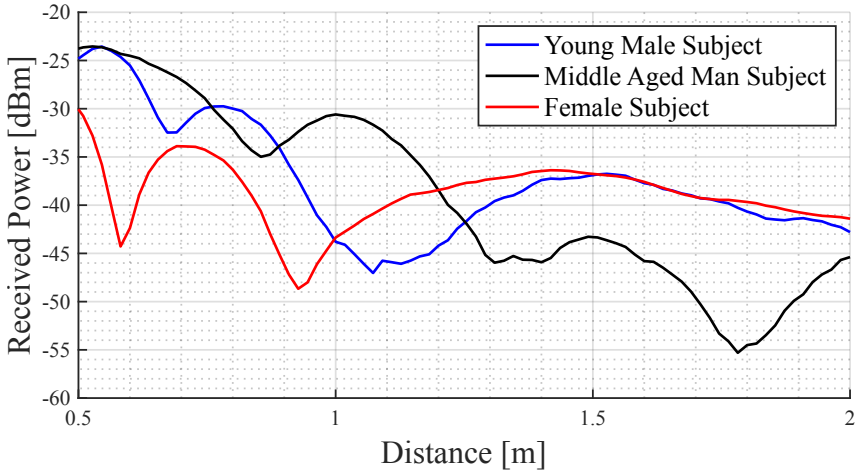

(a) Received Power

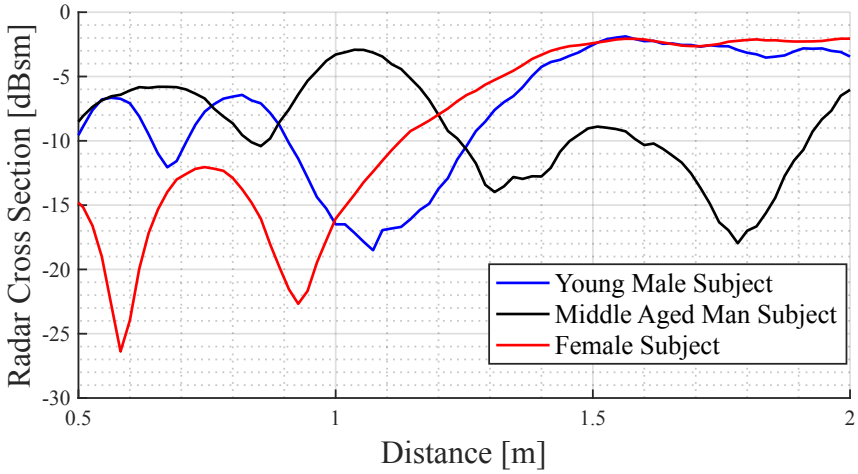

(b) RCS

Figure 4.14: Received power and RCS within the range of 0.5 to 2m of all 3D model subjects.

4.3 Discussion of the simulated results

In this section, it was provided a brief summary of the key findings from this chapter. Firstly, the simulation software was confirmed to align with the far-field criterion. Specifically, for the young male subject, the simulation indicated that the far-field region begins at the same distance as predicted by the theoretical equation. Additionally, this simulation suggests that the Bio-Radar system is likely operating in the near-field region from the target's point of view due to the target's dimensions.

Furthermore, in future practical experiments, it is possible to increase the transmitted power without impacting the behaviour of the received signal. The only observed

effect was that increasing the transmitted power led to a linear increase in received power, while it did not affect the RCS. This is because the RCS is independent of the transmitted power.

Depending on the subject's height and structure, the legs can impact the received signal from a certain distance forward. This demonstrates that each part of the human body has a distinct effect on received power and RCS.

Another crucial observation is the significance of maintaining a stable posture and minimising movement, as even slight variances can alter the received signal, potentially shifting the LM. Furthermore, different subjects with varying shapes and sizes exhibit significant variations in received power and RCS within a 2 m range. For this reason, the next step is to go to the anechoic chamber and conduct experiments with different subjects to observe whether there is an optimal operating distance range applicable to all subjects or if each case is unique. Determining a suitable operating distance may require individual analysis for each subject.

5

Human respiratory and RCS measurements in the anechoic chamber

The next approach taken in this dissertation was to perform practical measurements in the anechoic chamber with subjects. In Chapter 3, experiments with well-known shapes were conducted to validate the practical measurement process.

In this chapter, experiments were performed with a mannequin as well as with three human subjects. The goal was to observe if there is an optimal range of distances for measuring the respiratory signal, as well as the received power and RCS of the subject. Additionally, the aim was to determine if there is a specific area to avoid for measurements.

5.1 Analysis of the received power and RCS in a mannequin

The first set of practical tests involved studying the received power and the RCS at different distances when the target in question was a mannequin. This study was considered important to conduct because, unlike a human subject, a mannequin is a stationary object that doesn't exhibit slight movements. Therefore, it serves as a useful transitional object between well-known shapes and human subjects for conducting these analysis. The mannequin used had a height of 1.86 m and is shown in Figure

5.1. Both the torso and arms of the mannequin were covered with reflective fabric to enhance reflections. It is worth noting that, similar to the practical experiment with the circular plate target, the mannequin was placed on a platform with wheels, which stopped at different distances to measure the S_{21} parameter.

Figure 5.1: Mannequin used in the first set of practical experiments.

Similar to the previous experiment with the circular plate target in Chapter 4, the S_{21} parameter was obtained for each stopping distance over a period of 20 seconds to provide a more accurate representation of this parameter. For the analysis of received power and RCS, both the mean value and standard deviation of these measurements were calculated. The obtained results are presented in Figure 5.2. It is worth noting that a preliminary analysis regarding the mannequin was performed and is presented on appendix B, where the a single measurement S_{21} parameter was obtained for each distance.

The received power tends to decrease with distance, while the RCS increases with distance, exhibiting a somewhat oscillatory behaviour. With this target, the most pronounced LM is located at 1.74 m when considering the RCS parameter. When observing the standard deviation, there is greater dispersion around 1.74 m compared to the other distances. This could indicate that, for this particular subject, a stationary object such as a mannequin, 1.74 m may not be the most suitable distance for performing measurements, as there is significant variability in the values, even in a controlled environment such as the anechoic chamber.

Compared to the previous 3D CAD subjects, particularly the middle-aged man subject, the behaviour of the received power and RCS is not exactly the same. However, the most pronounced LM is located around the same distance. This is likely related to the

fact that both subjects have a similar stature and height. The middle-aged man subject, unlike the young male and female subjects, does not exhibit a tendency towards a constant value from 1.5 m forward, similar to the mannequin in this analysis.

Although the subjects are not exactly the same, two important aspects observed in this analysis are the following: subjects with similar structures exhibit LM around the same range of distances, and with subjects with bigger height and structure, the distance of the most pronounced LM is closer to 2 m when compared to subjects with smaller or average height and structure.

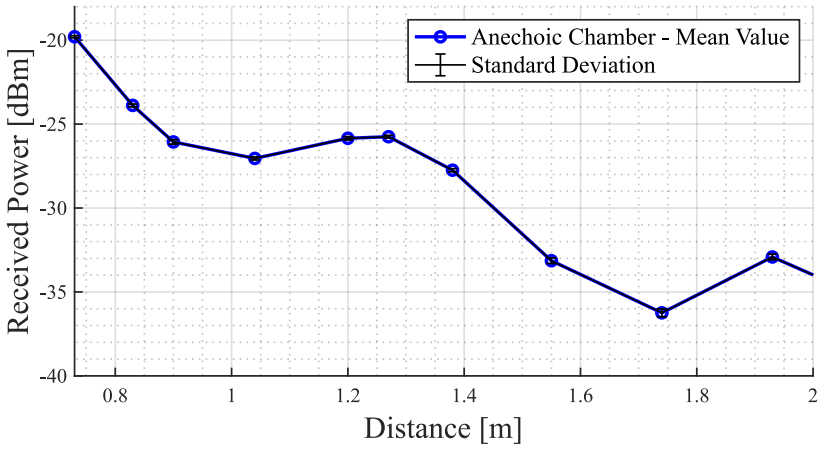

(a) Received Power

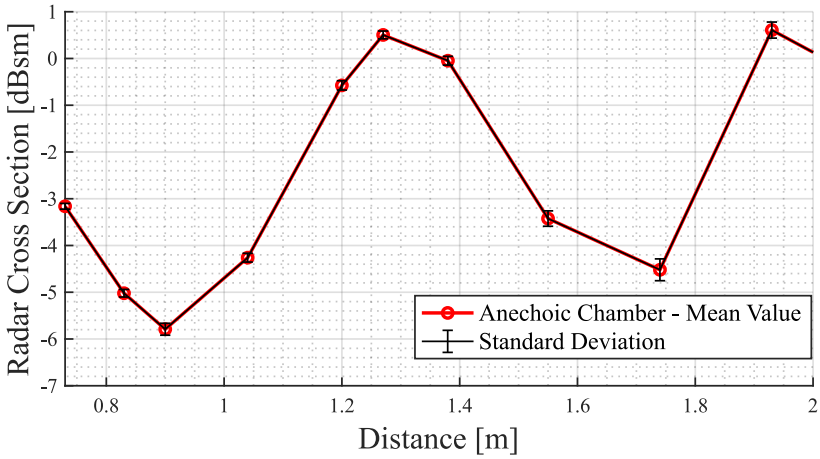

(b) RCS

Figure 5.2: Received power and RCS variation according to the distance for the mannequin.

5.2 Analysis of the respiratory signal in various subjects

After the experimental measurements with the mannequin, the next step was to perform a similar study, but now with human subjects. The study was approved by

the Ethics and Deontology Committee of the University of Aveiro, Portugal (No.10-CED/2023). The implemented procedure was in line with the Declaration of Helsinki, and an informed consent was obtained from all the participants.

Up until this point, only the received power and the RCS have been analysed in the various tests performed. This is because the tests were conducted using well-known shapes, 3D CAD subjects, and a mannequin, all of which do not exhibit a respiratory signal. However, the study of the LM was important as it allowed to gain a better understanding of the range of distances at which LM typically occur. Supposedly, if the respiratory signal is analysed at the same distance as a LM observed in the received power, the respiratory signal at that particular distance may not be as strong as when the received power reaches a maximum.

In this section, a study was conducted on the respiratory signal at various distances using different subjects. The goal was to observe whether there are suitable ranges for measuring the respiratory signal for different subjects. To perform the analysis of the respiratory signal in the anechoic chamber, the S_{21} parameter was measured with a VNA for 20 seconds at each distance, providing a more accurate value. This measurement was taken with the subject standing in front of the radar in each position.

Simultaneously with the VNA measurements, the respiratory signal was recorded using a system called Biopac. The Biopac system is connected to an acquisition board equipped with several modules for different types of signal acquisition, including ECG (Electrocardiogram), breathing, and blood pressure. The RSP100C module consists of a respiration transducer chest band placed around the chest cavity of the subject being tested. This transducer measures respiratory effort by analyzing the instantaneous thoracic perimeter, [31]. The obtained signal has a mean value, which is dependent on the chest cavity structure of each subject, resulting in variance around this value, [2].

For all the tests conducted in this section, the subjects were positioned in front of the antennas for 20 seconds at each distance. They were instructed to remain as still as possible during the measuring process. To identify and synchronise the respiratory signal obtained from the Bio-Radar with the signal obtained from the BioPac, an initial respiratory pattern was executed. This respiratory pattern comprised three deep breaths followed by 5 seconds of apnea, after which the subject resumed normal breathing for approximately 10 seconds.

The practical experiments were performed on three subjects, one male and two female. A brief description of each subject is presented in Table 5.1. For the signal obtained, the S_{21} parameter was processed in order to obtain the respiratory signal. The signal obtained from the VNA is a complex signal and what is being measured is the phase

variation of the received signal in the radar. In order to analyse the phase variation it is necessary to calculate the angle, which is achieved by using the *angle* function in MATLAB. In order to validate the respiratory signal obtained from the VNA, this signal was compared to the one obtained from the BioPac system by using the MATLAB plot *yyaxis*, which creates a chart with two y-axes. This analyses was performed for each subject.

Table 5.1: Subjects that performed the practical measurements.

	Description
Subject 1	Male Subject, Height = 1.87 m, IMC = 30 kg/m^2
Subject 2	Female Subject, Height = 1.50 m, IMC = 18.7 kg/m^2
Subject 3	Female Subject, Height =1.58 m, IMC = 25 kg/m^2

5.2.1 Practical tests with Subject 1 standing up

The first test was performed with Subject 1 while the subject was standing up. The setup used is illustrated in Figure 5.3.

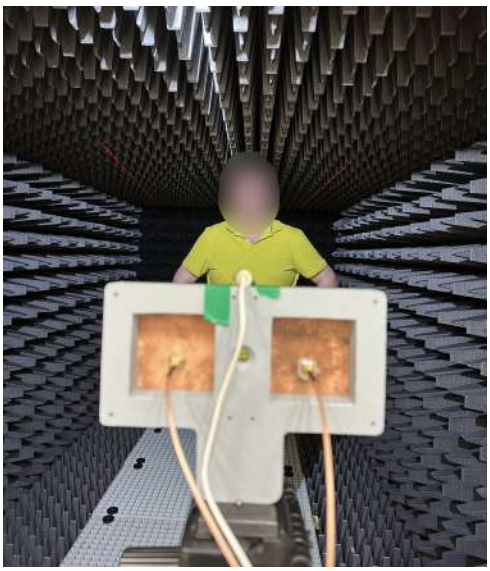

Figure 5.3: Setup used with Subject 1 while the subject was standing up.

The respiratory signal was analysed using both the VNA and BioPac for each distance. The results are presented in Figure 5.4, where a few significant distances were selected for analysis. The blue line represents the respiratory signal obtained from the VNA, while the orange line represents the respiratory signal obtained with the BioPac.

Although it was possible to align the first three deep breaths acquired from the VNA with those acquired from the BioPac at a distance of 0.52 m, the same cannot be applied at further distances. In subsequent distances, it becomes very challenging to observe both the apnea and the normal breathing of the subject afterwards. Only at 0.52 m, the closest distance to the antennas, was it possible to align these initial breaths. For all other distances, distinguishing the respiratory signal was difficult due to the subject's involuntary movements. As a result, tests involving human subjects had to be conducted with the subjects seated in order to extract the respiratory signal using the VNA.

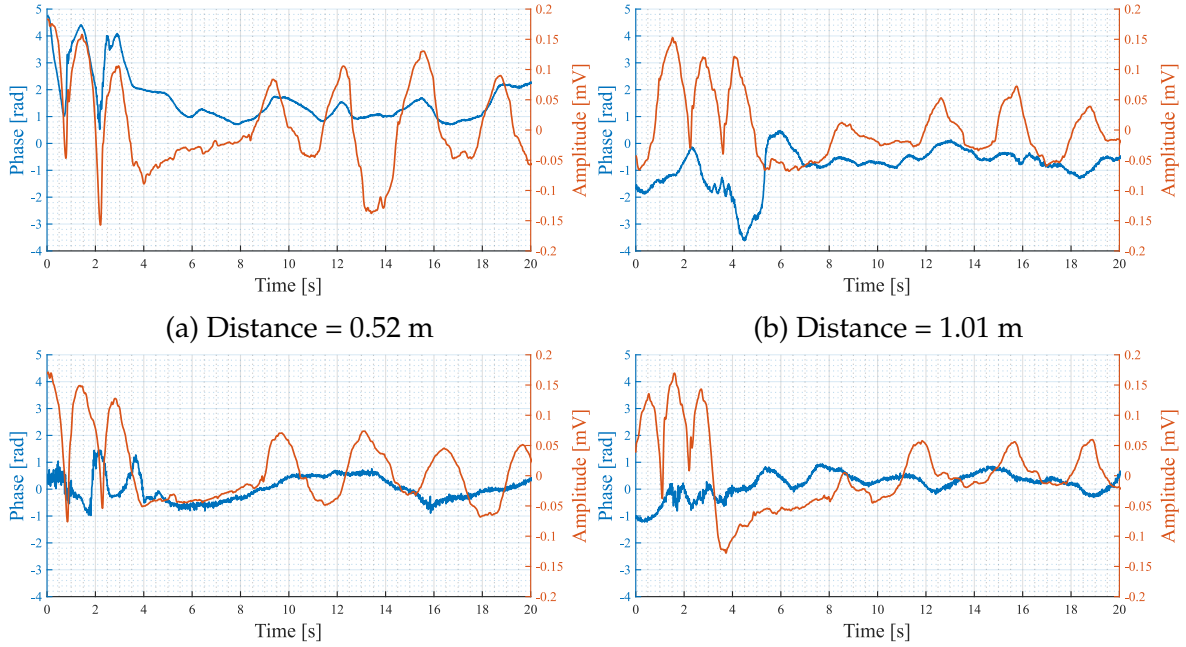

(a) Distance = 0.52 m

(b) Distance = 1.01 m

(c) Distance = 1.61 m

(d) Distance = 2.14 m

Figure 5.4: Respiratory signal obtained with the VNA and the BioPac for Subject 1 while standing up.

5.2.2 Validation of the transmitted power (P_t)

To proceed with the tests with the subjects sitting down, several preliminary measures were taken to ensure a good respiratory signal. In the previous test, where Subject 1 was standing up, it was observed that at 2 m, the respiratory signal obtained from the Bio-Radar was slightly faded. For the subsequent tests, it was considered important to increase the transmitted power (P_t) to better observe the respiratory signal at greater distances. The P_t was increased from 7 dBm to 13 dBm. Figure 5.5 illustrates the respiratory signal from the VNA compared to the signal from the BioPac at both 7 dBm and 13 dBm P_t. These measurements were taken while Subject 1 was seated at a

distance of 2 m.

By increasing the P_t, the initial breathing pattern from the Bio-Radar became significantly more pronounced. As a result, all practical measurements conducted from this point onward were performed with 13 dBm of P_t to compensate for the attenuation with distance.

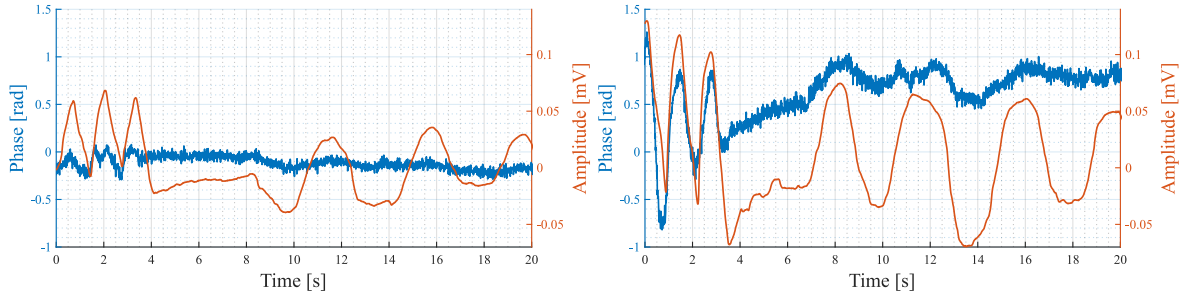

(a) P_t = 7 dBm (b) P_t = 13 dBm

Figure 5.5: Respiratory signal obtained with the VNA and the BioPac for Subject 1, while varying the P_t.

5.2.3 Practical tests with all subjects sitting down

In this section, a procedure similar to that in section 5.2.1 was carried out, but in this set of tests, all three subjects were seated. The practical measurements in this section were conducted on all three subjects, with the antennas of the Bio-Radar positioned in front of each subject. The setup described is illustrated in Figure 5.6, where Figure 5.6a represents Subject 1 and Figure 5.6b represents Subject 2.

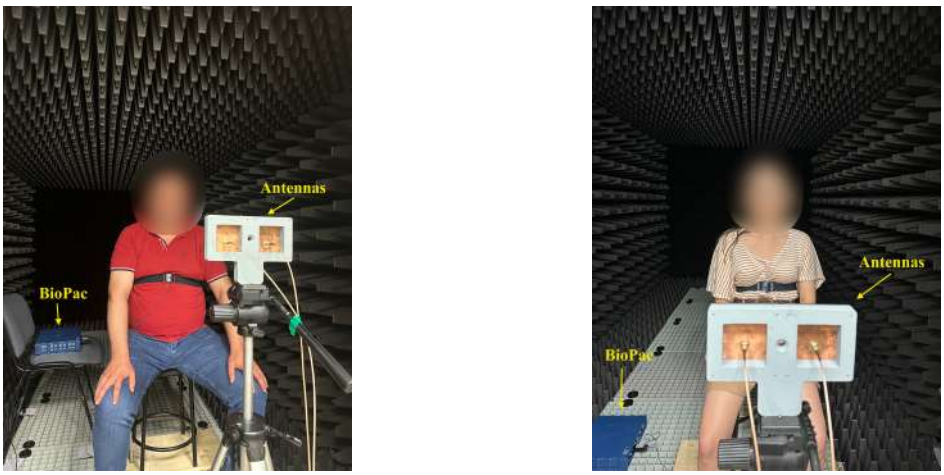

(a) Subject 1 (b) Subject 2

Figure 5.6: Practical measurements with the subjects sitting down.

Comparison between the respiratory signal obtained from the VNA and BioPac

For all three subjects, once again, the respiratory signal obtained from the VNA was compared to the one obtained from the BioPac. For each subject, a few critical distances were selected to be shown in this dissertation. The results obtained for Subject 1 are presented in Figure 5.7, where the blue line represents the signal from the VNA, and the orange line represents the signal from the BioPac.

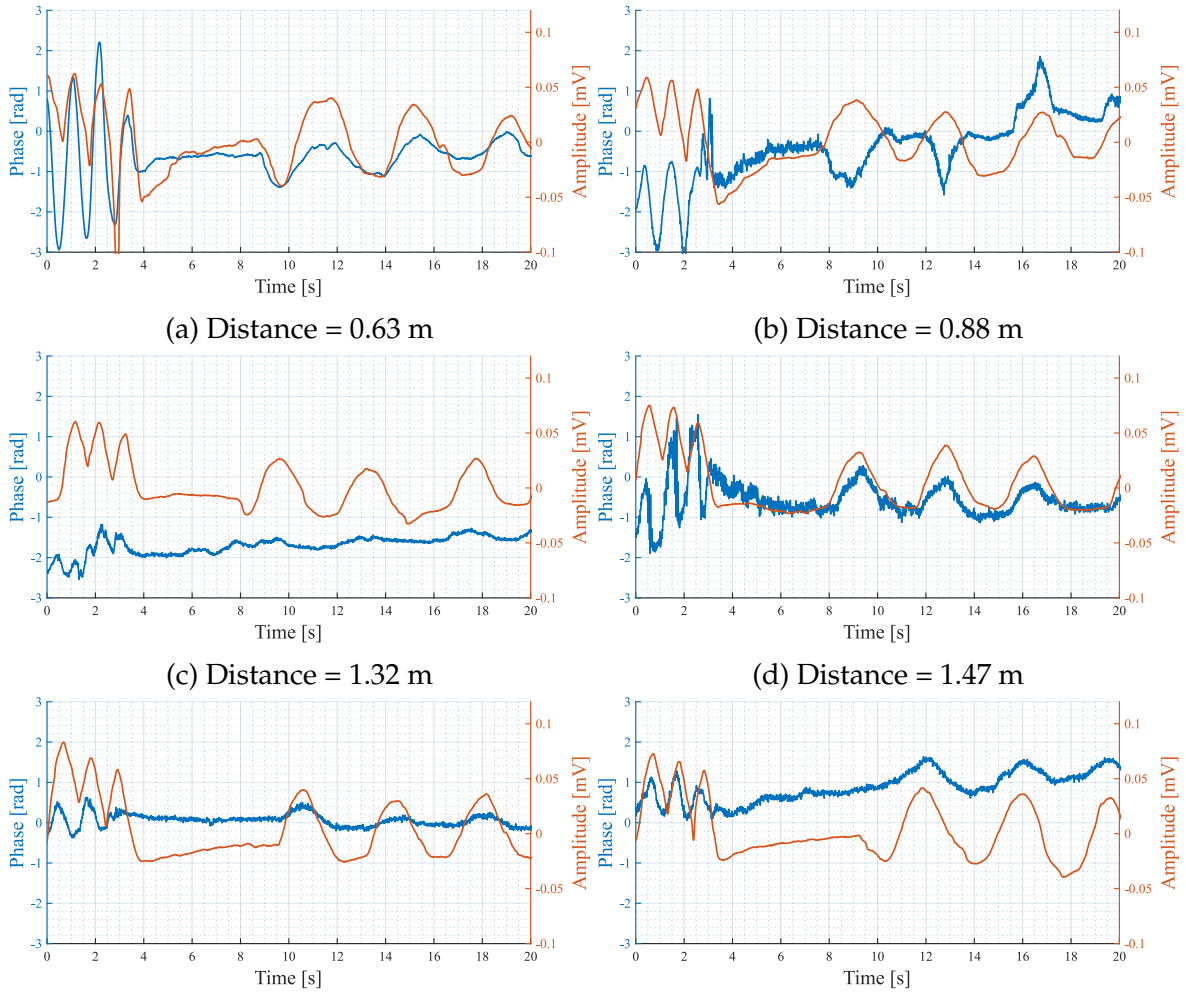

(a) Distance = 0.63 m

(b) Distance = 0.88 m

(c) Distance = 1.32 m

(d) Distance = 1.47 m

(e) Distance = 1.71 m

(f) Distance = 1.91 m

Figure 5.7: Respiratory signal obtained with the VNA and the BioPac for Subject 1 while sitting down.

In comparison with the previous results, where Subject 1 was standing, the respiratory signal obtained from the Bio-Radar can be observed more clearly when the subject is sitting down. The initial breathing pattern is more pronounced, as is the normal breathing. At distances of 0.63 m, 0.88 m, and 1.47 m, both the initial breathing pattern and normal breathing of the subject closely match the signal obtained from the BioPac. However, at 0.88 m, the normal breathing of the subject appeared abnormal compared

to the BioPac. This could be due to slight movements or the subject's posture at this specific distance. It is also noteworthy that at certain distances, particularly at 1.32 m and 1.71 m, while the initial breathing pattern is present, the normal breathing of the subject is very faint. Additionally, as the distance increases, the signal noise tends to be higher, especially from 1.47 m onward, with the exception of 0.88 m. In general, with this subject, it seems that at two specific distances (1.32 m and 1.71 m), the signal appears fainter, gradually increasing in the following distances.

The same analyses was performed but now regarding Subject 2. The obtained results are presented in Figure 5.8.

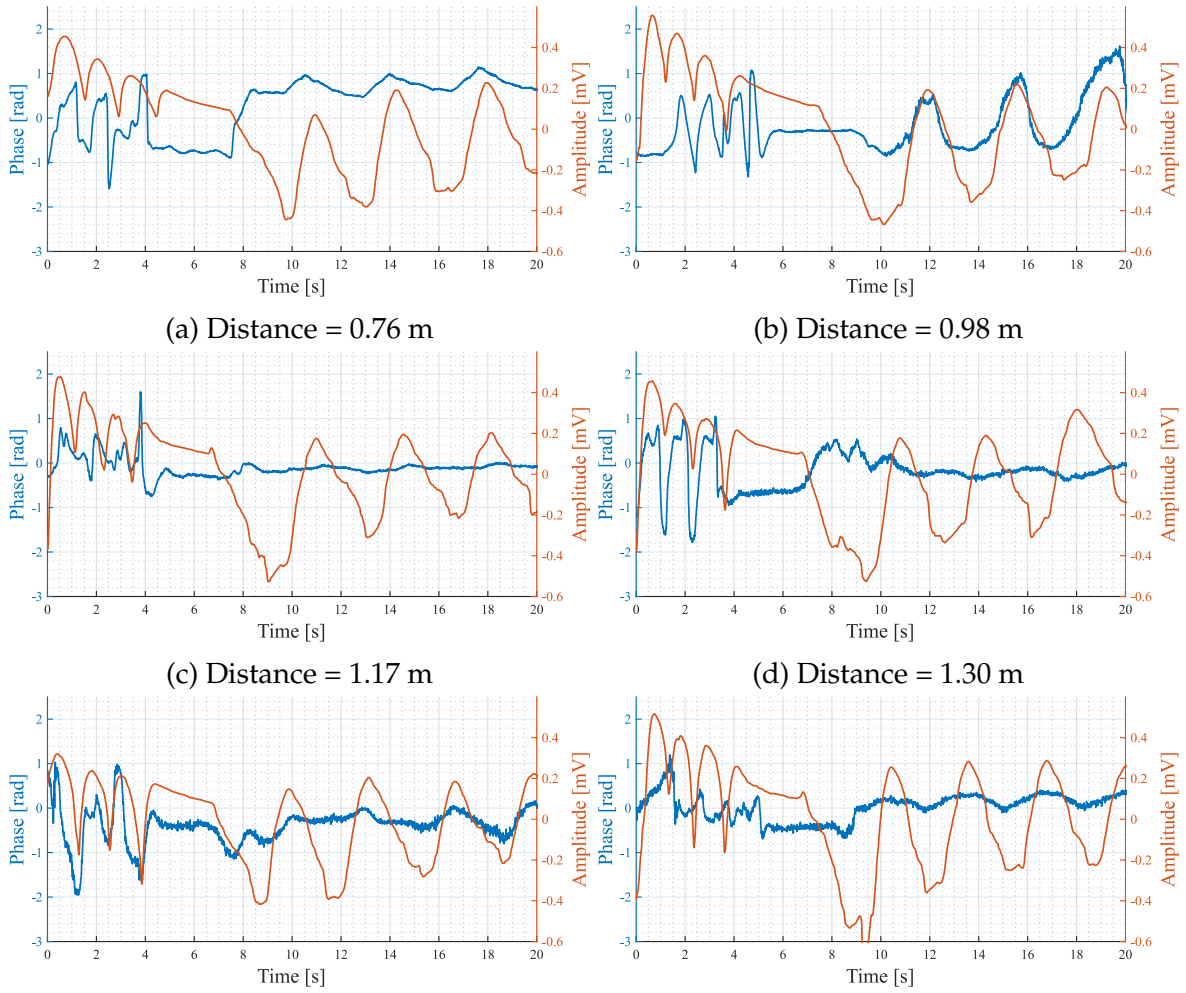

(a) Distance = 0.76 m

(b) Distance = 0.98 m

(c) Distance = 1.17 m

(d) Distance = 1.30 m

(e) Distance = 1.67 m

(f) Distance = 1.93 m

Figure 5.8: Respiratory signal obtained with the VNA and the BioPac for Subject 2 while sitting down.

The initial breathing pattern can be observed at every distance, as well as the normal breathing of the subject, although it may appear faint at times. The best distance to observe this signal is at 0.98 m. On the other hand, at 1.17 m, the normal breathing of the

subject appears to be nonexistent, despite the subject breathing normally, suggesting the presence of a LM. Additionally, as with the previous subject, at higher distances, the SNR decays.

The same approach was one last time performed, but this time on Subject 3, which is also a female subject with a little superior height and IMC when compared to Subject 2. The results are in Figure 5.9, where six significant distances were chosen. For this particular subject, in almost every distance the initial breathing pattern as well as the normal breathing of the subject are very pronounced except at 1.64 m. At this particular distance, although the first three deep breaths are pronounced when compared to the remaining signal, the apnea and the normal breathing cannot be distinguished from each other. This could be indication that a LM is present at this distance. Nevertheless, this is a qualitative analyses and to perform a more accurate evaluation, it is necessary to perform a more quantitative approach.

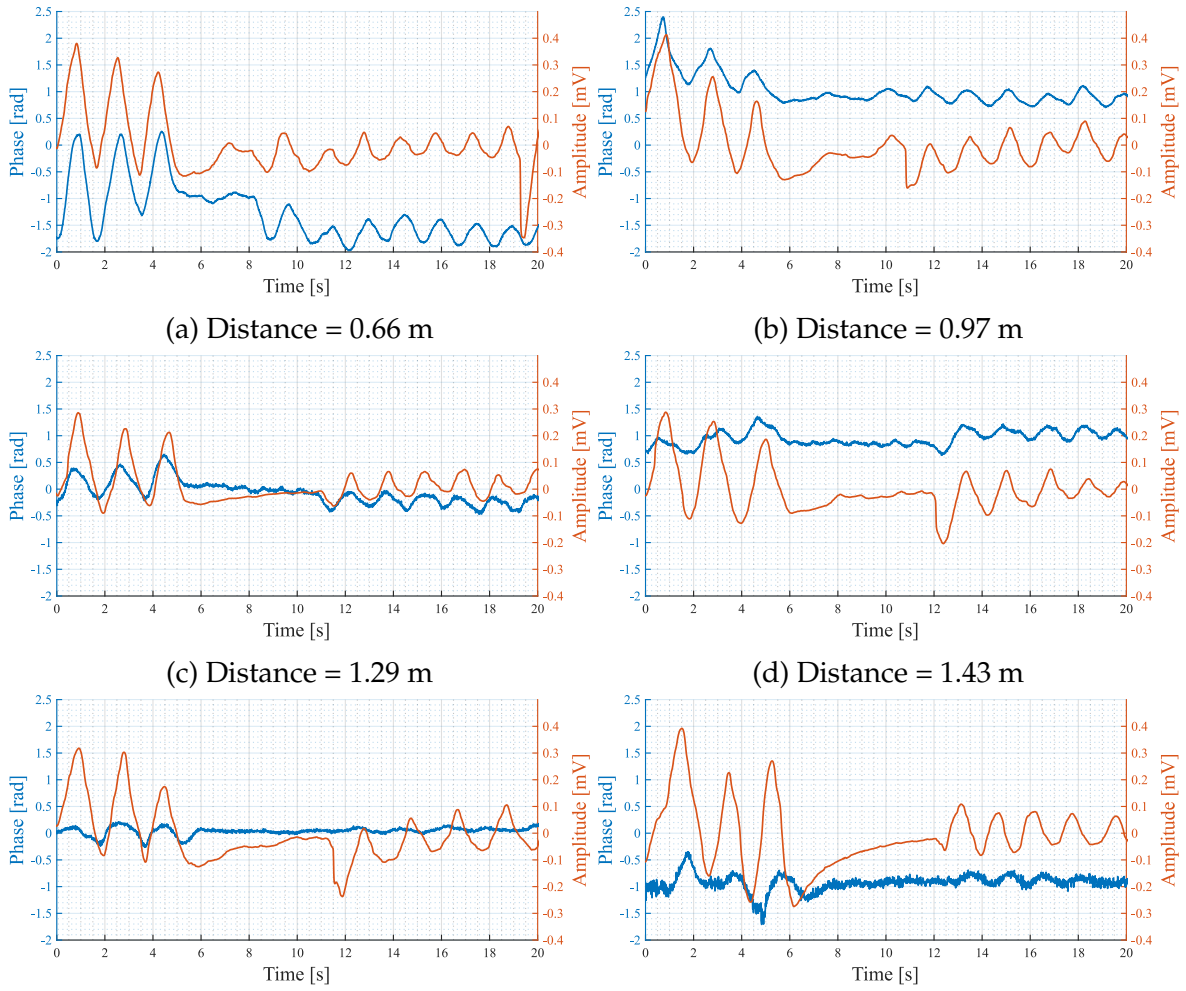

(a) Distance = 0.66 m

(b) Distance = 0.97 m

(c) Distance = 1.29 m

(d) Distance = 1.43 m

(e) Distance = 1.64 m

(f) Distance = 1.92 m

Figure 5.9: Respiratory signal obtained with the VNA and the BioPac for Subject 3 while sitting down.

Quantitative Analysis regarding the respiratory signal

To perform a more quantitative analysis, the mean of the first two peaks of the respiratory signal was calculated in the signal obtained from the VNA. This approach was applied to both the deep and the normal breathing of the subject. This method ensured consistency across all distances, accounting for variations in the number of deep breaths or the rate of breathing. The results from this analysis are presented in Figure 5.10, where the first graph (Figure 5.10a) represents the mean of the first two peaks during deep breathing, and the second graph (Figure 5.10b) represents the mean of the first two peaks during normal breathing.

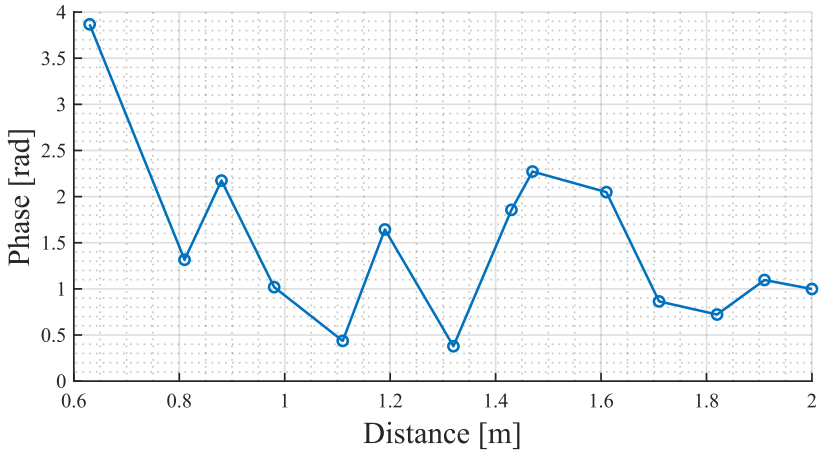

(a) Deep Breathing

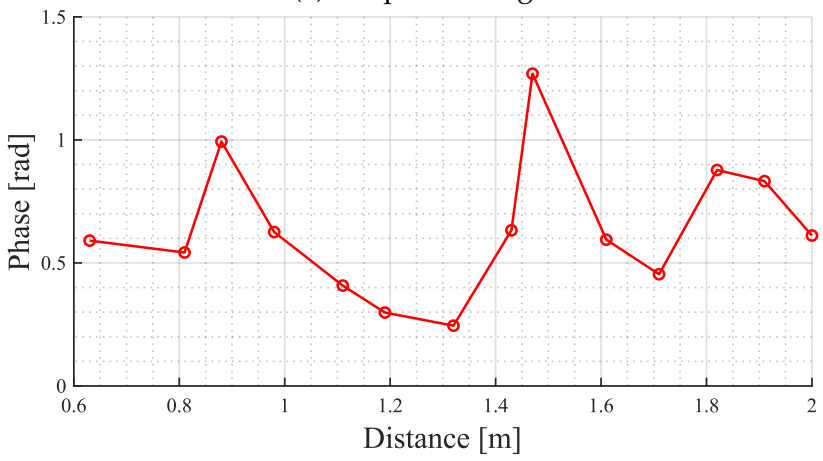

(b) Normal Breathing

Figure 5.10: Mean of the of the first two peaks for deep and normal breathing for each distance with Subject 1.

Deep breathing exhibits a wider phase range and more pronounced oscillations compared to normal breathing. This is because forced inhalation and exhalation leads to more involuntary movements than when the subject is breathing normally. Additionally, it is challenging for a human subject to replicate the exact same deep breathing

pattern since each breath is unique. Consequently, the graph of normal breathing was selected for a detailed analysis.

By observing the figure where the normal breathing of the subject is present, there are two distances that do not seem to be the best to measure the respiratory signal, which are 1.32 m and 1.71 m. This is coherent with the previous analyses performed with the graphs in Figure 5.7. Also, at 1.11 m and 1.19 m, the phase obtained was really low compared with the other distances, making them also not good distances to measure the respiratory signal. The remain distances could be good to measure this signal, especially at 0.88 m and 1.47 m. Always keeping into account that with the increasing of the distance, the SNR decay and the respiratory signal may not be as pronounced.

The same approach was now applied to Subject 2. The results for both deep breathing and normal breathing of Subject 2 are presented in Figure 5.11.

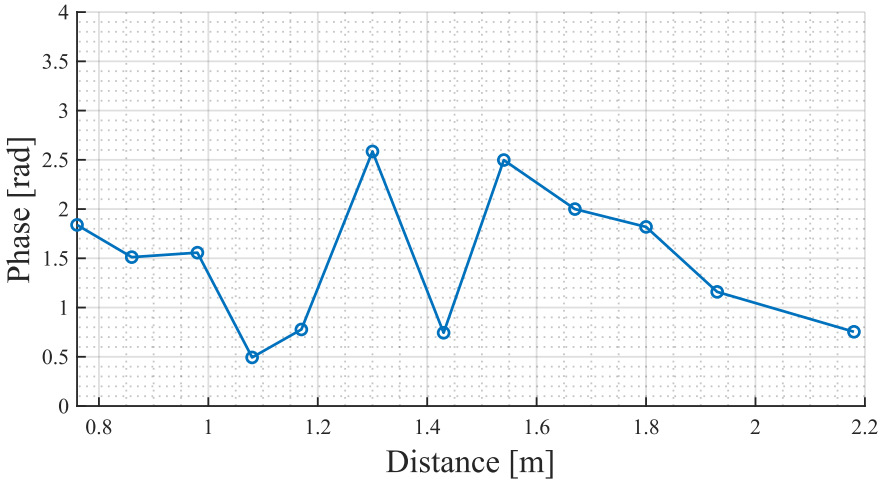

(a) Deep Breathing

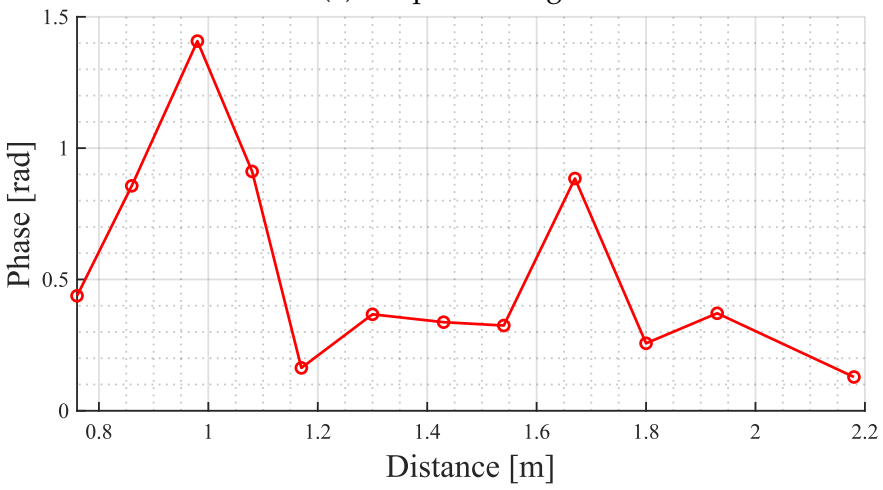

(b) Normal Breathing

Figure 5.11: Mean of the of the first two peaks for deep and normal breathing for each distance with Subject 2.

The deep breathing of the subject exhibits a more oscillatory behaviour with a larger phase variation, similar to what was observed with Subject 1. Once again, the graph depicting the normal breathing of the subject was analysed, as it is considered more stable in comparison to the graph showing the deep breathing of the subject. In Figure 5.11b, there are two distances that have a higher phase, this meaning that the respiratory signal obtained is clearly stronger. These distances are 0.98 m and 1.67 m. These was expected since the respiratory signal was very pronounced in Figure 5.8 for these values. At distances 1.17 m and 1.80 m, the respiratory signal is much weaker, making them not good distances to study this signal.

One last time, the mean of the first two peaks of the respiratory signal, for the deep breaths of the subject as well as the normal breathing of the subject, was calculated for Subject 3. The results obtained for deep breathing and normal breathing are presented in Figure 5.12.

Overall, in comparison with the other two subjects, Subject 3 exhibits a much lower phase in the respiratory signal. This may be attributed to the subject's breathing pattern, posture, or unique structural characteristics. However, it is important to note that each subject is unique and should not be directly compared. Analysing both signals, once again, the deep breathing of the subject presents a higher phase and a more oscillatory behaviour in comparison with the normal breathing of the subject.

By observing the graph in Figure 5.12b, which is the mean of the first two peaks of the normal breathing of the subject, there is a minimum of signal at 1.64 m and a maximum of signal at 1.2 m and from 1.75 m to 1.92 m. This indicates that good distances to measure the respiratory signal would be 1.2 m, 1.75 m or 1.92 m and a bad distance would be 1.64 m. However, it must be bared in mind that at higher distances, the SNR is higher, so for this subject around 1.2 m would be a good distance to measure. Also, the first distances are once again, always good to measure the respiratory signal, presenting a good level of mean phase.

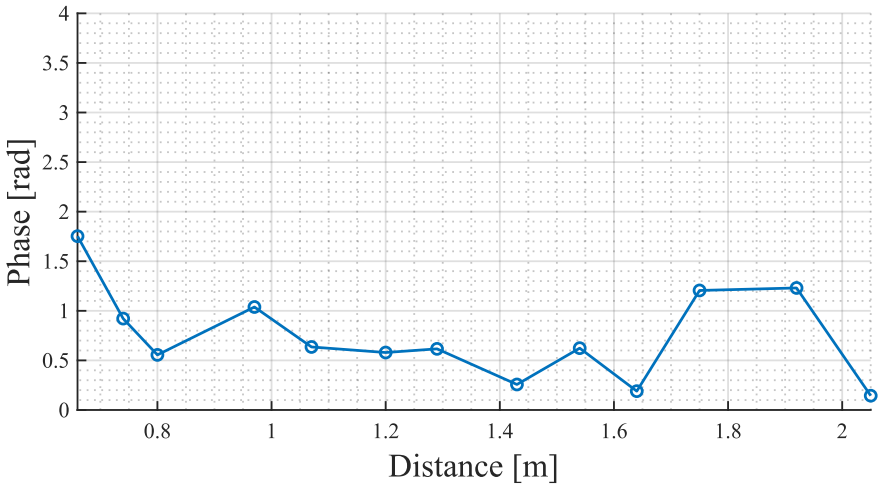

(a) Deep Breathing

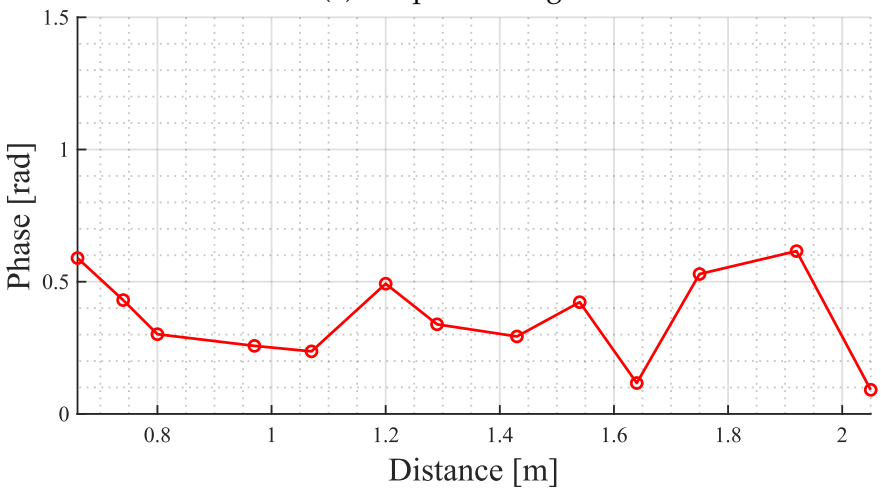

(b) Normal Breathing

Figure 5.12: Mean of the of the first two peaks for deep and normal breathing for each distance with Subject 3.

Analysis of the Received Power and RCS

Finally, the received power as well as the RCS were calculated from the S_{21} parameter for all subjects. These values were obtained using the same procedure as previously performed in the experiment with the mannequin. The procedure applied up until this point was once again used for all subjects, involving the calculation of the mean value of the received power and RCS, as well as the standard deviation for each distance. This study was firstly done on Subject 1 and the results are depicted in Figure 5.13.

Comparing the results obtained with Subject 1 to those obtained with the mannequin, the standard deviation in the results is significantly higher for all distances. This is due to the fact that involuntary movements are very frequent, and even the slightest movement can have an impact on the variance of the values. However, it is evident

that certain distances exhibit more dispersion than others, particularly between 0.8 m and 1.11 m, and from 1.71 m onward.

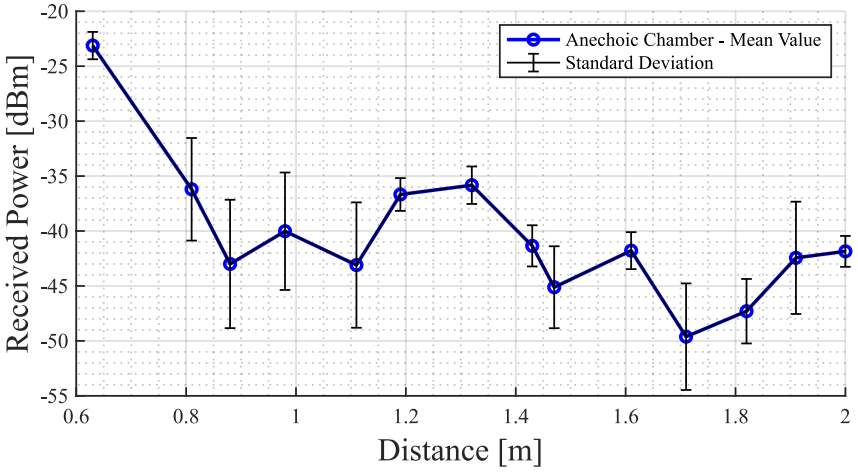

(a) Received Power

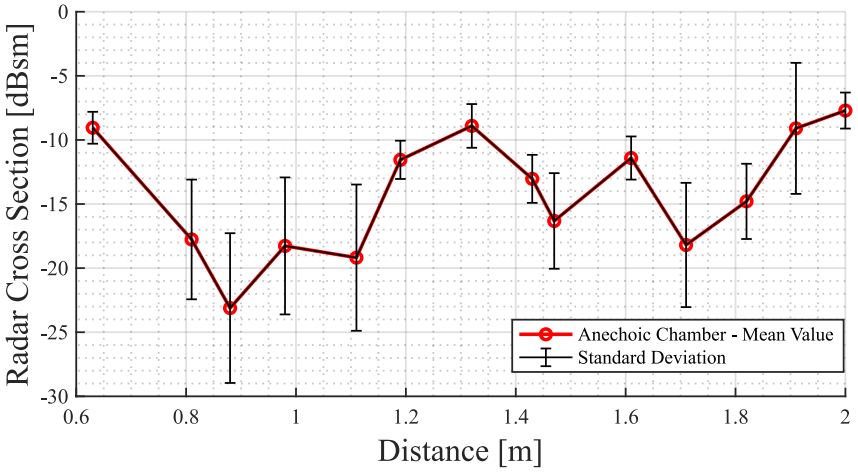

(b) Radar Cross Section

Figure 5.13: Received power and RCS according to the distance for Subject 1.

Previously in Figure 5.10b, it was observed that 0.88 m and 1.47 m could be good distances to take measurements. As for the other distances, the obtained signals all exhibit various factors, such as body movements or attenuation, which could contribute to the signals having lower power. Consequently, these distances may not be ideal for conducting measurements. The relation between the received power and the amplitude of the respiratory signal could be inconclusive, as is the case for this particular subject. This because, from the point of view of the received power and RCS, 1.19 m and 1.61 m would seem like good distances to take measurements. But, as observed previously the mean phase of the normal breathing at these distances is very low, making them distances to avoid when measuring this signal. It can also be observed that distances closer to the radar seem good to perform measurements for both the respiratory signal

and received power.

The study of the received power and RCS was now performed on Subject 2. The results are illustrated in Figure 5.14. For this subject, all the distances present some dispersion around the mean value. However, at 1.30 m and from 1.67 m until 1.93 m, the dispersion is superior in comparison with the other distances, making these not the best distances to take measurements. However, it was observed in Figure 5.11 that 1.67 m was a good distance to measure the respiratory signal.

Similar to Subject 1, the results obtained with Subject 2 prove that there is not a relation between the received power and the amplitude of the respiratory signal, as a good distance to measure the respiratory signal could not be a distance with high received power. The first distances up to 1.17 m (distances closer to the radar) and 1.67 m are good distances to measure the respiratory signal and received power.

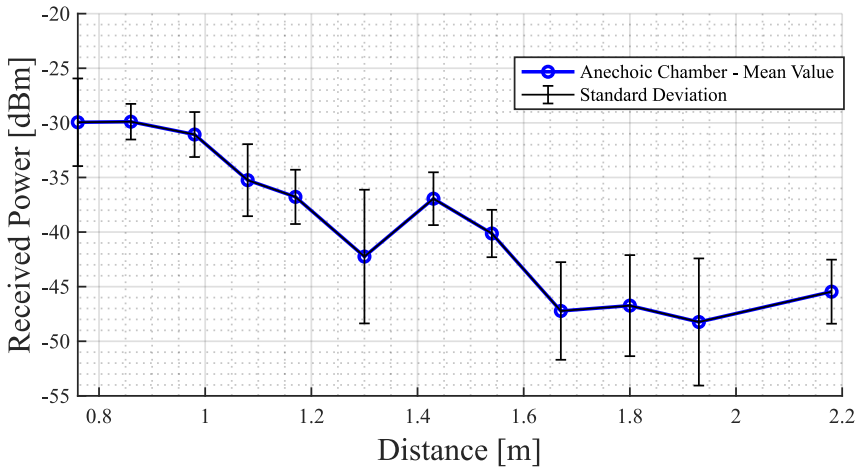

(a) Received Power

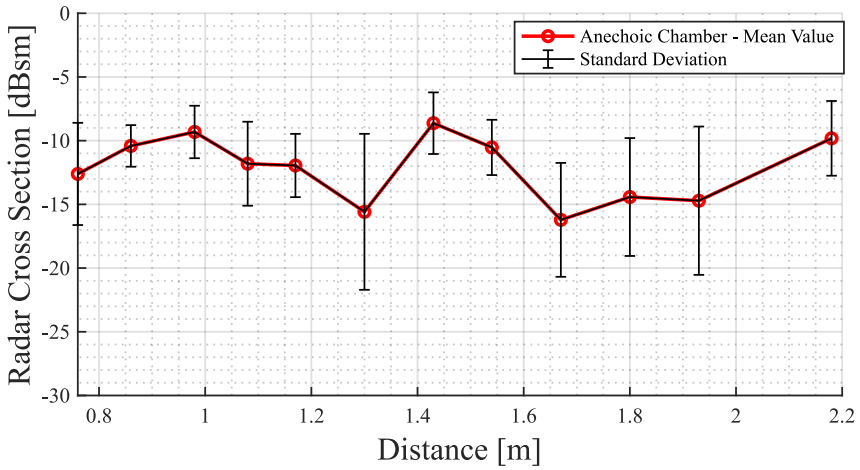

(b) Radar Cross Section

Figure 5.14: Received power and RCS according to the distance for Subject 2.

Finally, the received power and RCS were analysed for Subject 3. The results are illustrated in Figure 5.15. There is not much dispersion around the mean value for each distance for this subject, except at 1.64 m and 2.05 m, which are labeled as LM . Every other distance seems to be suitable for measuring the respiratory signal. This analysis is consistent with the previous results obtained in Figure 5.12b. Subject 3 was the only subject for which the mean of the peaks of normal breathing coincided with the results of the received power and RCS. As previously analysed, this was not the case for the other two subjects.

Overall, there is a lot of variability between subjects and many factors that can influence the analysis of the results. As future work, it could be considered performing this study with dozens of subjects to establish a trend line.

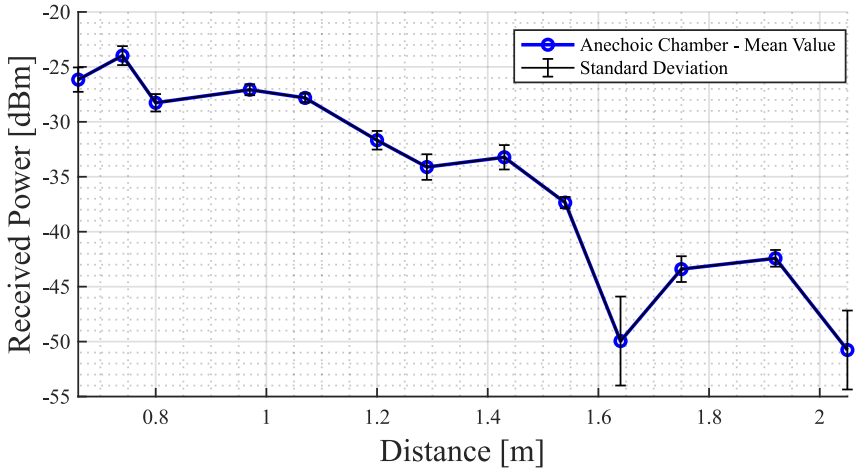

(a) Received Power

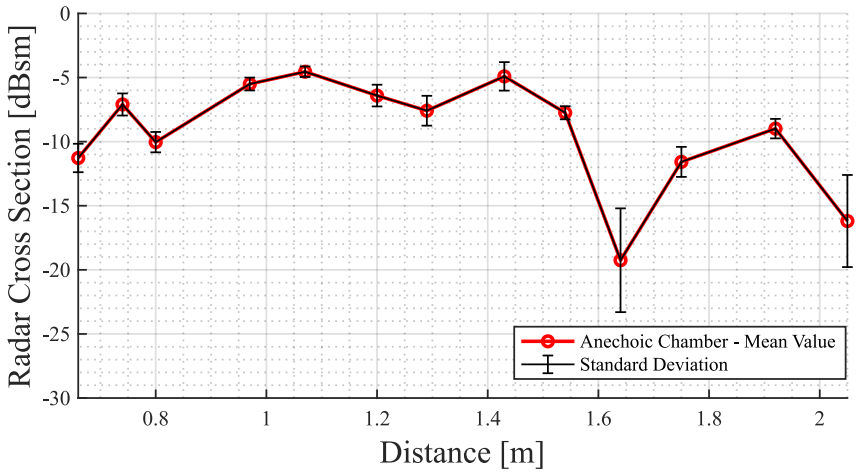

(b) Radar Cross Section

Figure 5.15: Received power and RCS according to the distance for Subject 3.

5.2.4 Results discussion for all 3 subjects

The main conclusion drawn from the experiments with the three subjects is that every case is different, even within tests on the same subject. It is challenging to define a specific distance range that is universally unsuitable for measuring the respiratory signal because various factors could influence the results.

The posture of the subjects, along with their breathing patterns, are possible factors that could influence the results. Additionally, the location of the LM observed varies from subject to subject, as some positions are more suitable than others for measuring an LM, depending on the subject. In general, shorter distances tend to be the best for performing measurements due to higher received power and a more pronounced phase of the respiratory signal. While it was not possible to definitively prove that a specific distance range, from 1 m to 1.4 m, is unsuitable for conducting measurements as it might lead to the appearance of LM, it was observed that for all three subjects, a certain distance that was not the most suitable for measuring the respiratory signal. Beyond this distance, the respiratory signal became noticeably stronger.

6

Conclusion and Future Work

Overall, the main goal of the work performed in this dissertation was to evaluate whether there exists a range of distances applicable to all subjects where measurements should be avoided due to a weak respiratory signal and lower received power. To achieve this goal, the basic principles of the Bio-Radar system were first studied. Next, a study was conducted on the received power and RCS of well-known shapes to validate both the simulation software and the practical measurement system. Subsequently, simulations were carried out with various 3D CAD subjects, and finally, experiments with human subjects were conducted in the anechoic chamber to measure the respiratory signal.

The study of received power and RCS in the context of well-known shapes proved valuable for validating both the simulation software and the practical measurement process in the anechoic chamber. Subsequently, various 3D CAD models were examined within a simulation environment. Additionally, controlled experiments were conducted to assess the impact of certain characteristics, such as gender and height, on the received signal. It became evident that the Bio-Radar system likely operates in the near-field region, considering the target's point of view, due to the target's dimensions. The simulations also highlighted the importance of maintaining a stable posture and minimising movement, as even slight variations could lead to changes in the received signal, sometimes causing a shift in the LM. When comparing the three different 3D CAD models, it became apparent that they all exhibited wide variations in received power and RCS within a 2 m range. This finding emphasised the need to treat each

subject as a unique case study during practical experiments.

Finally, the last analyses was performed in the anechoic chamber with a mannequin and three human subjects. The practical measurements performed with the mannequin were considered important because the a mannequin is a stationary object and it does not perform slight movements like a human subject. Because of this, it was a good transitioning object between well-known shapes and human subjects to perform this analysis. The study performed on the mannequin appeared to be coherent with the 3D middle aged man used in Chapter 3, since the height and structure of the subjects were similar.

In the experiments involving human subjects in a seated position, the main conclusion drawn was the uniqueness of each case. It is challenging to define a specific area universally unsuitable for measuring the respiratory signal among all subjects, as various factors, such as the subject's posture, can influence the results. However, it was observed that for all three subjects, there was a certain distance that was less suitable for measuring the respiratory signal. Beyond this distance, the respiratory signal became noticeably stronger. In general, shorter distances tend to yield better results for measuring the respiratory signal, and the suitability for measurements varies among subjects, as the appearance of LM can differ from one subject to another.

6.1 Future Work

This dissertation work was challenging, leaving room for numerous aspects that can be improved and further studied. In order to validate the simulations, practical experiments with the human subjects sitting down were performed. However, for the practical results, the setup used was the subject sitting on stool, which was standing on top of a platform with wheels.

This setup could be improved since the subject may perform some involuntary movements due to the lack of back support. To minimise these involuntary movements, an automatic shifting system could be created to enhance precision and ensure the subject's stability consistently. This would increase the likelihood of the subject moving less. Furthermore, the study conducted on the three human subjects could be extended to dozens of subjects to establish a trend line.

References

[1] *Cardiovascular diseases*, 2023. [Online]. Available: https://www.who.int/health-topics/cardiovascular-diseases#tab=tab_1.

[2] Carolina Teixeira de Sousa Gouveia, "Bio-radar: Contactless acquisition system for vital signs", Ph.D. dissertation, Universidade de Aveiro (Portugal), 2023.

[3] Alexandra Sofia Dias Lopes, "Bio-radar applications for remote vital signs monitoring", M.S. thesis, Universidade NOVA de Lisboa (Portugal), 2020.

[4] Carolina Gouveia, Daniel Malafaia, José N. Vieira, and Pedro Pinho, "Bio-radar performance evaluation for different antenna designs", *URSI Radio Science Bulletin*, vol. 2018, no. 364, pages 30–38, 2018. DOI: 10.23919/URSIRSB.2018.8486765.

[5] Mariam Abd, Ghaida Al-Suhail, Fadhil Tahir, Ahmed Ali, Hamzah Abdulkareem, Kia Dashtipour, Sajjad Shaukat Jamal, and Jawad Ahmad, "Synchronization of monostatic radar using a time-delayed chaos-based fm waveform", *Remote Sensing*, vol. 14, Apr. 2022. DOI: 10.3390/rs14091984.

[6] V. Umesh, "Classification of radars and working of ground penetration radar", *International Journal of Computational Intelligence Research*, pages 1069–1077, 2018.

[7] Habibur Rahman, *Fundamental Principles of Radar*. CRC Press, May 2019, ISBN: 9780429279478. DOI: 10.1201/9780429279478.

[8] Niraj Bhatta and Geetha Priya .M, "Radar and its applications", *International Science Press*, vol. 10, pages 1–9, 2017.

[9] Olga Boric-Lubecke, Victor M Lubecke, Amy D Droitcour, Byung-Kwon Park, and Aditya Singh, *Doppler radar physiological sensing*. John Wiley & Sons, 2015.

[10] J. Oberhammer, N. Somjit, U. Shah, and Z. Baghchehsaraei, "16 - RF MEMS for automotive radar", in *Handbook of Mems for Wireless and Mobile Applications*, ser. Woodhead Publishing Series in Electronic and Optical Materials, Deepak Uttamchandani, Ed., Woodhead Publishing, 2013, pages 518–549, ISBN: 978-0-85709-271-7. DOI: https://doi.org/10.1533/9780857098610.2.518.

[11] NOAA US Department of Commerce, *Nws jetstream - how does doppler radar work?*, 2021. [Online]. Available: https://www.weather.gov/jetstream/how.

[12] Hsueh-Jyh Li and Yean-Woei Kiang, "Radar and inverse scattering", *The Electrical Engineering Handbook*, pages 671–690, 2005.

[13] Army Research Laboratory U.S. Army Combat Capabilities Development Command, "Near-field target scattering characterization and radar modeling (article no. arl-tr-9193)", 2021.

[14] Yang Liu, Weidong Hu, Wenlong Zhang, Jianhang Sun, Baige Xing, and Leo Ligthart, "Radar cross section near-field to far-field prediction for isotropic-point scattering target based on regression estimation", *Sensors*, vol. 20, no. 21, 2020, ISSN: 1424-8220. DOI: 10.3390/s20216023.

[15] Madhu, *What is the difference between near field and far field*, 2021. [Online]. Available: https://www.differencebetween.com/what-is-the-difference-between-near-field-and-far-field/.

[16] Philippe Pouliguen, Bourlier Christophe, Jean-Francois Damiens, and J. Saillard, "Analytical formulae for radar cross section of flat plates in near field and normal incidence", *Progress in Electromagnetics Research B*, vol. 9, pages 263–279, Jan. 2008. DOI: 10.2528/PIERB08081902.

[17] P. Pouliguen and L. Desclos, "A physical optics approach to near- field rcs computations", *Annals of Telecommunications*, vol. 51, 1996.

[18] L. Desclos and P. Pouliguen, "The physical optics applied to discs and square plates in near-fields leads to simple formula", *Microwave and Optical Technology Letters*, vol. 9, 1995.

[19] Fortuny Guasch J and Chareau J, "Radar cross section measurements of pedestrian dummies and humans in the 24/77 GHz frequency bands", Luxembourg (Luxembourg), Scientific analysis or review LB-NA-25762-EN-N, 2013. DOI: 10.2788/80844.

[20] Hanqiao Zhang, Steven Krooswyk, and Jeff Ou, "Chapter 5 - measurement and data acquisition techniques", in *High Speed Digital Design*, Hanqiao Zhang, Steven Krooswyk, and Jeff Ou, Eds., Boston: Morgan Kaufmann, 2015, pages 199–219. DOI: https://doi.org/10.1016/B978-0-12-418663-7.00005-8.

[21] Giovanni Manfredi, Paola Russo, Alfredo Leo, and Graziano Cerri, "Efficient simulation tool to characterize the radar cross section of a pedestrian in near field", *Progress In Electromagnetics Research C*, vol. 100, pages 145–159, Mar. 2020. DOI: 10.2528/PIERC19112701.

[22] Ming Chen, Chi-Chih Chen, Stanley Y.-P. Chien, and Rini Sherony, "Artificial skin for 76–77 GHz radar mannequins", *IEEE Transactions on Antennas and Propagation*, vol. 62, no. 11, pages 5671–5679, 2014. DOI: 10.1109/TAP.2014.2355259.

[23] Emanuele Piuzzi, Paolo D'Atanasio, Stefano Pisa, Erika Pittella, and Alessandro Zambotti, "Complex radar cross section measurements of the human body for breath-activity monitoring applications", *IEEE Transactions on Instrumentation and Measurement*, vol. 64, no. 8, pages 2247–2258, 2015. DOI: 10.1109/TIM.2015.2390811.

[24] Makoto Yasugi, Yunyun Cao, Kiyotaka Kobayashi, Tadashi Morita, Takaaki Kishigami, and Yoichi Nakagawa, "79ghz-band radar cross section measurement for pedestrian detection", in *2013 Asia-Pacific Microwave Conference Proceedings (APMC)*, 2013, pages 576–578. DOI: 10.1109/APMC.2013.6694869.

[25] John E. Kiriazi, Shekh M. M. Islam, Olga Borić-Lubecke, and Victor M. Lubecke, "Sleep posture recognition with a dual-frequency cardiopulmonary doppler radar", *IEEE Access*, vol. 9, pages 36 181–36 194, 2021. DOI: 10.1109/ACCESS.2021.3062385.

[26] John E. Kiriazi, Olga Boric-Lubecke, and Victor M. Lubecke, "Radar cross section of human cardiopulmonary activity for recumbent subject", in *2009 Annual International Conference of the IEEE Engineering in Medicine and Biology Society*, 2009, pages 4808–4811. DOI: 10.1109/IEMBS.2009.5332634.

[27] Øyvind Aardal, "Radar monitoring of heartbeats and respiration", Ph.D. dissertation, Faculty of Mathematics and Natural Sciences, University of Oslo, 2013.

[28] Pablo Sanchez-Olivares, Lorena Lozano, Álvaro Somolinos, and Felipe Cátedra, "Em modelling of monostatic rcs for different complex targets in the near-field range: Experimental evaluation for traffic applications", *Electronics*, vol. 9, no. 11, 2020, ISSN: 2079-9292. DOI: 10.3390/electronics9111890.

[29] Pedro Pinho, Hugo Santos, and Henrique Salgado, "Design of an anechoic chamber for w-band and mmwave", *Electronics*, vol. 9, no. 5, 2020, ISSN: 2079-9292. DOI: 10.3390/electronics9050804.

[30] Italian National Research Concil. "Dielectric properties of body tissues". (2000), [Online]. Available: http://niremf.ifac.cnr.it/tissprop/ (visited on 04/12/2023).

[31] P.Ferreira T.Varum J.Vieira D.Malafaia B.Oliveira and A.Tomé, "Cognitivebioradar: The natural evolution of bio-signals measurement", *Journal of medical systems*, vol. 20, no. 10, 2016.

A

Auxiliary simulations of the 3D subjects

Young Male Subject

In this appendix, all the auxiliary simulations performed with the 3D subjects are presented. Firstly, a study was conducted to evaluate the simulation time of the WaveFarer software. This aspect was considered important because, given that this software employs ray tracing and other techniques, it can be computationally demanding when dealing with 3D CAD models. To reduce the computation time and observe if the results diverged, specific parts of the young male subject were removed. In one simulation, only the torso of the 3D model was used, while in another simulation, the torso of the 3D model without the back was used. The 3D models used in these simulations are depicted in Figure A.1.

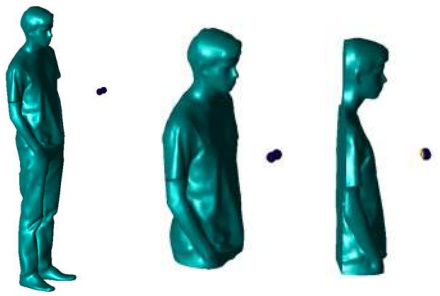

Figure A.1: Torso of the 3D subject with and without the back.

To test the efficiency of the software, when removing certain parts of the 3D model, the received power and the RCS were measured in a range of 0.5 m to 2 m. The results obtained are in Figure A.2.

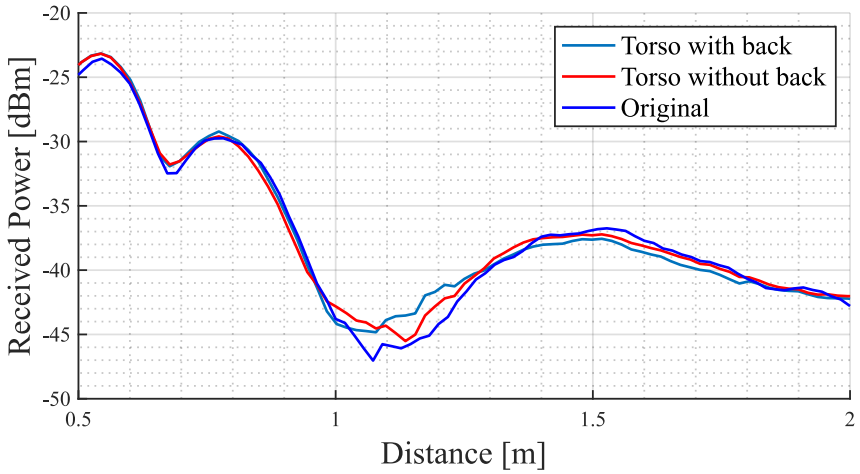

(a) Received Power

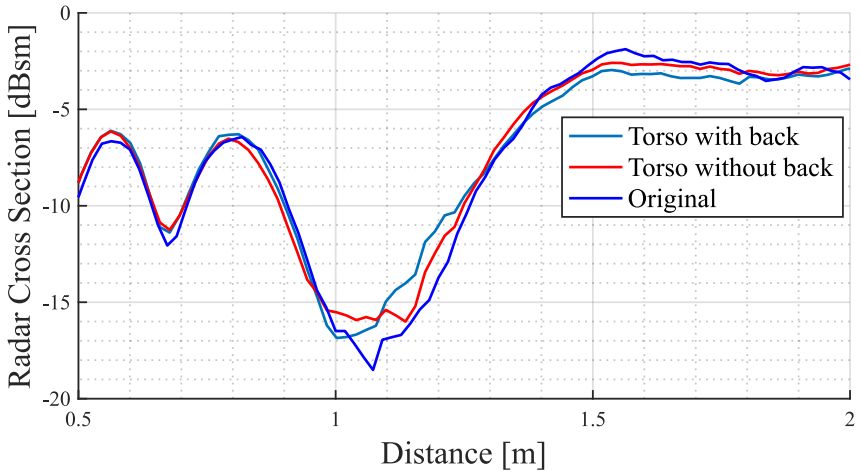

(b) RCS

Figure A.2: Received power and RCS of 3D male torso with and without back.

Regarding this analysis, it was observed that by removing parts of the 3D model, the simulation became more efficient from a time point of view when certain parts were removed. However, starting from a distance of 1 m forward, the results began to diverge because the legs no longer contributed reflections that were visible to the antennas. This effect can also be observed in Figure 4.4. Although removing the back of the 3D subject model did not have a drastic impact, it slightly altered the received power. Due to these reasons, it was deemed best to perform the simulation with the full CAD model.

The next analysis was performed with a scaled down 3D male subject model. The subject was scaled down on all axes from 1 to 0.8 to observe the impacts that minimising

the subject could have on the LM. The received power as well as the RCS are presented in Figure A.3. When scaling down the subject, the target was reduced in width, height, and depth. In the scaled signal, the LM are not as prominent as they were when the 3D subject was not scaled, especially around 1 m. The initial behaviour for the RCS is very similar until 1 m, although the LM positions seem to be slightly shifted.

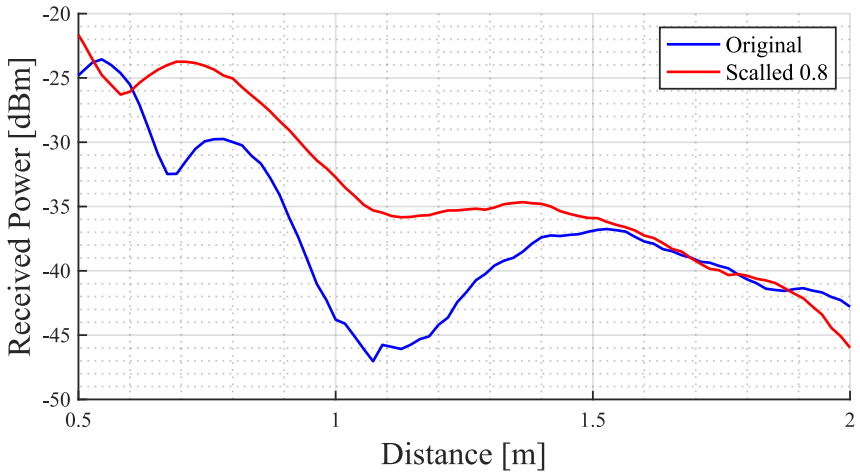

(a) Received Power

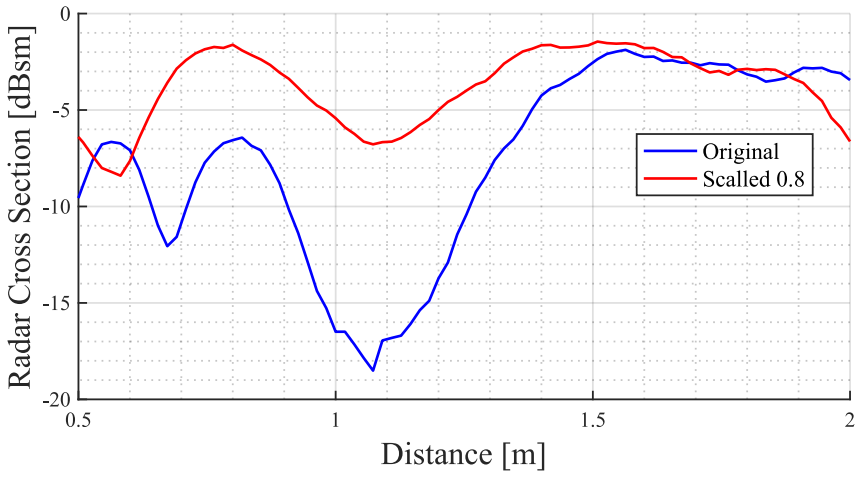

(b) RCS

Figure A.3: Received Power and RCS variation according to the distance - Scaled Young Male.

Female Subject

After the analysis performed with the young male subject, it was important to observed the impacts that a female subject has on the received signal in comparison with a male subject. The female CAD subject, with height of 1.53 m, used in the simulations is presented in Figure A.4. Similarly to the previous subject, the female subject is coated with the material PEC in all the simulations and the antennas were aligned

with the diaphragm. The received power as well as the RCS were obtained within a range of 0.5 m to 2 m. The results can be observed in Figure A.5.

Figure A.4: Female CAD Subject.

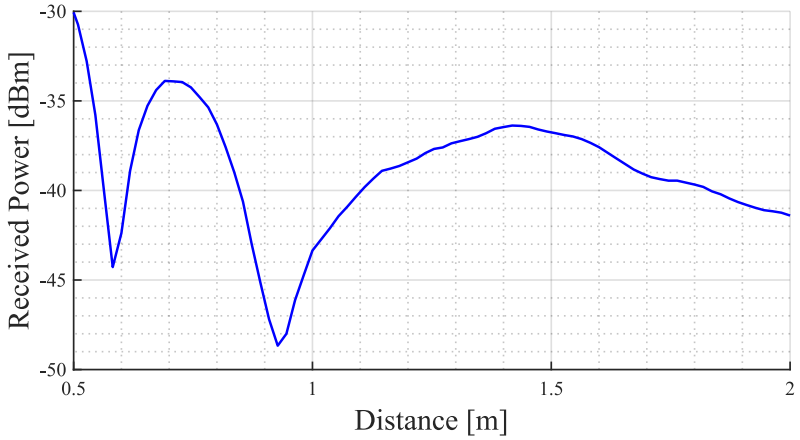

(a) Received Power

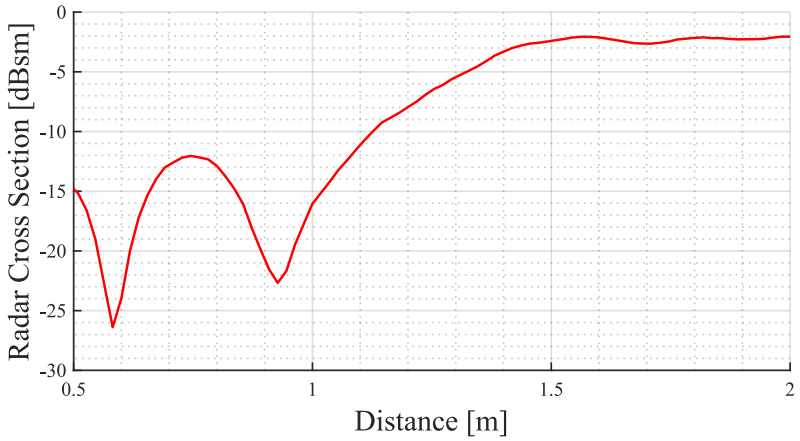

(b) RCS

Figure A.5: Received Power and RCS variation according to the distance - Female Subject.

The received power decreases with the distance and the RCS increases as expected. In both signals, the subject presents two very pronounced LM at 0.6 m and 0.9 m, having a more constant behaviour after 1.5 m. The female subject, compared with the young male subject, has significantly more pronounced LM and these occur before 1 m, which is at a slightly lower distance than with the young male.

The next set of tests performed on this subject was the variance of the frequency from 5.6 GHz up until 6 GHz, just like it was previously done with the young male subject. The goal once again was to observe if there is a frequency that produces less pronounced LM. The received power and RCS obtained for the female subject are presented in Figure A.6.

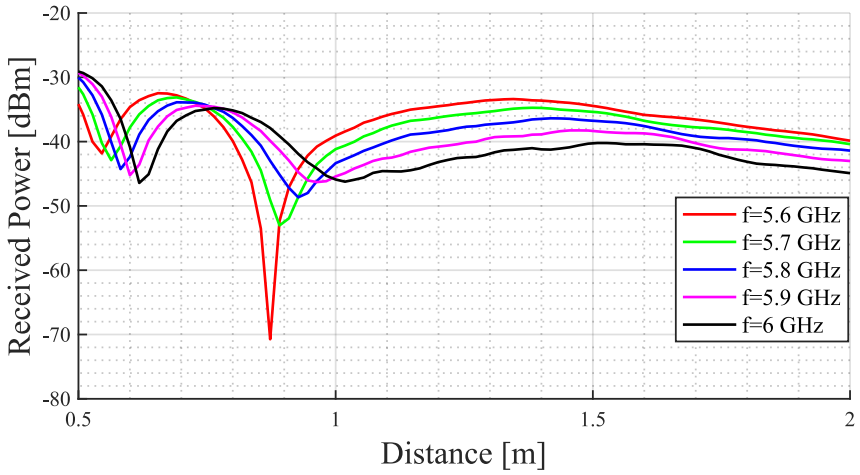

(a) Received Power

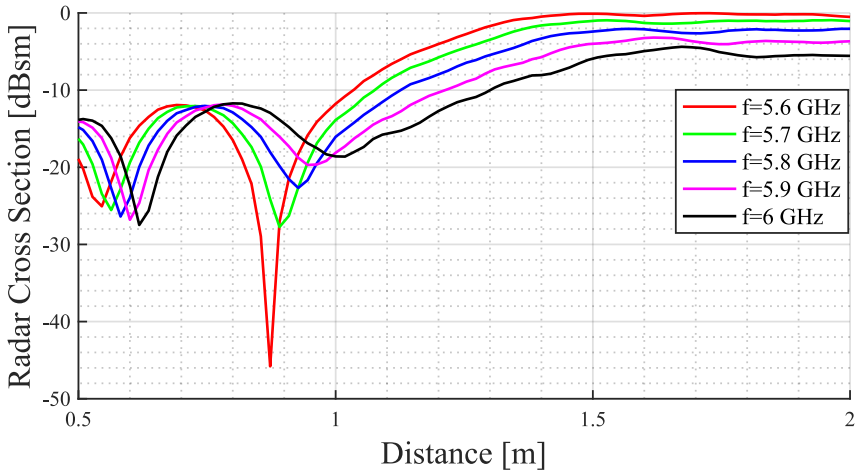

(b) RCS

Figure A.6: Received Power and RCS variation according to the distance on the female subject - Range from 5.6 GHz up until 6 GHz.

As it can be observed, at 5.6 GHz there is a very pronounced last LM in comparison to all the other frequencies at around 0.85 m. Also, the last LM tends to be less

pronounced with the increase of the operating frequency. For this particular subject, it appears that 6 GHz would be probably a better operating frequency, since the LM obtained is less pronounced.

The last validation involving this subject was regarding the width of the chest-wall. The width of the chest-wall was changed between a range of 0.23 m up until 0.32m. This was the same range of distances performed on the young male subject.

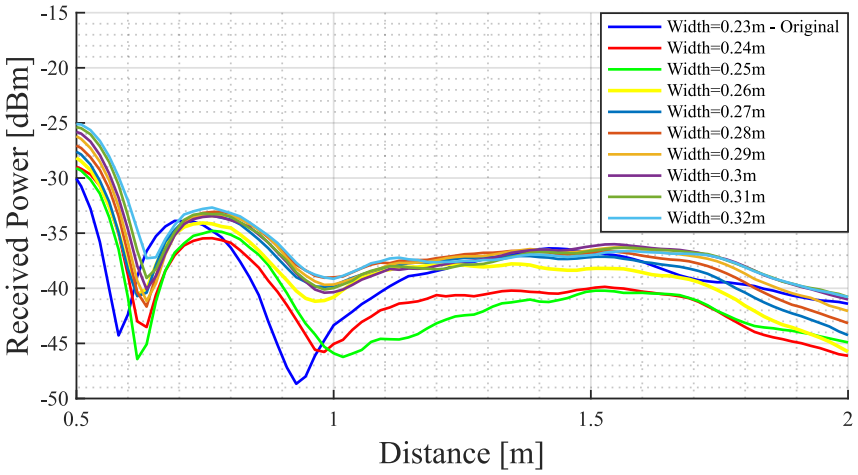

(a) Received Power

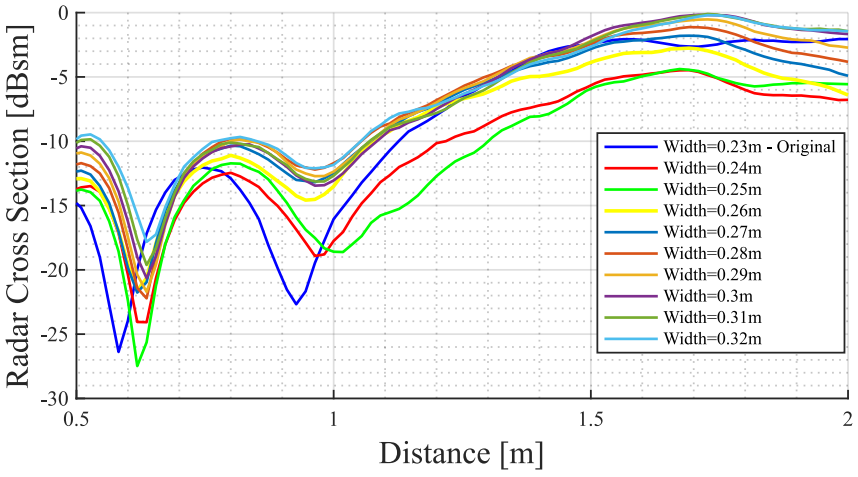

(b) RCS

Figure A.7: Received Power and RCS variation according to the distance - Variation of the width of the chest-wall of the female subject.

The results are presented in Figure A.7, where the original width of the chest-wall of the female subject was 0.23 m. In the transition from 0.23 m to 0.24 m, it appears that the last LM starts being less pronounced and shifted closer to 1 m. From 0.27 m of width forward, the last LM stays at approximately the same distance and with the same value of received power. One plausible reason for this is the fact that, by increasing the width of the 3D subject, the chest-wall area is becoming more flat, similar

to a rectangular/square shape, and as previously observed in Chapter 3 these shapes produce less pronounced LM than more circular objects.

B

Auxiliary analysis of the received power and RCS of the mannequin

In this appendix are presented all the auxiliary experiments performed on the mannequin. It is worth mentioning that in these tests, the S_{21} parameter was not measured for a period of time. Only one measurement of the S_{21} parameter was done for every distance, making this analysis a little less reliable than the one presented in Chapter 5. Nonetheless, this analyses was valuable to better understand the impact of the posture, as well as, the position of the arms have on the received signal. The description of these tests is presented in Table B.1.

Table B.1: Tests performed with the mannequin.

Test 1	Arms were slightly forward
Test 2	Arms were slightly backwards
Test 3	Arms were excessively forward
Test 4	Arms were excessively backwards
Test 5	Left arm was forward and right arm was backwards
Test 6	Attempted to replicate the conditions of Test 1
Test 7	The torso was rotated 5º to 10º to the right

The comparison between all the tests presented in the previous table are in Figure B.1, where the received power as well as the RCS are present in these graphs. As it can

observed, even the slight change in the position of the arms or the torso causes a big change on the received signal as well as the RCS. Also, rotating the torso of the subject causes a very pronounced LM around 1.05 m. Regarding the Tests 1 and 6, where it was attempted to replicate the same conditions in posture and placement of the arms of the mannequin in both tests, it was not possible, since slightly different signals were obtained. Overall, replicating the exact position and posture of a subject is challenging, and the placement of the arms significantly affects the received signal.

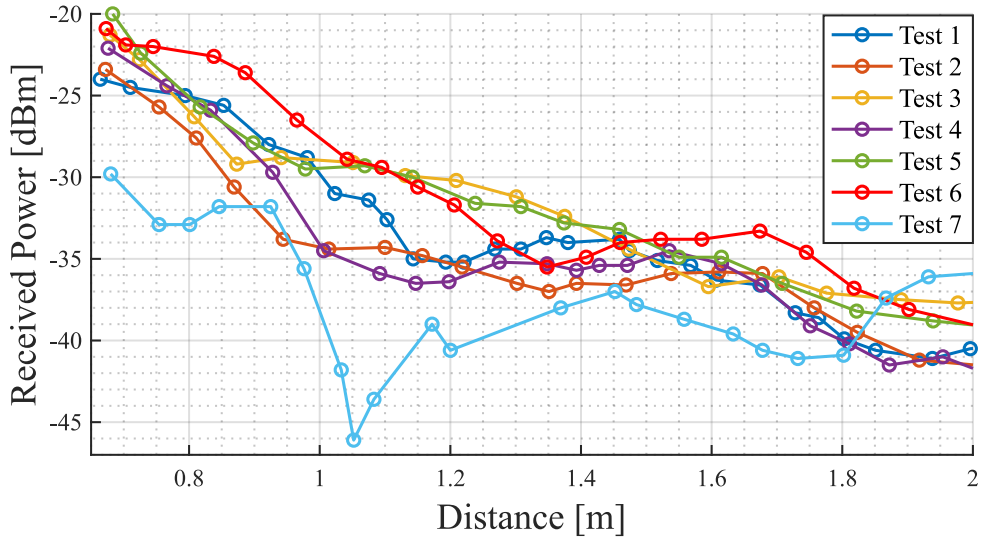

(a) Received Power

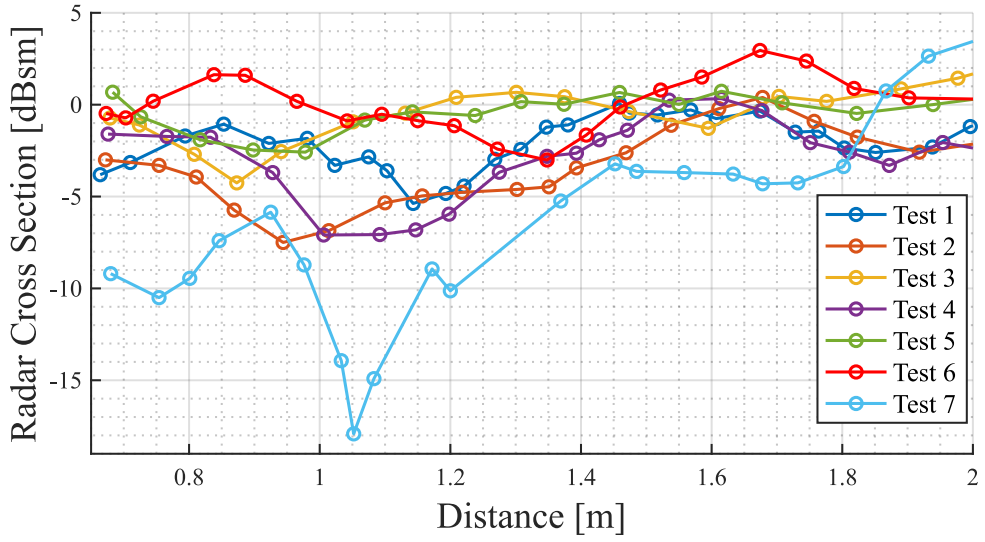

(b) RCS

Figure B.1: Received power and RCS obtained for the mannequin while performing various tests.